Control of an Axial Flow Tidal Stream Turbine

Ben Whitby

Institute of Energy

Cardiff University

A thesis submitted for the degree of

Doctor of Philosophy

August, 2013

To my mother and father, Linda and Christopher Whitby, for making this journey possible.

Declaration

This work has not previously been accepted in substance for any degree and is not concurrently submitted in candidature for any degree.

Signed..... (Candidate) Date.....

This thesis is being submitted in partial fulfilment of the requirements for the degree of PhD.

Signed..... (Candidate) Date.....

This thesis is the result of my own independent work/investigation, except where otherwise stated. Other sources are acknowledged by explicit references.

Signed..... (Candidate) Date.....

I hereby give consent for my thesis, if accepted, to be available for photocopying and for inter-library loan, and for the title and summary to be made available to outside organisations.

Signed..... (Candidate) Date.....

Abstract

Tidal stream turbines have the potential to generate electricity from a renewable source that is highly predictable and non-polluting. The United Kingdom's geographical location means that it has one of the most significant wave and tidal resources in the world. The implications of controlling horizontal axial flow, variable speed tidal stream turbines for the purpose of optimising energy capture, regulating power and reducing mechanical loads has been investigated.

The research was separated into two main areas: control of the turbine in below rated flow speeds where the objective was to maximise energy capture, and control of the turbine in high flow speeds where the aim was to regulate power, shed load and ensure the survivability of the turbine.

A control strategy that maximises the power output of a tidal stream turbine in below rated flow speeds, by allowing the rotor speed to be varied, was implemented. The performance of the control strategy was assessed in simulation and then implemented on a hardware in the loop test rig. In both cases the controller performed well and was able to maximise power output from the turbine by varying the rotor speed to maintain the optimum tip speed ratio.

Two control strategies for regulating the output power from a tidal stream turbine in high flow speeds were investigated and compared. The first strategy relies on adjusting the pitch angle of the rotor blades to regulate power and the second assumes fixed pitch rotor blades and relies on the stall characteristic of the blades to regulate power. Models of both the pitch and stall regulated turbines were developed and simulated using the commercially available software GH Tidal Bladed®. The control system design behind both strategies was developed in Matlab. Following control implementation a comparison of each model was carried out in terms of performance under turbulent flows, loading and energy yield. Following the comparison it was concluded that the performance of the pitch regulated tidal stream turbine was superior to that of the stall regulated turbine. The research also revealed that the dynamics of each turbine model are significantly different for above rated flow speed operation. This has implications on controller design and loading experienced by each tidal stream turbine.

Acknowledgements

I would like to express my deepest appreciation to the following individuals without whom this would not have been possible: Prof. Nick Jenkins, for your wisdom and guidance these past three years; Dr Jun Liang, for your patience and technical assistance and Dr Carlos Ugalde-Loo, for your considerable help and for sharing your enthusiasm and knowledge of control engineering with me.

I would also like to thank the following individuals who I worked closely with and who deserve a special mention: Dr Janaka Ekanayake, Dr John Licari and Dr Ian Moore. My thanks also go out to all my colleagues within the Institute of Energy at Cardiff University who I was privileged enough to meet and who I now consider to be close friends.

Finally, I would like to give a special thanks to my mother, Linda Whitby, for her help and support in putting this thesis together.

Table of Contents

List of Figures

Nomenclature

Roman Variables

A	Rotor swept area, Cross-sectional area
A_{Disk}	Cross-sectional area of actuator disk
a	Axial induction factor
a'	Angular induction factor
C_p	Power Coefficient
C_T	Thrust Coefficient
C_Q	Torque coefficient
C_l	Two-dimensional lift coefficient
C_d	Two-dimensional drag coefficient
C	DC link Capacitance, Aerofoil chord length
D	Generator rotor diameter
D_{dt}	Rotor shaft damping coefficient
E	Annual energy yield
F_{Lift}	Lift force
F_{Drag}	Drag force
F_T	Force normal to plane of rotation (Thrust)
F_τ	Force tangential to circle swept by blade section (Driving torque)
F	Tip-loss factor
i_{sq}	Generator stator current in the q axis
i_{sd}	Generator stator current in the d axis
i_s	Stator current in the q axis
i_q	Grid current in the q axis
i_d	Grid current in the d axis
i_F	Rotor field current
i_{sa}, i_{sb}, i_{sc}	Three-phase stator currents
i_{ga}, i_{gb}, i_{gc}	Three-phase grid currents

I_{load}	Load current
I_{dc}	DC link current
J	Moment of Inertia
K_{dt}	Rotor shaft stiffness
K_{Ω}	Scaling factor for rotational speed
K_t	Generator torque constant
K_{τ}	Scaling factor for torque
L	Generator rotor length
L_{sq}	Permanent magnet synchronous generator inductance in the q axis
L_{sd}	Permanent magnet synchronous generator inductance in the d axis
L_{grid}	Grid coupling inductance
M_a	Amplitude modulation ratio
M_y	Out-of-plane blade root bending moment
M_x	In-plane blade root bending moment
M_{ph}	Phase margin
M_g	Gain margin
m	Mass
N	Gearbox Ratio
n_{pp}	Number of machine pole pairs
P	Power
P_n	Rated power of turbine
p	Pressure
Q	Reactive power
R_s	Permanent magnet synchronous generator stator resistance
R	Outer blade radius
r	Radius
R_{grid}	Grid coupling resistance
T	Thrust
T_s	Sampling delay
T_{act}	Pitch actuator time constant

u_F	Rotor field voltage
V_{flow}	Flow velocity
V_{dc}	DC link voltage
V_n	Rated flow speed of turbine
V_{sq}	Generator stator voltage in the q axis
V_{sd}	Generator stator voltage in the d axis
V_q	Grid voltage in the q axis
V_d	Grid voltage in the d axis
$V_{s\alpha}, V_{s\beta}$	Voltages in the stationary α, β reference frame
V_{ga}, V_{gb}, V_{gc}	Three-phase grid voltages
V_{sa}, V_{sb}, V_{sc}	Three-phase stator voltages
$V_{conv\_a}, V_{conv\_b}, V_{conv\_c}$	Three-phase converter voltages
$\hat{V}_{grid\_ph}$	Peak grid phase voltage
V_0	Undisturbed free stream flow velocity
V_{Disk}	Streamwise flow velocity at the rotor disk
V_3	Streamwise flow velocity in the far wake
V_{Rel}	Relative flow velocity
V_{MSP}	Mean Spring Peak flow velocity

Greek Variables

α	Angle of attack
β	Blade pitch angle
γ	Angle of relative flow to rotor axis
δ	Torque angle
ζ	Damping ratio
η	Mechanical to electrical conversion efficiency of turbine
θ_r	Angular position of rotor shaft
θ_g	Angular position of generator shaft
θ_e	Electrical rotor position angle of generator

θ_{grid}	Grid phase angle
θ_P	Section pitch angle
θ_T	Section twist angle
λ	Tip speed ratio
λ_r	Local tip speed ratio
ρ	Fluid density
τ_d	Generator torque demand
τ_n	Rated torque of turbine
τ_{hy}	Hydrodynamic torque
τ_m	Low speed shaft torque
τ_{em}	Generator electromagnetic torque
φ	Angle of relative flow to rotor plane
Ψ_{pm}	Flux linkage
Ω_{grid}	Synchronous frequency of grid
Ω_e	Generator electrical speed
Ω_g	Angular velocity of generator rotor
Ω_r	Angular velocity of the turbine rotor
ω	Angular velocity of the flow

Chapter 1

1. Introduction

Summary:

An overview of the fundamentals applicable to the use of tidal stream turbines for the generation of electricity in the waters around the United Kingdom (UK) is given. The current energy climate in the UK and the drivers for the development of marine energy are described, and the potential of marine energy as a means of generating renewable electricity, particularly in the waters around the UK, is discussed. An overview of the theory behind tidal stream power generation and the fundamental design drivers is given. Finally an overview of the current status of marine energy technologies is outlined with particular emphasis on tidal stream generators.

1.1 Key Drivers for the Development Marine Energy

1.1.1 Government Targets and Policy

The majority of countries in Europe and some of the states in America are committed to increasing the share of renewables in electricity generation. A European Council agreement, made in March 2007, set a target for 20% of the European Union's energy to be from renewables by 2020. In the UK the goal is for 15% of energy consumption to be met from renewable sources by 2020 (Department of Energy and Climate Change [DECC], 2011a). This is set against the backdrop of legally binding targets to reduce greenhouse gas emissions by 80% (on 1990 levels) by 2050. A 2011 report produced by the DECC (2011b) identifies a number of challenges facing the UK electricity generation sector. These include:

- About 20 GW of ageing generation plant, which will come to the end its life by 2020. This will jeopardise security of supply.
- The need to reduce carbon emissions within the power sector in order to help the UK meet the legally binding targets identified above.
- A general rise in demand for electricity over the next two decades. The need to reduce carbon emissions and reliance on fossil fuels means that electric vehicles and electricity based technologies for heat will become more common. These factors are expected to drive demand for more electricity generation capacity.

The DECC report (2011b) stresses that in order to overcome these challenges the building of new low carbon generation plant will be essential. Renewables, gas and coal Carbon Capture and Storage, and Nuclear will all play a role in decarbonising the power sector and securing the supply of electricity into the future. In terms of the contribution that will be made by renewables, DECC (2011a) have estimated that 234TWh of electricity will need to be generated from renewable sources in 2020 if the UK is to meet its 15% percent target[1]. They have identified eight forms of renewable energy generation which they believe will play a significant role in helping the UK meet this target. They are as follows:

- Onshore Wind
- Offshore Wind
- Biomass Electricity

[1] In the report 'UK Renewable Energy Roadmap' (DECC 2011a) the UK energy demand is forecast to be 1557TWh in 2020.

- Marine
- Biomass heat (non-domestic)
- Air Source and Ground-Source heat pumps (non domestic)
- Renewable transport
- Other (including hydro, geothermal, solar and domestic heat)

Figure 1.1 uses data from DECC (2011a) and is a pie chart representation of the contributions each of the eight technologies is predicted to make in 2020, as a proportion of the total 234TWh of generation.

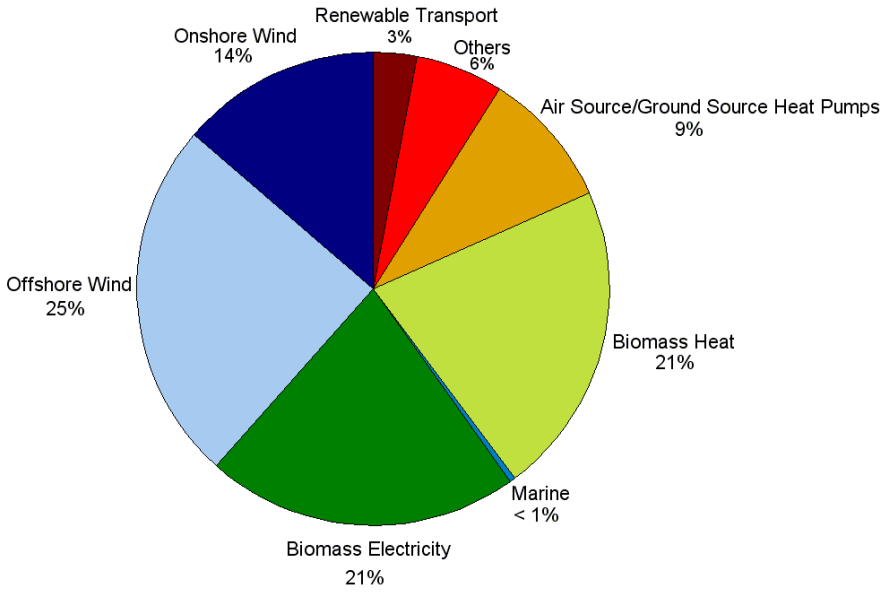

Figure 1.1: Breakdown of different renewable energy technologies and their predicted contribution to the 2020 target of 234 TWh of generation from renewable sources.

The predicted contribution from Marine Energy in 2020 will be less than 1%[2], which represents about 300MW of installed capacity. This is a small contribution when compared with other forms of renewable generation such as offshore and onshore wind, which are predicted to make far more significant contributions. However, marine energy is starting from a low base and is still in its infancy; probably fifteen to twenty years behind the wind industry in terms of maturity. There is currently only about 5MW of installed marine energy capacity in the UK. All of these are prototype devices, most of which are at an early stage of development. Thus reaching

[2] Marine Energy in this case refers only to wave and tidal stream technologies. Other forms of Marine energy such as tidal barrages and osmotic power are not considered here. Thus the contribution from marine renewables could be higher if the potential contribution from these technologies was also taken into account.

300MW of installed capacity by 2020 will represent an achievement. The DECC report (2011a) stresses that beyond 2020 marine energy has the potential to make a far greater contribution. The Welsh government has stated that it intends to have 4GW of installed marine renewable energy generation by 2025 (Welsh Assembly Government 2010). Between now and 2020 experience should increase and developers will move from single prototype installations to deployment of large arrays. As a result the cost of energy should begin to fall. The Carbon Trust (Carbon Trust 2011) has highlighted the importance of reducing the capital costs of marine energy. This will make it more competitive with other forms of renewable generation and accelerate growth.

The rate at which the industry develops will be strongly influenced by government policy and incentives. The current support mechanism for marine energy in the UK takes the form of Renewable Obligation Certificates (ROCs)[3]. The UK government recently increased the support offered to tidal and wave energy developers from 3 ROCs/MWh to 5ROCs/MWh for all devices up to 30MW installed between now and 2017 (DECC 2012). This demonstrates that the government is committed to developing marine energy and they believe it has the potential to make a significant contribution in the future. Due to the current incentive schemes, the ambitious targets set by government to increase renewable generation and the need to reduce carbon emissions, some believe that progress towards large commercial scale arrays will be achieved faster than was the case for wind energy (Bahaj, 2013).

1.1.2 The Tidal Resource

The UK's geographical location means that it is exposed to the Atlantic Ocean in the West and the North Sea in the East. This location provides it with the most significant wave and tidal resource in Europe. This is backed up by a number of studies that have been carried out in order to determine the scale and availability of the UK tidal current resource. The most recent study was undertaken in 2011 (Black and Veatch Ltd., 2011). It estimates that 20.6TWh/y, which is around 7.5% of the UKs current annual electricity demand, could practically be extracted from the waters around the UK using currently foreseeable technologies. This is a conservative estimate, which takes into account the practical constraints that will affect energy extraction such as grid accessibility, shipping, fishing and designated conservation areas. The study also imposed constraints on the total amount of energy that could be extracted at a particular site, believing

[3] The ROC scheme places an obligation on UK suppliers of electricity to source a proportion of their electricity from renewable sources. They are issued to accredited generators of renewable electricity in the UK and are used by electricity suppliers to demonstrate that they have met their obligation. The system is administered by OFGEM (2011).Suppliers who fail to meet their obligation must make a payment to the buy-out-fund. The buy-out price is set by OFGEM and the supplier is charged a certain price for each MWh that they were under their obligation. The buy-out price for the 2013-14 obligation is 42.02 £/MWh (OFGEM 2013).

that if the limits were exceeded then the impacts on the environment and project economics would be unacceptable. In total these constraints removed about one third of the technical resource, which was estimated at 29TWh/y.

The study identified thirty sites in the waters around the UK deemed as suitable for deployment of tidal stream turbines. The figures above represent the total estimated power output from these thirty sites. All of the sites chosen have a water depth of at least fifteen metres and a mean power density in excess of 1.5kW/m^2. Sites that did not meet these criteria were deemed as unsuitable because it would not be economical, using current tidal stream turbine technologies, to develop such sites. Flow rates across the sites vary, with most sites having mean spring peak flow velocities (V_{MSP}) between 2.25m/s and 3.1 m/s.

1.2 Tidal Energy Conversion

1.2.1 Overview

All tidal energy conversion techniques aim to try and tap the energy generated by the rising and falling of the oceans. The primary cause of these cyclic variations in water level is the interaction of gravitational forces associated with the sun, the moon and the earth as well as centrifugal forces resulting from the Earth's own rotation (Bryden, 2004). The spinning of the Earth on its axis results in a centrifugal force while at the same time the moon produces a gravitational force that interacts with the Earth. When the Moon is located at the Earth's equatorial plane, the waters of the Earth's oceans tend to move towards the points nearest to and farthest from the Moon as shown in Figure 1.2. The point on the Earth nearest the Moon experiences greatest gravitational attraction, but a smaller centrifugal force, since it is closer to the centre of mass of the Moon-Earth system. The point farthest away from the Moon experiences the greatest centrifugal force but the lowest gravitational force. The result is two bulges which occur on opposite sides of the planet.

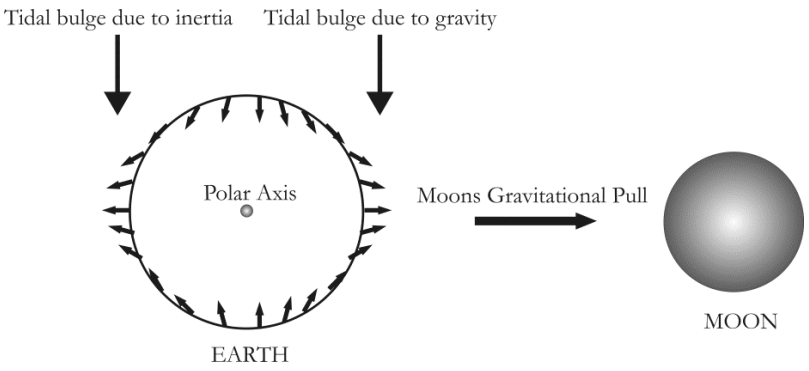

Figure 1.2 : Influence of the Moon on the Tides.

If the Moon stayed on the Earth's equatorial plane, then every coastal site on the Earth would experience two high tides and two low tides over the course of one lunar day, where a lunar day is 24 hours and 50 minutes long. This type of tidal cycle does, in fact, occur in many locations on Earth and is known as a semidiurnal tide. However, the Moon does not always remain on the Earth's equatorial plane, the declination angle[4] of the moon changes as it rotates around the Earth over the course of a Lunar month. In such cases that it moves toward the poles, a tidal period with frequency of once during the lunar day occurs. This is known as a diurnal tide and occurs once every 24 hours, 50 minutes. Tidal currents are classified into groups based on the ratio of diurnal to semidiurnal constituent amplitude: mainly diurnal, mainly semidiurnal, or mixed.

The strength of the tidal currents will also vary over longer periods, with most places experiencing two sets of neap tides and two sets of spring tides during each lunar month. This cycle of spring and neap tides produces the most notable variation in the tides on Earth and is caused by the Sun's gravitational pull, in combination with that of the moon, exerting its influence on the Earth. Thus, the relative positions of the Sun, Moon and Earth will affect the height of the tides experienced at a particular location. Figure 1.3 shows that when the Sun, Moon and Earth are aligned, at full moon and New moon, the gravitational attractions of the Moon and Sun reinforce each other and so the high tide is higher than at any other period of the Lunar month. These are called spring tides. When the moon is at right angles to the Sun, at half moon, the gravitational attractions of the Moon and Sun counteract each other and so the high tide is lower than at any other period during the Lunar month. These are called neap tides.

[4] As the moon revolves around the Earth, its angle increases and decreases relative to the equator. The angle that the Moon forms with the equator is its declination.

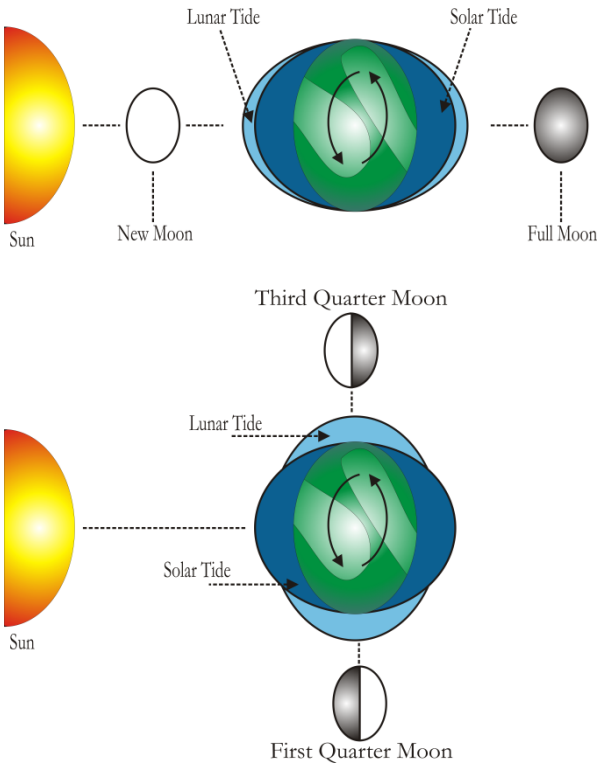

Figure 1.3: Combined Effect of the Moon and the Sun on the Tides. Top figure shows the occurrence of a Spring tide and bottom figure shows the occurrence of a Neap tide.

The height of the tides is not only affected by the relative angles of the Sun, Moon and Earth but also by the distances between them. The orbits of the moon around the Earth and the Earth around the Sun are elliptical. This means that their relative distances will vary, resulting in additional periodical variations in tidal forces. There are a total of 37 separate periods which affect the tides and it takes 18.61 years to cover them all (Garrad Hassan and Partners Ltd., 2010). The periodic nature of each of the tidal constituents means that harmonic analysis is often used to produce highly accurate forecasts of the tides at a particular location.

There are two distinct methods of generating electricity from tidal movement. As discussed by Bryden (2004) the most well known method is the tidal barrage. This is probably due to the fact that a number of tidal barrages have already been constructed, such as the 240MW La Rance tidal barrage power plant in France. There have also been proposals for large barrage schemes in the Severn Estuary (UK) and the Bay of Fundy (Canada), which have attracted significant media attention and heightened public awareness of this type of tidal energy generation. The barrage method involves taking advantage of the change in water level between low and high tides. Water is allowed to accumulate on one side of the barrage such that a head difference is established, and then water is released through a series of turbines to generate electricity. As discussed by Yates et al. (2013) the principles are very similar to conventional hydro power generation and much of the technology is transferable.

According to O Rourke, Boyle & Reynolds (2009) tidal barrages offer the potential to generate huge amounts of clean electricity; however, the scale and cost of barrage schemes has hampered their development. Furthermore, their impacts on the environment, due to the way in which they alter the flow of tidal currents, as well as their potential impact on shipping and navigation are all areas that have attracted opposition. So although the technology for generating electricity using tidal barrages is well established their development is still likely to be restricted for the foreseeable future.

The high cost and widespread opposition to tidal barrages has fuelled interest in another method of tidal energy generation called tidal stream. As the tides rise and fall they produce flood and ebb currents. The strongest currents occur at some point in between the high and low tides. The weakest currents occur in between the flood and ebb currents, at slack tide. These currents have the same periodicities as the vertical movements and are therefore also predictable. In areas where the topography of the land causes these currents to be constrained and channelled, such as in straits or between islands, very high water particle velocities can result. Currents in the Pentland Firth (between the Scottish mainland and the Orkney Islands) can reach 7m/s (Bryden, 2004). Fast flowing currents are also found in estuaries and around the ends of large headlands. The kinetic energy contained in these currents is what a tidal stream turbine (TST) is designed to extract, in much the same way that wind turbines extract kinetic energy from the wind. It is envisaged that multi-unit arrays will be deployed at suitable sites allowing for large scale electricity generation. TSTs are seen as a more economically viable option than large barrages and are perceived as having a lower environmental impact (Hassan, Karim & El-Shafie, 2012). The work in this thesis relates entirely to this form of tidal energy generation.

1.2.2 Headline Benefits of Tidal Stream Energy

Tidal stream energy has the potential to be a highly predictable, non-polluting source of renewable energy. On a global scale the resource is vast, offering many coastal nations an indigenous and therefore more secure alternative to traditional fossil fuels which are often imported.

Predictable and Reliable

The predictability of the tidal resource, both in terms of timing and power output, gives it a unique advantage over other forms of renewable energy. Tidal could deliver power predictably to a timetable, which will make it inherently more valuable to a utility company.

Many renewable energy sources, such as wind and solar, are intermittent in nature (O Rourke, Boyle & Reynolds, 2009) meaning that conventional generators are still needed when the renewable plant is not generating, thus increasing the redundancy. However, the operating hours of this plant are significantly reduced affecting the profitability of the conventional generator, and putting up the price of electricity generated during these periods. Evidence suggests that by carefully selecting the rated flow speed of TSTs and limiting the power above rated it is possible to achieve a relatively high capacity factor. Furthermore if tidal sites are phase shifted relative to each other then the aggregate output from the tidal sites could provide a continuous base load (Clarke, et al., 2006) with little variation. This would require finding locations where the tidal phase varies, which poses a challenge, but evidence suggests that the nature of the tidal resource around the UK could make this possible (Hardisty, 2008).

Low Visual and Environmental Impact

There have not yet been any large scale deployments of TSTs. So far the only deployments have been one off prototypes, usually in designated test centres such as the European Marine Energy Test Centre (EMEC). Thus it is difficult to assess what the visual and environmental impact will be, and any long term effects are merely speculation at this stage. However, the fact that these devices operate underwater suggests that the visual impact will be low, certainly compared to large offshore wind farms or tidal barrages. Some devices may have surface piercing towers that are visible, although the trend in the industry seems to be moving towards designing devices that are fully submerged. Devices designed for deployment in deeper sites (greater than 40 metres), which is where most of the best tidal current resource is, are likely to be fully submerged.

The threat posed by turbine rotors to fish and marine mammals is often discussed. Fraenkel (2007) believes that the impact is likely to be minimal. TSTs are specifically designed to rotate at low speed in order to avoid the occurrence of cavitation, and as a consequence the risk of harming fish or marine mammals is reduced. A report assessing the environmental impact of a prototype commercial scale TST called Seagen, which was operated by Marine Current Turbines Ltd., concluded that over three years of operation the device had no significant impact on marine mammals in the area. Monitoring continues to take place to see what effect the turbine has on the local environment and species that inhabit the area. So far the impact appears to be very low (Royal Haskoning, 2011).

A study to work out the life cycle energy use and $C0_2$ emissions associated with the Seagen turbine also came to a favourable conclusion (Douglas, Harrison & Chick, 2008). The report

calculated the overall embodied energy and $C0_2$ emissions for the device, assuming an operating period of twenty years. To allow comparisons to be made between Seagen and other electricity generating technologies the overall embodied energy and $C0_2$ emissions for the device were divided by the total production of the turbine over its lifetime. This gives the energy and $C0_2$ intensities (i.e. per unit of production). The results were comparable with large wind turbines and much lower than fossil-fuelled forms of generation. This is encouraging and suggests that the environmental impact of TSTs is largely benign, as they produce no emissions while operating and their overall carbon emissions are low.

1.2.3 Headline Challenges Facing Tidal Stream Energy

Tidal energy faces numerous challenges including reducing costs, maintenance, installation and retrieval, and proving survivability. The wind industry experienced many of the same challenges during its development and was able to overcome them. So in tackling many of these problems it is important to have an appreciation for what has already been learnt from the development of wind turbines over the last thirty years. However, TSTs also face many new and unique challenges due to the environment in which they are operating. The marine environment is extremely harsh and device developers will need to prove that their devices can survive and perform in this environment.

Reducing Cost

The levelised cost of energy for tidal stream generators is still very high compared with conventional fossil-fuelled generators and more mature forms of renewable energy generation such as wind. Reducing these costs will be essential if tidal stream energy is to become competitive. A Carbon Trust report (2011) provides an in depth analysis of how costs could be reduced and identifies installation as an area with the highest potential for cost reduction. This is not surprising as the industry has very little experience in this area because so few devices have been installed. Even with experience, installing devices in a subsea environment will present major technical challenges. Safe and economical methods of installing and retrieving devices still require further investigation.

Operation and Maintenance

The marine environment is harsher than the low level atmospheric conditions encountered by wind turbines. Devices will be subjected to corrosion and bio-fouling, which will impact on the survivability and performance of the turbines. Blade surface contamination in the form of algae,

marine flora and barnacles will affect the hydrodynamic performance of the turbine and could lead to significant losses in power (Batten, et al., 2007). It is understood in the wind industry that contamination of the blades can severely degrade aerodynamic performance (Corten, Veldkamp, 2001). It can also alter the angle at which stall occurs and even lead to multiple stall levels for the rotor. Monitoring and maintaining the rotor blades to insure that a build up of marine growth does not occur will be important. Turbine blade damage may also occur due to debris carried in the marine current.

Any power conditioning equipment located at the turbine will need to be housed in an appropriate manner to reduce the risk of failure and the level of maintenance required. Power electronics will almost certainly need to be kept in a dry, de-humidified and temperature controlled environment. This will be a challenge on turbines that are completely submerged.

Provisions will have to be made during the design stage to allow access for maintenance work to be carried out. Some developers have acknowledged this and have incorporated a technique to raise the turbine above the water level making it easier to carry out maintenance work from a ship or platform (Fraenkel, 2010a). Such innovations will help to reduce the operating costs by removing the need for expensive cranes and specialist vessels. Large maintenance operations will also be subject to the weather, which will limit times when the device can be accessed.

Site Specific Environmental Conditions

The environmental conditions experienced by TSTs will be highly site specific (McCann, Thomson & Hitchcock, 2008). They will be influenced by local factors such as: water depth, bathymetry, the shape of the coastline and local wind and weather patterns. Due to the high density of water hydrodynamic loads will dominate over gravitational and inertial loads on TSTs, and of particular importance will be the natures of the turbulence and wave climate as these tend to drive the structural loads (McCann, Thomson & Hitchcock, 2008). Turbulence and wave climate will also be site specific which highlights the importance of taking detailed local measurements at a site before installing devices.

1.2.4 Theory of Hydrokinetic Energy Conversion

The principles applicable to the extraction of hydrokinetic energy from tidal currents are the same as those for wind. The power contained in a moving fluid is a function of the mass flow rate, which is a measure of the mass (m) of fluid passing a point in the system per unit time. It is defined as follows (Manwell, McGowan & Rogers, 2002):

$$\frac{dm}{dt} = \rho A V_{flow} \tag{1.1}$$

where m is the mass of the fluid, ρ is the density of water, V_{flow} is the velocity of the flow and A is the swept area of the rotor.

Considering the kinetic energy per unit time, or power, of a fluid passing through the swept area of a turbine rotor, as shown in Figure 1.4, we obtain the following formula:

$$P_{hy} = \frac{1}{2}\frac{dm}{dt}{V_{flow}}^2 = \frac{1}{2}\rho A {V_{flow}}^3 \tag{1.2}$$

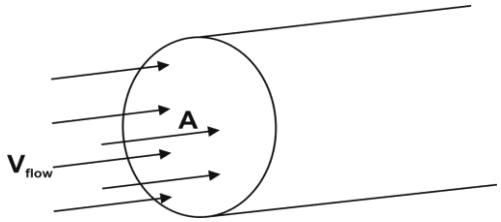

Figure 1.4: Flow of water through the swept area of a rotor disk.

This formula provides a measure of the amount of power that could be extracted per unit area from a hydrokinetic resource if the power could be extracted at 100% efficiency. It is a useful measure for determining the capability of the resource. However, in practice a TST will only be able to extract a fraction of this available power. The above equation is modified to give the actual power that a TST is able to extract. This is given by the following equation (Manwell, McGowan & Rogers, 2002):

$$P_{hy} = \frac{1}{2}\rho C_P(\lambda, \beta)\, A {V_{flow}}^3 \tag{1.3}$$

C_P is a dimensionless term that describes the hydrodynamic efficiency of a turbine. The C_P value is a ratio between the actual power (P) extracted by the rotor to the total kinetic energy incident over the cross sectional area of the rotor:

$$C_P = \frac{P}{\frac{1}{2}\rho A {V_{flow}}^3} \tag{1.4}$$

Due to the Betz limit it is only possible to extract a total of 59.3% $(C_P = 0.593)$ of the total kinetic energy available in the flow (Burton, et al., 2001). In addition the conversion efficiency of

hydrodynamic, mechanical and electrical processes reduces the overall output further. So in practice most real turbines have efficiencies that are lower than the Betz limit, with C_P values in the range 0.4 - 0.5 (Fraenkel, 2010b) for modern axial flow turbines. C_P is a non linear function of the tip speed ratio (λ) and the pitch angle of the blades (β). The tip speed ratio (TSR) is the ratio between the rotational velocity at the tip of the rotor blade and the flow speed and is given by:

$$\lambda = \frac{\Omega_r R}{V_{flow}} \tag{1.5}$$

where Ω_r is the rotational velocity of the rotor and R is the radius of the rotor. In the same way that power is expressed by a non-dimensional power coefficient. The thrust (T) on the turbine rotor can be expressed in a similar way as:

$$C_T = \frac{T}{\frac{1}{2}\rho A V_{flow}^2} \tag{1.6}$$

1.2.5 Turbine Concepts

Extracting the energy available in a flowing fluid can be done in a number of ways. Using a turbine to convert the hydrokinetic power into mechanical power is the most common option. A number of different types of turbines or rotors may be used to achieve this: drag or lift style devices, axial or vertical axis turbines, hybrid turbines combining aspects of several variants, turbines with variable or fixed pitch blades, ducted turbines, etc. Other more novel approaches to power take off include the use of oscillating hydrofoils (Pulse Tidal, 2013) and variable geometry sails (Tidal Sails AS, 2013). However, this thesis will focus on the more conventional turbine based concepts of which there are three main types, they are:

1. Axial turbines: These are turbines in which the rotational axis of the rotor is parallel to the incoming flow. Turbines of this type will usually employ lift type blades that are shaped as aerofoils and rotate relative to the flow. The motion of the fluid around the aerofoil generates the lift force at an angle relative to the blade chord, known as the angle of attack, causing a pressure difference on one side of the blade as compared to the other. The lift force will always be perpendicular to the angle of relative fluid velocity. A drag force is also developed as the fluid flows around the aerofoil. The drag force acts parallel to the relative fluid velocity and impedes

rotation, but for lift devices the average tangential force developed by lift overcomes the retarding drag force, and the net tangential force acting at a radius on the turbine blade generates positive torque and power. Axial flow turbines are a common choice amongst developers of tidal energy converters and are similar in concept and design to modern day wind turbines (Figure 1.5 (B)).

Design of axial flow turbines will vary with developers using different blade numbers and even ducts to streamline and concentrate the flow towards the rotor (Figure 1.5 (A)). Developers have also come up with different designs to overcome the problem of generating power during both the flood and ebb stages of the tidal cycle; when the fluid will be flowing in different directions. Yaw mechanisms have been proposed as well as pitch actuators capable of pitching the blades through 180 degrees to allow bi-directional operation of the turbine. The use of two opposing rotors has also been proposed.

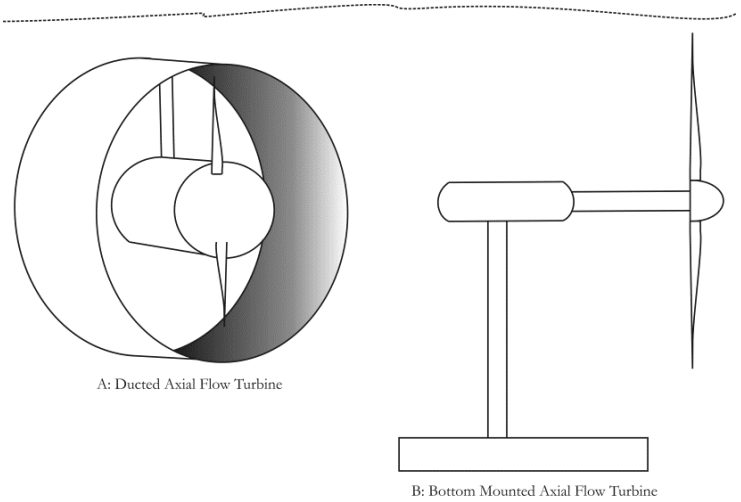

Figure 1.5: Axial flow turbine designs.

2. Vertical axis turbines: These are turbines where the rotational axis of the rotor is vertical to the water surface and perpendicular to the incoming flow. Turbines of this type employ either lift or drag type blades, with some designs using a combination of both. Savonius rotors are drag based and rely on being pushed by the flow, usually at a speed slower than the free stream velocity of the flow. The rotor generates high torque at low speeds, making it desirable for applications such as water pumping (Saha & Rajkumar, 2006). The design of the conventional Savonius rotor is simple and cheap to build – two half cylinders are set with their concave sides facing each other and then offset with a small overlap (Figure 1.6(A)). The disadvantage of

Savonius rotors is their low efficiency compared with lift based devices; hence, many have dismissed their use (Fraenkel, 2010b) citing the fact that they are too inefficient to compete with other designs.

Darrieus turbines are a common type of vertical axis design. They are characterised by aerofoil shaped blades and they rely on generating lift to make them rotate around a central axis (Figure 1.6 (C)). The main disadvantage of Darrieus rotors is that they are not self starting and have very low starting torque. For this reason they are often used in conjunction with Savonius rotors, which are able to provide a large torque at low speeds (Gupta, Biswas & Sharma, 2008). Another issue with the Darrieus turbine is torque oscillation. Despite these problems Darrieus turbines are commonly used in wind and marine energy applications. A description of a Darrieus turbine being used to convert hydrokinetic energy in to electricity in the Sudan is given by Fraenkel (2010b).

The Gorlov helical turbine (Figure 1.6(B)) is another member of the vertical axis family and like the Darrieus turbine it uses aerofoil shaped blades and is lift based. As discussed by Hardisty (2009) the turbine has a number of desirable characteristics: it is self starting and, as with all vertical axis turbines, due to its axial symmetry it will rotate in the same direction regardless of whether the tidal current is in flood or ebb (an important advantage when compared with axial flow turbines, which are difficult to operate in a bi-directional fashion). TST developer GHK Technology (2013) is known to be using a Gorlov helical turbine design.

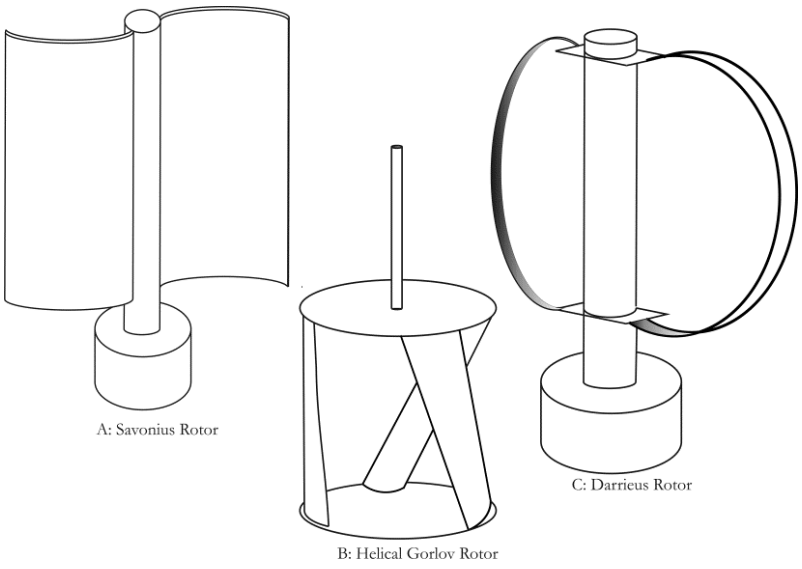

Figure 1.6: Types of vertical axis turbine.

3. Cross-flow turbines: These are turbines where the rotational axis of the rotor is parallel to the water surface and perpendicular to the incoming flow. Like the vertical axis turbines they can employ either lift or drag type blades. Many cross-flow designs are drag based making them less efficient than other lift based turbine designs. However, variants of the Darrieus and Helical Gorlov turbine designs can be used in a cross-flow arrangement as shown in Figure 1.7. TST developer Ocean Renewable Power Company (2013) is proposing the use of Gorlov helical turbines mounted in a cross-flow arrangement.

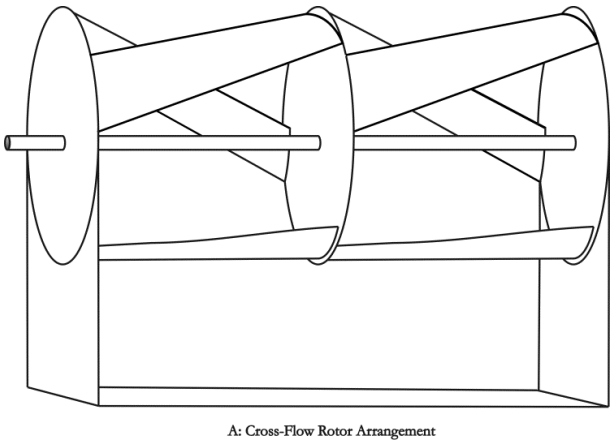

Figure 1.7: Cross-flow turbine design.

There is no universal agreement on the form that tidal stream turbines should take and what rotor type is best. This is evident from the wide number of designs being proposed by developers. Firstly, it is clear that drag based devices like the Savonius rotor will be less efficient than lift based devices; furthermore, drag based devices will normally rotate slower than the free stream flow velocity. It is possible for Savonius rotors to have TSRs of greater than 1.0 (Manwell, McGowan & Rogers, 2002), but normally they will rotate significantly slower than lift based devices. The slow rotational speed of drag devices makes them more difficult to integrate with a generator without a high ratio gearbox to step up the rotational speed. Based on these factors it is unlikely that drag based turbine designs will be competitive with lift based designs.

With the exclusion of the Savonius rotor the other, lift based, vertical axis and cross-flow rotors could make reasonable design options. The Darrieus in particularly is reported to achieve relatively good efficiencies of 30 to 35% (Fraenkel, 2010b). It is also generally easier to operate vertical axis and cross-flow designs in bi-directional flows than it is for axial turbines, which will require a yaw mechanism or some other technique to enable bi-directional operation. Another often cited advantage of vertical axis designs is the fact that the shaft is perpendicular to the flow, meaning the generator can be placed above the water surface (Hassan, Karim & El-Shafie,

2012) making access easier. Cross-flow turbines do not have this advantage and access to the drive-train will be problematic.

Despite these advantages vertical axis or cross-flow designs, like the Darrieus and the Helical Gorlov rotor, are still likely to be less efficient than a well designed axial flow turbine rotor (Eldridge, 1980). Figure 1.8 supports this assumption, and shows that high speed axial flow rotors have a significant advantage. Fraenkel (2002) highlights disadvantages of using Darrieus rotors. These include an increased sensitivity to cavitation, compared to axial flow rotors, and a rapid degradation of performance caused by fouling and surface roughness on the rotor. Furthermore, the Darrieus and the Helical Gorlov rotors are not easily controllable in high flow speeds. The output power cannot easily be regulated and the only way to stop the rotors is by using a brake or spoilers. In contrast there are a number of effective regulation methods (stall or pitch) that have been developed over many years in the wind industry that can be applied to axial flow rotors. The wide knowledgebase that already exists on system design and performance of axial flow rotors, mainly due to advances that have been made in the wind industry, is perhaps the main reason why many tidal developers are choosing to use this type of rotor. This is evidenced by the fact that over fifty percent of devices are based on bottom mounted, low solidity, horizontal axial flow rotors (Garrad Hassan and Partners Ltd., 2010). So although there are still a large number of developers designing different types of device a certain amount of convergence has taken place. The work in this thesis assumes the use of a horizontal axial flow rotor design, and addresses the implications of controlling such a turbine.

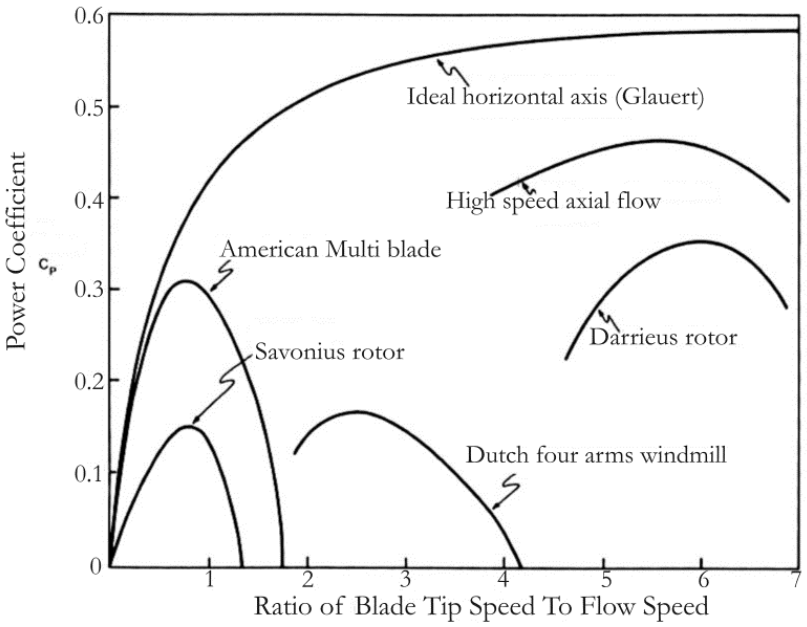

Figure 1.8: Typical Power coefficients achieved by different rotor designs (adapted from Eldridge, 1980, p.131).

1.2.6 Comparison with Wind Turbines

Horizontal axial flow TSTs have obvious similarities to wind turbines; however, there are also a number of important differences. The main difference is the fact that the density of air is about $1/800^{th}$ the density of water. This leads to very large out-of-plane bending forces, for which the main driver is the hydrodynamic thrust force acting in the axial direction (Marsh, 2004). Moreover, the flow rates are lower for TSTs. Wind turbines are rated for a wind speed in the region of 15 m/s (Burton, et al., 2001). Conversely, the rated speed of a TST, based on information from some device developers, is likely to be between 2-3 m/s (Bornens, et al., 2010; Fraenkel P.L. 2010a). In addition, a TST and a wind turbine of a similar power rating will have a significant difference in rotor size. Consider a 1 MW TST (rated flow speed of 2.4 m/s) and a 1 MW wind turbine (rated wind speed of 15 m/s) with the same power coefficient. If the water and air densities are 1027kg/m^3 and 1.225 kg/m^3 respectively then by using (1.3): the ratio of radii can be given as:

$$A = \frac{1000000}{0.5 * 1.225 * 15^3} = 483.7 \therefore R_{WT} = 12.4 \tag{1.7}$$

$$A = \frac{1000000}{0.5 * 1027 * 2.4^3} = 141.1 \therefore R_{TST} = 6.7 \tag{1.8}$$

Therefore the ratio of radii is $R_{TST}/R_{WT} = 0.54$. This result shows that tidal stream turbines are more compact than the equivalent wind turbine that produces the same amount of power. Furthermore, assuming that the tip-speed ratios (1.5) are the same for both turbines the ratio of rotational speeds can be calculated as in (1.9).

$$\frac{\omega_{TST}}{\omega_{WT}} = \frac{V_{TST}}{V_{WT}} x \frac{R_{WT}}{R_{TST}} \tag{1.9}$$

Where ω_{TST} and ω_{wt} are the rotational speeds of the TST and wind turbine respectively. By substituting in the values calculated above:

$$\frac{\omega_{TST}}{\omega_{WT}} = \frac{2.4}{15} \text{x} \frac{12.4}{6.7} = 0.3 \tag{1.10}$$

It is clear that the TST will rotate at roughly a third the speed of the wind turbine. The fact that TST blades are short and rotate relatively slowly means that the centrifugal forces, which balance the bending forces on large wind turbines, are small. This means they do little to restrict the large

bending forces acting on the blades of a TST (Fraenkel, 2002). The slower rotational speed of the TST also has implications on torque developed by the rotor. Using the relationship between angular velocity (Ω_r) and torque (τ_{hy}) given by (1.11) it is clear that if the tidal stream turbine rotates slower than the wind turbine then to generate the same amount of power (P_{hy}) it will have to impose more torque.

$$P_{hy} = \tau_{hy}\,\Omega_r \tag{1.11}$$

This is another key difference between wind turbines and tidal stream turbines and one that needs to be taken into consideration when designing drive-trains. Gearbox failures are one of the main causes of downtime in the wind industry (Hahn, Durstewitz & Rohrig, 2007). If TSTs are developing high torques then it is logical to assume that there will be added stress on the gearbox and drive shaft, which may cause unwanted failures. High operational torques coupled with the fact that TST rotors are smaller, and therefore likely to have lower inertia, than an equivalent wind turbine means that they will accelerate faster as the flow changes. Therefore, regulating rotor speed will be more difficult on a TST particularly in locations where rapid variations in flow speed occur (Winter, 2011a).

1.2.7 Drivetrain and Power Take-Off Options

Obtaining information on the types of drive-train being used by TST developers is difficult. However, as horizontal axial flow turbines are commonly used in the wind industry it is logical to assume that the drive-train concepts will be similar. The different concepts can be distinguished by rotational speed, power regulation and type of generator.

Asynchronous (Induction) Generator

The use of induction generators (either singly or doubly-fed) in conjunction with a gearbox is commonplace in the wind industry. The generator of choice is the squirrel cage induction generator (SCIG). It is cheap and simple to design; nothing more than an induction motor driven above its synchronous speed. Alternating current (AC) is applied to the stator windings producing a rotating magnetic flux; which in turn, induces an opposing current in the rotor bars. When the rotor is driven above synchronous speed the rotor bars cut across the lines of flux produced by the stator and induce active current back into the stator coils. The amount by which the rotating flux produced by the stator exceeds the rotor speed is called the slip (Burton, et al., 2001). In generator mode the slip is negative as the rotor runs faster than the flux produced by the stator. Since the rotor current is proportional to the relative motion between the rotating flux

and the rotor speed, the rotor current and hence the torque are both directly proportional to the slip.

The simplest configuration is to connect the stator windings directly to the grid, and use a high speed low torque induction generator with a gearbox inserted between the shaft of the turbine rotor and the shaft of the generator (Figure 1.9). This configuration is considered to be fixed speed; although, the speed will vary slightly (due to the slip) as the operating power of the rotor fluctuates (Anaya Lara, et al., 2009). The gearbox is necessary to convert the low rotational speed of the turbine rotor to a compatible frequency of the available network, which would be 1500 rotations per minute (RPM) for a four pole machine connected to the European 50Hz network. The turbine and gearbox ratio has to match the available generator speeds, which are for standard induction generators 1500RPM, 1000RPM and 750RPM (4, 6 or 8 pole) (Burton, et al., 2001). In this configuration an external capacitor bank is usually required to adjust the reactive power and control the power factor.

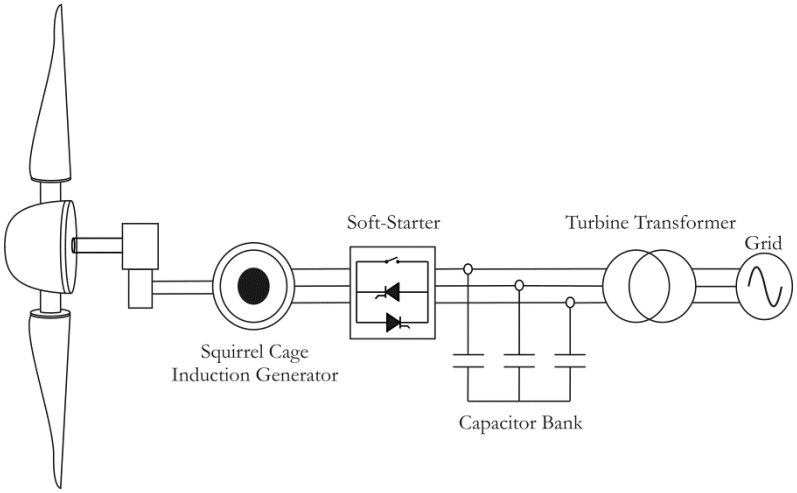

Figure 1.9: Induction generator in fixed speed configuration.

This configuration has a simple and robust design and combines good efficiency and low cost. A disadvantage is the fixed rotational speed. As discussed by Soter and Wegener (2007) this causes a number of problems: power production will not be optimal as one is unable to adapt the rotor speed to the flow speed, and because the generator is directly coupled to the grid fluctuations in rotor torque translate directly into output power variations.

An improvement is to use a wound rotor induction generator with insulated windings brought out via slip rings and brushes. This allows resistors to be placed in series with the rotor which can be varied to control the rotor current; and therefore, the rotational speed of the rotor. Increasing the rotor resistance will reduce the rotor torque allowing the turbine to speed up. This

reduces output power fluctuations during rapid changes in flow speed because the rotor inertia provides a certain amount of buffering; meaning, that torque fluctuations are not translated directly into output power variations. Speed increases of 10% (above the synchronous speed) can realistically be achieved with this system (Burton, et al., 2001). Unfortunately the wound rotor machine is not as robust as the squirrel cage and the need to use slip rings and brushes make it a more expensive solution.

Doubly-Fed Induction Generator

An alternative way of achieving variable speed operation using a wound rotor induction generator is to replace the external resistors in the rotor circuit with a full-power converter. In this configuration the stator is directly coupled to the grid and the rotor is supplied by the power converter (Figure 1.10). Again the rotor current is proportional to the rotor resistance. Increasing the rotor resistance will reduce the current and increase the slip. Therefore, the power flowing through the converter in a doubly-fed induction generator (DFIG) is proportional to the speed variation e.g. for a +/-30% speed variation, the rated power of the frequency converter is only about 30% of the rated power of the generator (Muljadi, Singh & Gevorgian, 2012). When the rotor over-speeds (super-synchronous operation) the converter absorbs power from the rotor and feeds it to the power line. During under-speed (sub-synchronous operation) the converter will borrow power from the line, which it passes on to the stator. This configuration offers more flexibility than using a resistor bank in series with the rotor. A greater range of speed variation can be achieved (+/-30%), and the turbine can operate both above and below the synchronous speed.

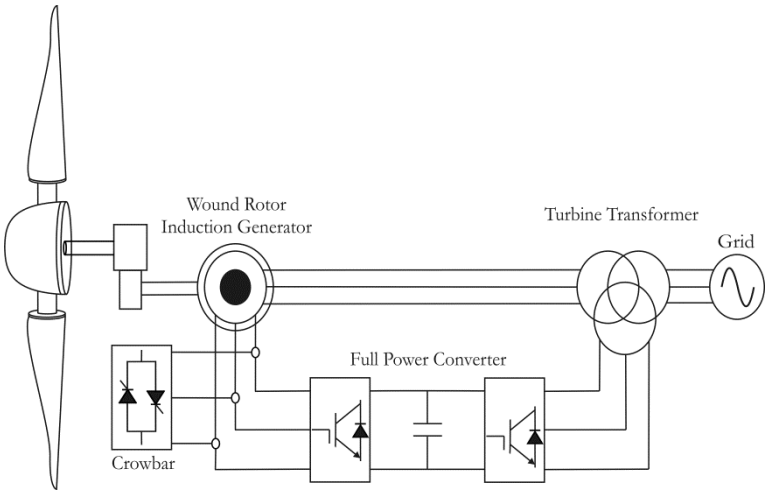

Figure 1.10: DFIG Configuration for TST.

Induction Generator with Full-Power Converter

To achieve full variable speed operation, which allows the speed to be varied from close to zero up to rated speed, the generator must be de-coupled from the grid. This can be accomplished by using a SCIG with a full-power converter (Figure 1.11). In this configuration the power converter is used to transfer current in both directions, allowing active power to be delivered to the grid and reactive power to be supplied to the machine to provide the excitation field. The generator-side converter controls the frequency of the voltage to the stator and also rectifies the AC from the generator to direct current (DC), while the grid-side converter converts the DC back to AC at the appropriate voltage and frequency (Heir, 2006).

As with the configuration of Figure 1.9 this design benefits from the use of a SCIG, which is cheap and robust. The ability to vary the speed over a wide range is an improvement and the power factor can be controlled removing the need for an external capacitor bank (Heir, 2006). The drawback is that the power converter has to be designed to handle the full power of the turbine. This makes it expensive and increases the losses in the system because the converter efficiency affects the entire power (Burton, et al., 2001).

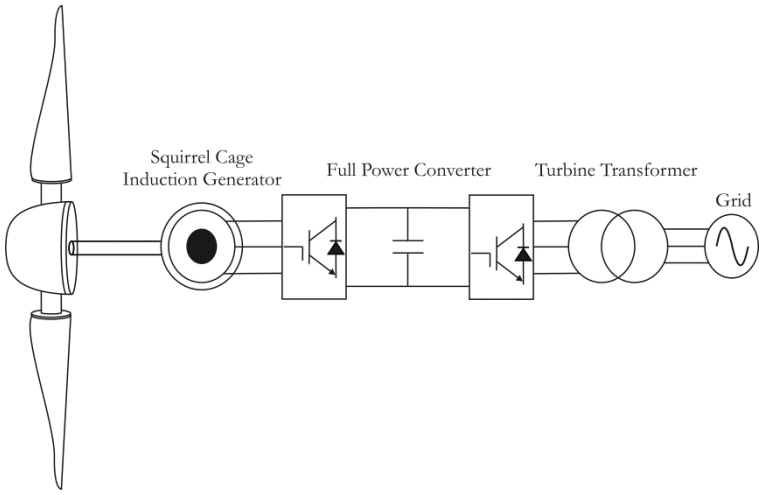

Figure 1.11: SCIG with full-power converter.

Permanently Excited Synchronous Generator with Full-Power Converter

A permanent magnet synchronous generator (PMSG) uses magnets (typically Samarium Cobalt or Neodymium Iron Boron) on the rotor to produce a rotating magnetic flux which induces an electromotive force (EMF) in the stator windings. The EMF produced is proportional to the rate of change of magnetic flux. As the shaft speed changes, as a result of changes in the operating condition of the turbine, the EMF will change. Full variable speed operation can be achieved and

there is no need to supply a reactive magnetising current. In comparison to induction generators, PMSGs operate at a higher power factor and achieve a higher power density.

PMSGs are also well adapted to short pole pitch configurations; therefore, they lend themselves well to multi-pole constructions that are designed to rotate at very low speed. As a result PMSGs make it possible to do away with the gearbox (Bard, et al., 2005). By using a direct-drive system the noise and vibration associated with the gearbox is eliminated, and the conversion efficiency, particularly at part load, is improved. The suitability of PMSGs for use in direct-drive applications has been investigated extensively (Polinder, et al., 2006; Spooner & Williamson, 1996). Various PMSG designs exist including: radial-flux, axial-flux and transverse-flux synchronous generators (Heir, 2006). An analysis of different PMSG designs is beyond the scope of this thesis; however, radial flux designs are currently the most widely used in large wind turbines due to their relatively simple design (Bang, et al., 2008).

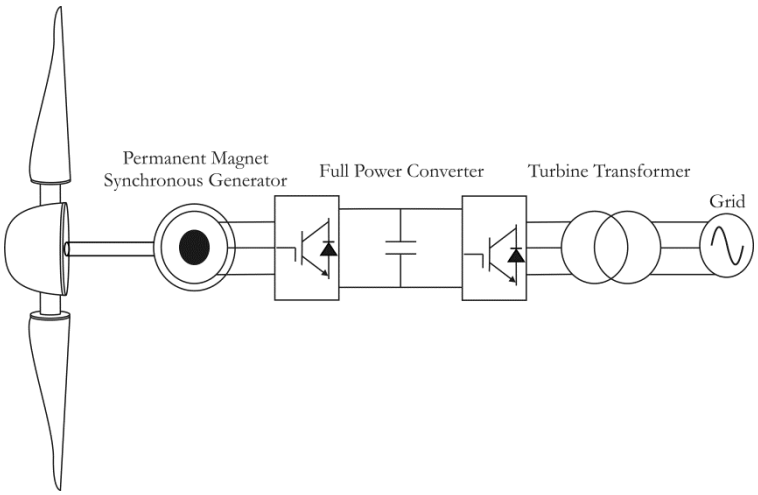

Figure 1.12: PMSG with gearbox removed.

Separately Excited Synchronous Generator with Full-Power Converter

A final option is to use a wound rotor synchronous generator with separate excitation. In this configuration the generator uses electromagnets on the rotor which are fed by direct current from the electrical grid. Since the grid supplies AC, they first have to convert the AC to DC before sending it into the coil windings around the electromagnets on the rotor. The rotor electromagnets are connected to the current by using brushes and slip rings on the rotor of the generator. The separately excited synchronous generator can be operated without a grid connection by using rotating permanent magnets for a pilot exciter which supplies the main exciter coils with the necessary magnetic field.

Comparison and Assessment of Drivetrain and Power Take-off Options

The directly coupled induction machine is a simple robust solution but does not allow variable speed operation leading to less than optimal power extraction. Power quality is also an issue as torque variations are translated directly into output power fluctuations, these torque variations also lead to higher mechanical loads. Furthermore, with this configuration a multistage gearbox needs to be used to convert the low rotational speed of the turbine rotor to a compatible frequency of the available grid. As discussed gearbox failures are a major cause of downtime in the wind industry and with the high torques produced by TSTs the gearbox will be under increased stress. Multistage gearboxes can also lead to increased audible noise, resulting from the gears rotational motion; heat dissipation, caused by friction between the gears; and increased maintenance resulting from long term wear due to friction between the gears.

The DFIG offers an attractive solution and is popular in the wind industry. The fact that the stator is directly coupled to the grid and the rotor is supplied by the frequency converter leads to an electric power through the control circuit which is proportional to the speed variation, e.g. for a +/-30% speed variation, the rated power of the frequency converter is only 30% of the rated power of the generator. In this case the frequency converter is cheaper and causes less loss, but the generator is more expensive and requires more maintenance due to the use of slip rings. Furthermore a multistage gearbox will be required. For these reasons, although it has been widely adopted in the wind industry, tidal developers are sceptical about using the DFIG. The increased complexity of the generator and control, as well as the need to use a multistage gearbox means that it is unlikely to be considered robust enough for use in a marine environment.

Using an SCIG with a full-power converter allows for full variable speed operation. The generator is decoupled from the grid in this configuration making it possible to remove the gearbox, or at least reduce the size of the gearbox from a multistage stage to a single stage configuration. However, at the low speeds experienced in tidal flow regimes (rotational speeds are likely to be in the range 10-30rpm) a generator with a high number of poles will be needed to allow the gearbox to be removed. SCIGs are available with high pole numbers but they are larger and heavier than their high speed counterparts. The relationship between generator power output (P_g) and generator size is given by (Burton, et al., 2001):

$$P_g = KD^2L\omega_g \tag{1.12}$$

where D is the generator rotor diameter, L is the rotor length, ω_g is the rotational speed and K is a constant. To achieve a given power rating a compromise must be made between increasing the diameter of the generator and increasing the length. Due to the square relationship it is usually desirable to increase the diameter (Burton, et al., 2001). Unfortunately SCIGS must supply the excitation field to their rotor via the stator winding (Pillay & Krishnan, 1989); therefore, to keep copper losses in the stator coils down and maintain a high power factor it is necessary to have a small air gap. Manufacturing large diameter induction machines with small uniform air gaps is hard to achieve (Heir, 2006). For these reasons synchronous generators (either permanently excited or separately excited) are preferable in direct-drive applications because larger air gaps can be used and the stator coils only have to carry active power produced in the conversion, which reduces copper losses in the stator.

Separately excited synchronous generators have been used in direct-drive configurations in the wind industry. The main advantage of this configuration over the permanent magnet machine is that one has the ability to control the excitation current and therefore the no load voltage can be controlled. The disadvantage is the high complexity of this type of machine for excitation and voltage control and the use of brushes and slip rings which will potentially increase cost and maintenance (Pillay & Krishnan, 1989). Furthermore, wound rotors are heavier and less efficient than permanent magnet rotors, due to losses in the excitation circuitry (Polinder, et al., 2006). These generators were initially favoured over PMSGs due to the high cost of the materials needed for permanent magnets; however, prices have dropped significantly over the last ten years.

The PMSG appears to be the most attractive solution for use at low speeds. When used in a direct-drive configuration with a full-power converter (Figure 1.12) full variable speed operation can be achieved. This represents a highly efficient and low maintenance solution, which would be very attractive for tidal turbines that are located offshore and may be hard to access.

1.3 Current Status and Future Prospects

1.3.1 Prototype and Commercial Devices

The vast tidal resource around the UK coast means that the area has become a hub for the development of TSTs. To the authors knowledge there are currently no commercially operated TSTs in the world. However, a number of full-scale-grid-connected prototypes have already been installed. Most notable of these is the Marine Current Turbines (MCT) Seagen device which was deployed in 2008 in Northern Ireland's Strangford Lough as the world's first commercial-

scale, grid-connected TST. The device has generated over 5GWh of electricity since being connected. More device installations are planned with leases for up to 1.6GW of wave and tidal devices having been awarded by the Crown estate (Carbon Trust 2011) demonstrating that there is significant activity taking place.

A number of smaller scale prototype devices have been installed in test sites such as the European Marine Energy Test Centre (EMEC), which has operated as a test facility for both wave and tidal stream devices since 2003. Most of these devices have been developed by small research and development companies with limited funding and are at differing stages of development. For a detailed review of currently installed devices and their stage of development the reader is referred to the following sources: Bahaj (2013) and Bahaj (2011).

1.3.2 Future Prospects and Challenges

The next step for the tidal stream energy industry will be making the move from single prototype device installations to small array scale developments. This will not be easy for small privately funded companies to achieve as the increase in cost when moving from single prototype installations to commercial scale multi-device arrays is significant. However, as discussed there does appear to be strong government support for the industry in the UK, which was demonstrated by their willingness to increase support to device developers to 5ROCs/MWh until 2017. Recently a number of large utility companies and original equipment manufacturers have entered the market buying stakes in several device developers. Their involvement combined with favourable incentive and regulatory schemes from government will hopefully accelerate the move towards large commercial scale projects.

As this happens there will hopefully be a convergence of designs with poorer designs being forced out of the market by better performing ones. Some believe that the large number of different devices, with vastly different design philosophies, is hampering progress in the industry (Bahaj, 2011). Between now and 2020 installation of the first multi-device arrays should start taking place in the Pentland Firth, Scotland , and the waters around the Orkney Islands.

1.4 Research Objectives and Thesis Outline

The research objective was to investigate the implications of controlling horizontal axial flow, variable speed TSTs for the purpose of optimising energy capture, regulating power and reducing mechanical loads. The research was separated into two main areas: control of the turbine in below rated flow speeds where the objective is to maximise energy capture, and control of the

turbine in high flow speeds where the aim is to regulate power, shed load and ensure the survivability of the turbine. This thesis details the work carried out to achieve these objectives and has been structured as below:

- Below rated control of variable speed TSTs (Chapter 2).
  - Objectives of below rated TST control.
  - The field oriented control method for variable speed operation.
- Experimental testing of below rated control method (Chapter 3).
- TST modelling in GH Tidal Bladed® (Chapter 4).
- Above rated control of variable speed TSTs (Chapter 4, Chapter 5).
  - Objectives of above rated TST control.
  - Power regulation methods.
  - Controlling stall regulated and pitch regulated TSTs in above rated flow speeds.
  - Comparing loading and energy yield of pitch regulated and stall regulated TST models in GH Tidal Bladed®.

1.5 Publications and Achievements

The research resulted in the acceptance of one IEEE transactions journal paper and two conference papers. Details of the publications are given as follows.

Whitby B., Ugalde-Loo C. 2013, "Performance of Pitch and Stall Regulated Tidal Stream Turbines", *IEEE Transactions on Sustainable Energy,* Accepted for future publication.

Whitby B., Liang J. 2011, "Field Oriented Control of a Permanent Magnet Synchronous Generator for use in a Variable Speed Tidal Stream Turbine", *In Proceedings of the 46th Universities Power Engineering Conference (UPEC),* Soest , Germany.

Whitby B. 2012, " Variable Speed Control of Axial Flow Tidal Stream Turbines using Direct Drive Permanent Magnet Generators", *Paper presented at the International Network on Offshore Renewable Energy Conference (INORE),* Aalborg, Denmark.

In addition the author was invited to present results of his research to an audience of industry experts, including several device developers, at an event organised by renewable energy consultancy Garrad Hassan and Partners Ltd.

Chapter 2

2. Variable Speed Control of Grid Connected Tidal Stream Turbines

Summary:

This chapter addresses the implications of controlling a direct-drive variable speed TST which is interfaced to the electrical grid through a full-power converter. Mathematical models of the hydrodynamic conversion, drive-train and permanent magnet synchronous generator are developed and implemented in Simulink® to allow steady state and transient simulations to be carried out. The theory behind variable speed operation of a TST and the control objectives are discussed. Control strategies for the generator-side and grid-side converters are proposed and implemented. The generator is controlled to extract maximum power from the flow, while vector control of the grid-side inverter allows control of the DC link voltage and also the reactive power delivered to the grid. Frequency response and step response analysis are carried out to assess the closed-loop performance of each controller. Finally the system is simulated to verify the model and test the performance of the controllers.

2.1 Turbine Configuration and Control Objectives

2.1.1 System Description and Implementation

There are many possible TST configurations. The designer can choose between a direct-drive system or a geared system; the generator can be synchronous or asynchronous and connection to the grid can be through a full-power converter, a partially rated converter or directly connected. As discussed in Section 1.2.7 the use of a PMSG in a direct drive configuration is an attractive solution. When used in conjunction with a full-power converter, the generator is decoupled from the grid and full variable speed operation can be achieved. Variable speed operation increases the energy yield of the turbine by allowing it to operate at its maximum power coefficient over a wide range of flow speeds. Figure 2.1 shows the system considered in this thesis.

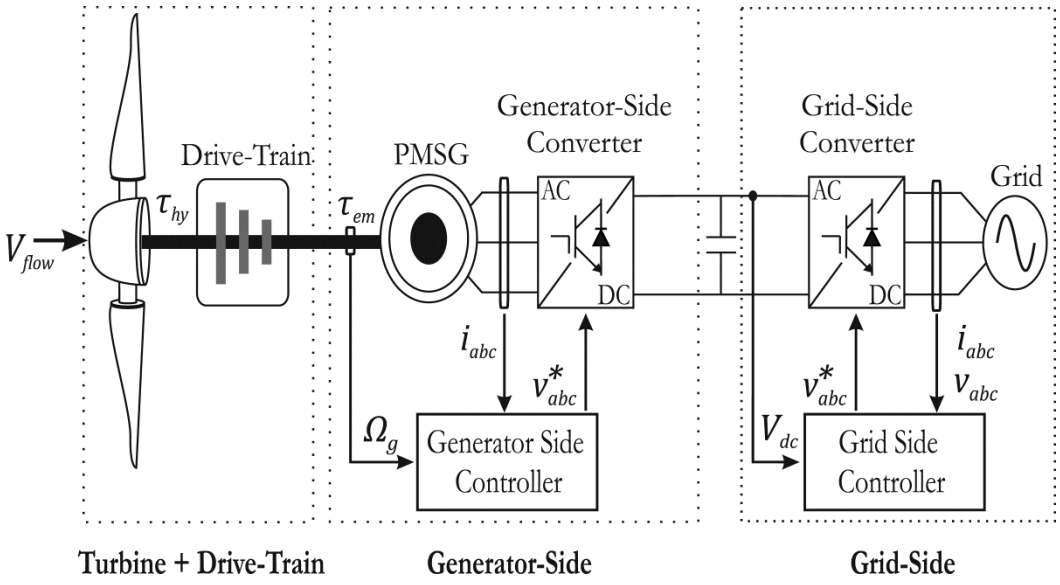

Figure 2.1: Block diagram of PMSG based TST.

The system consists of a PMSG and a full-power converter, consisting of back-to-back voltage source converters. Use of two, six switch converters connected in a back-to-back configuration with an intermediate DC link capacitor has the advantage of allowing for vector control on both the generator and grid-side converters (Pena, Clare & Asher, 1996). This topology allows bi-directional current flow and one has full control over the generator power factor and torque. An alternative is to use a diode rectifier on the generator-side, which simplifies the control and reduces the cost. The disadvantages of using a diode rectifier are mostly related to efficiency. The diode rectifier has been reported as introducing high levels of harmonic distortion in the generator (Huang et al., 2008), which affects efficiency and can introduce pulsating torques. For these reasons the full-power converter with active rectifier is used in this work.

Hydrodynamic Model

The hydrodynamic torque developed by the turbine rotor of Figure 2.1 is (Burton et al., 2002):

$$\tau_{hy} = \frac{1}{2} \cdot \frac{\rho A V_{flow}^3 C_P(\beta, \lambda)}{\Omega_r} \tag{2.1}$$

The block diagram of the hydrodynamic system is shown in Figure 2.2. For modelling purposes, C_P is a mapping function which is expressed through a look-up table (Heir, 2006). This model simply converts the flow incident on the turbine rotor into hydrodynamic torque and does not include any structural dynamics or any dynamic inflow effects, such as shear or tower shadowing. Models that do include these dynamic effects are developed in Chapter 4. For the work in this section the simplified model of Figure 2.2 is sufficient.

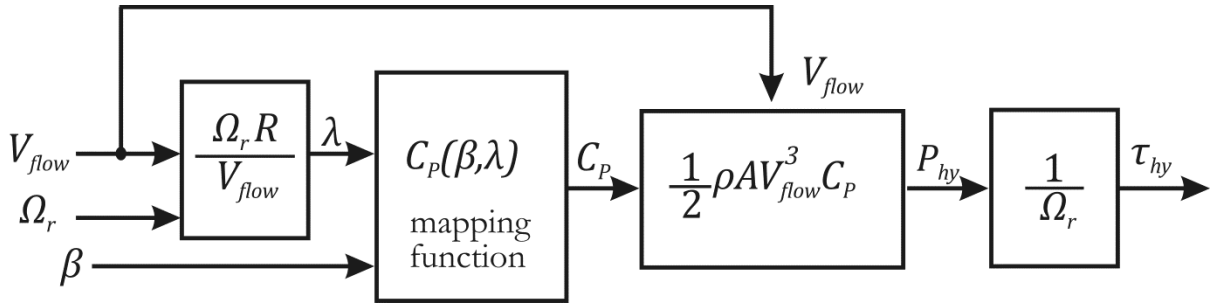

Figure 2.2: Model of hydrodynamic system.

The tip speed ratio (TSR) is calculated based on the flow speed and the rotor speed. An initial condition is set such that the rotor speed is non zero at the start of the simulation. The calculated TSR (λ) and the blade pitch angle (β) are then mapped to the appropriate C_P value using the lookup table. The C_P look-up table is for a generic 1 MW TST rotor. The parameters of the rotor are given in Appendix A.1. Having obtained the C_P value the hydrodynamic torque (τ_{hy}) was calculated.

Drive-Train Model

The hydrodynamic torque generated by the rotation of the rotor is transferred to the generator via the drive-train. In this case a direct-drive system is used, meaning the rotor is connected directly to the generator via a single shaft. To model the TST drive-train a two-mass model is used whereby the rotor and hub are considered to be one lumped mass and the generator is considered to be another lumped mass. The two masses are connected together via a flexible shaft which has a stiffness (K_{dt}) and damping (D_{dt}). The model is shown in Figure 2.3 where

one end of the shaft is driven by the turbine rotor, generating a torque (τ_{hy}). The other end of the shaft is loaded by the generator, which generates a torque (τ_{em}).

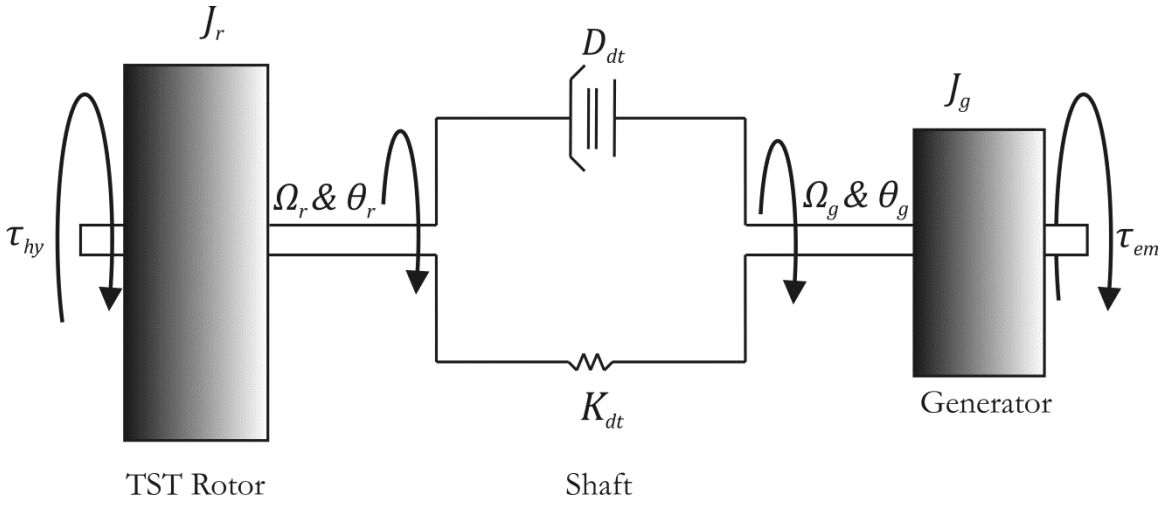

Figure 2.3: Two-mass drive-train model without gearbox.

The drive-train is described by the following set of equations (Florin et al, 2004):

$$\tau_{hy} = J_r \cdot \frac{d^2\theta_r}{dt^2} + K_{dt} \cdot (\theta_r - \theta_g) + D_{dt} \cdot \left(\frac{d\theta_r}{dt} - \frac{d\theta_g}{dt}\right) \tag{2.2}$$

$$-\tau_{em} = J_g \cdot \frac{d^2\theta_g}{dt^2} + K_{dt} \cdot (\theta_r - \theta_g) + D_{dt} \cdot \left(\frac{d\theta_r}{dt} - \frac{d\theta_g}{dt}\right) \tag{2.3}$$

$$\frac{d\theta_r}{dt} = \Omega_r, \quad \frac{d\theta_g}{dt} = \Omega_g \tag{2.4}$$

where θ_r and θ_g are the angular positions of the rotor shaft and generator shaft, Ω_r and Ω_g are the speeds of the rotor shaft and generator shaft. J_r and J_g are moments of inertia for the rotor and generator respectively. The drive-train parameters are given in Appendix A.2.

Generator Model

The electrical equations used to model the PMSG are represented in the rotating dq reference frame, in which the d-axis is oriented along the rotor flux vector position and the q-axis leads the d-axis by 90 degrees (Figure 2.4). Expressing the electrical equations in this way allows the torque producing and magnetising flux components of the machine to be separated; therefore, allowing for the development of a control strategy that provides independent control of the torque. In this model the three phase quantities of the machine (voltages, currents and magnetic

flux) can be described using just two complex vectors. This means that a three phase machine can be modelled as a two phase machine.

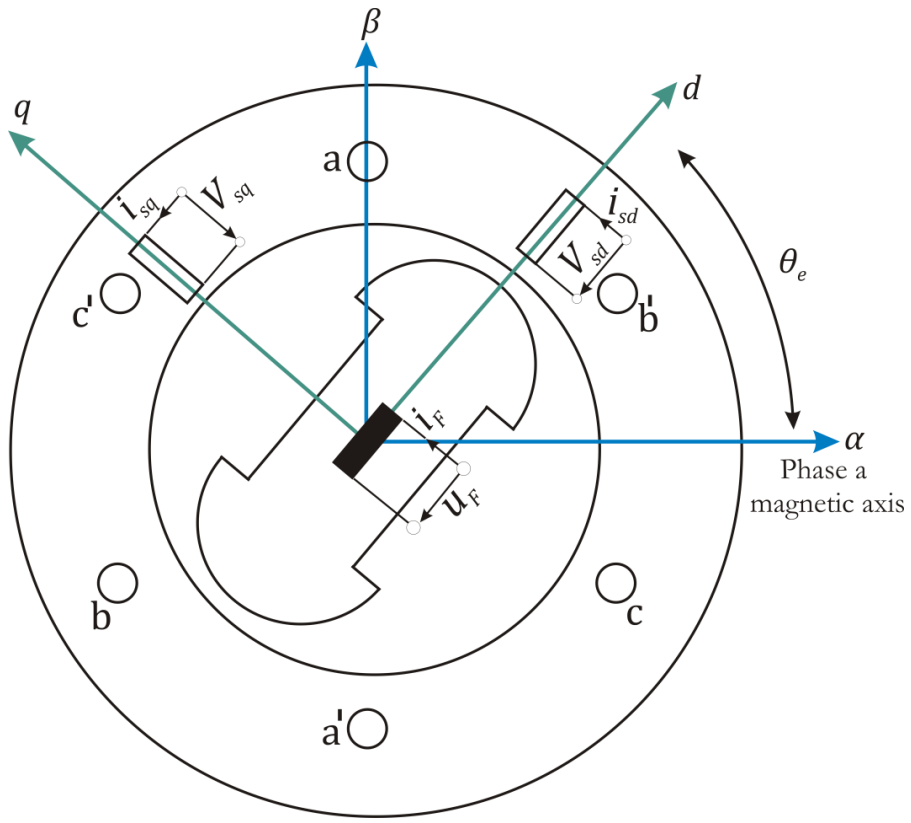

Figure 2.4: Representation of PMSG in the dq rotating reference frame where the three-phase winding has been replaced by a two-phase rotating winding. The d-axis is aligned with the rotor flux field and the q-axis leads the d-axis by 90 degrees. i_{sd} and i_{sq} are the stator currents and v_{sd} and v_{sq} are the stator voltages. i_F and u_F are the rotor field current and voltage. θ_e is the electrical rotor position angle measured relative to the stationary magnetic axis of phase a. α and β represent the stationary (or stator) reference frame. Where α is aligned with the magnetic axis of phase a and β leads α by 90 degrees.

The equations of the PMSG in the d, q reference frame are given as follows (Krishnan, 2010):

$$V_{sd} = i_{sd}R_s + \frac{di_{sd}}{dt}L_{sd} - \Omega_e L_{sq} i_{sq} \tag{2.5}$$

$$V_{sq} = i_{sq}R_s + \frac{di_{sq}}{dt}L_{sq} + \Omega_e\left(L_{sd} i_{sd} + \Psi_{pm}\right) \tag{2.6}$$

where i_{sd} and i_{sq} are the stator currents, R_s is the stator resistance, Ω_e is the electrical PMSG rotor speed, L_{sd} and L_{sq} are the equivalent self inductances of the stator and Ψ_{pm} is the flux produced by the permanent magnets. The full derivation of the PMSG model of Figure 2.4 is given in Appendix B.1. It is assumed that the PMSG used in this work is of the surface-mounted type and exhibits no saliency $\left(L_{sd}/L_{sq} = 1\right)$.

Power Converter Model

The voltage source converters and DC link capacitor are modelled using blocks from the SimPowerSystems library within Simulink® (The MathWorks Inc., 2010). The grid is modelled using an AC voltage source from the SimPowerSystems library in series with an impedance (Z_{grid}).

2.1.2 Control Objectives

The operation of axial flow variable speed TSTs for optimal power extraction is illustrated in Figure 2.5, which shows the ideal power curve for a typical turbine.

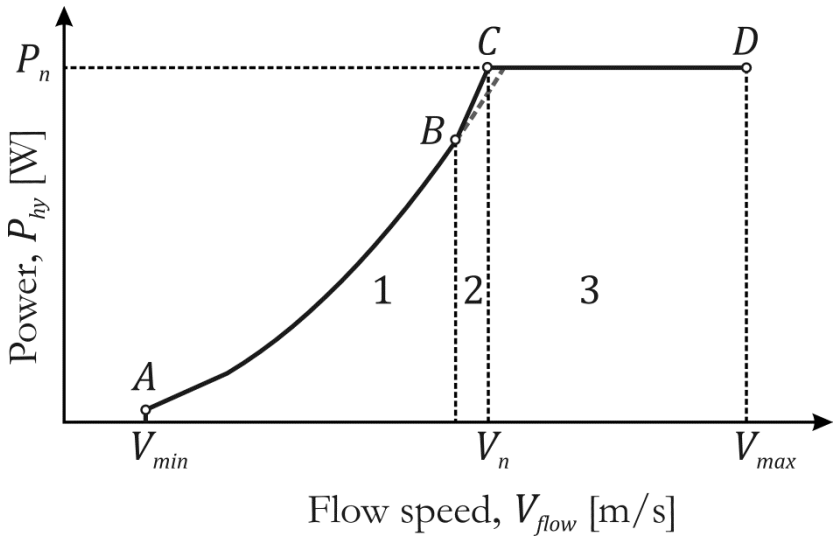

Figure 2.5: Ideal power curve of a TST.

The turbine operates between the cut-in flow speed (V_{min}) and the cut-out flow speed (V_{max}). Below V_{min} the available energy in the flow is so low that the losses and operating costs make it uneconomic to operate the turbine. Above V_{max}, although there is a lot of energy available, these flow speeds occur so infrequently that their contribution to the annual energy yield is minimal. So it is uneconomic to operate the turbine above V_{max} (Bianchi, De Battista & Mantz, 2010). Between these two limits three operating modes are possible. In region 1 (between A and B) the objective is to extract as much energy from the flow as possible by running the turbine at its optimum hydrodynamic efficiency. Region 2 (between B and C) is a transition area between the optimum power curve and the constant power region. Here, the speed of the turbine is limited to avoid over-speeding the generator, and as a consequence, cavitation (Fraenkel, 2002). In region 3 (between C and D) the objective is to limit power to avoid overloading.

This Chapter is concerned with operation of the turbine in region 1, where it is operating in variable speed mode. Operation of the turbine in higher flow speeds (region 2 and 3) is addressed in Chapters 4 and 5. In region 1 the rotor speed is varied to maintain optimum TSR, which maintains peak C_P and maximises output power. This is achieved by controlling the rotor speed through the generator reaction torque. An open loop control is used whereby the generator torque demand (τ_d) is continuously set proportional to the square of the rotor speed (Ω_r) (Bossanyi, 2003):

$$\tau_d = \frac{\pi \rho R^5 C_P}{2\lambda N^3} \cdot {\Omega_r}^2 \tag{2.8}$$

where R is the rotor radius, ρ is the fluid density, λ is the TSR and N is the gearbox ratio. This control ensures that the turbine follows a torque vs. speed trajectory, as illustrated in Figure 2.6(a), which maximises the output power. Figure 2.6(b) shows the power vs. speed trajectory for the same turbine, where it can be seen that the power is maximised. For practical reasons a rotor speed measurement is usually not available, so the control of equation (2.8) is achieved using the generator speed measurement (Ω_g), which is the rotor speed (Ω_r) scaled up by the gearbox ratio (N).

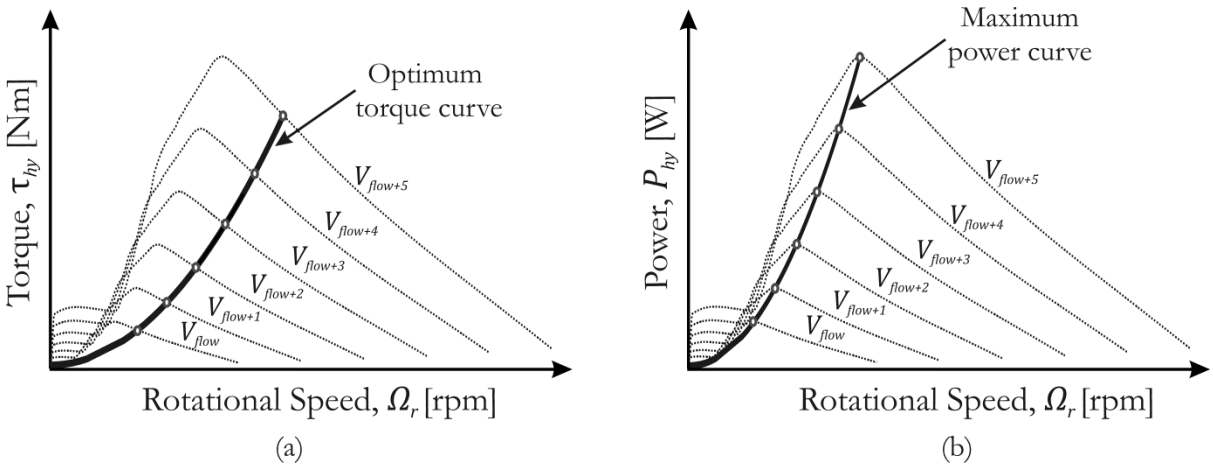

Figure 2.6: Characteristics of a typical TST as a function of flow speed change $(V_{flow}, V_{flow+1}, V_{flow+2}, V_{flow+3}, V_{flow+4}, V_{flow+5},)$: (a) torque vs. rotor speed, (b) power vs. rotor speed.

2.2 Variable Speed Control

2.2.1 The Field Oriented Control Method

The field oriented control method allows for separate closed loop control of both the flux and torque, hence, achieving a similar control structure to that of a separately excited DC machine. By separating the stator current into a magnetic flux producing part and a torque producing part independent control of each is achieved.

Using a two phase machine model, such as that in Figure 2.4, reduces the number of equations and makes control design simpler. By deriving an equation for the electromagnetic torque it can be shown that the torque, and therefore the speed of the PMSG can be controlled using just the q-axis stator current.

Electromagnetic Torque

Assuming a balanced system the equations of active and reactive power in the dq reference frame can be expressed in terms of the voltages and currents shown in Figure 2.4. When going from a three-phase to a two-phase system the input power must remain invariant (Krishnan, 2010). Hence a scaling factor of $\frac{3}{2}$ is used when expressing the power input to the machine in the two-phase dq reference frame.

$$P_{(dq)} = \frac{3}{2}\left(V_{sd}i_{sd} + V_{sq}i_{sq}\right) \tag{2.9}$$

$$Q_{(dq)} = \frac{3}{2}\left(V_{sq}i_{sd} - V_{sd}i_{sq}\right) \tag{2.10}$$

By substituting for V_{sd} and V_{sq} in equation (2.9) from equations (2.5) and (2.6) the input power in the dq reference frame can be expressed in terms of armature resistive losses, rate of change of armature magnetic energy and air-gap power.

$$P_{(dq)} = \frac{3}{2}\left[R_s\left(i_{sd}^2 + i_{sq}^2\right) + \left(\frac{di_{sq}}{dt}L_{sq}i_{sq} + \frac{di_{sd}}{dt}L_{sd}i_{sd}\right) + \Omega_e\left(\Psi_{pm} + \left(L_{sd} - L_{sq}\right)i_{sd}\right)i_{sq}\right] \tag{2.11}$$

The term associated with the air-gap power on the right hand side of equation (2.11) can be extracted to give equation (2.12).

$$P_{(air-gap)} = \frac{3}{2}\Omega_e\left[\Psi_{pm} + \left(L_{sd} - L_{sq}\right)i_{sd}\right]i_{sq} \tag{2.12}$$

The electromagnetic torque is obtained by dividing the air-gap power by the mechanical rotor speed giving equation (2.13) where n_{pp} is the number of machine pole pairs.

$$\tau_{em} = \frac{3}{2}n_{pp}\left[\Psi_{pm}i_{sq} + \left(L_{sd} - L_{sq}\right)i_{sd}i_{sq}\right] \tag{2.13}$$

The term on the left of equation (2.13) is referred to as the permanent magnet torque and is dependent on the rotor flux $\left(\Psi_{pm}\right)$ and the q-axis current $\left(i_{sq}\right)$. The term on the right is the reluctance torque and it is dependent on the d-axis and q-axis currents $\left(i_{sq}, i_{sd}\right)$ and on the difference between the stator self inductances $\left(L_{sd}, L_{sq}\right)$. For a non-salient PMSG the reluctance term disappears, since L_{sd} and L_{sq} are assumed equal, and equation (2.13) reduces to (Pillay & Krishnan, 1989):

$$\tau_{em} = \frac{3}{2}n_{pp}\Psi_{pm}i_{sq} \tag{2.14}$$

From equation (2.14) it is clear that the electromagnetic torque is directly proportional to the q-axis stator current $\left(i_{sq}\right)$. Therefore, variable speed operation can be achieved via control of i_{sq}.

Field Oriented Control Strategies

Field oriented control of a PMSG can be implemented in a number of ways depending on what the objective is. Two common control strategies are:

- **Maximum torque per ampere control** - The main aim of this control strategy is to keep the ratio between the stator current and the electromagnetic torque as small as possible. If the machine has no saliency then the torque is determined solely by the q-axis current. Therefore, by regulating the d-axis current (which makes no contribution to the electromagnetic torque) to zero the excitation flux and the armature flux will be at right angles (torque angle (δ) equal to 90 degrees) and the maximum torque to current ratio is achieved. The phasor diagram for the maximum torque per ampere control is shown in Figure 2.7 where it can be seen that the stator current (i_s) contains only a q-axis component $\left(i_{sq}\right)$.

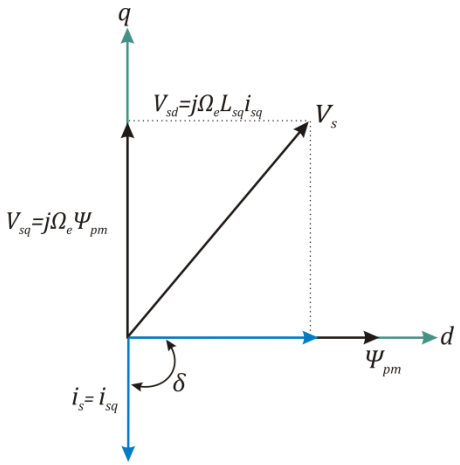

Figure 2.7: Phasor diagram for maximum torque per ampere control in the *d*, *q* reference frame.

By regulating the d-axis current to zero the equations (2.9) and (2.10), for active and reactive power, simplify to the following:

$$P_{(dq)} = \frac{3}{2}(V_{sq} i_{sq}) \tag{2.15}$$

$$Q_{(dq)} = -\frac{3}{2}(V_{sd} i_{sq}) \tag{2.16}$$

It can be noted from equation (2.16) that with this control strategy the reactive power demanded by the generator is not zero. This will increase the converter rating and is a disadvantage of the maximum torque per ampere control strategy. The need to supply reactive power also means that the use of an active rectifier, capable of bidirectional power flow, is a necessity. This control scheme cannot be implemented using a diode rectifier. The advantage of this control strategy is an optimal utilization of the generator, because the total supply current is used for torque production.

- **Unity power factor control** - The aim of this control strategy is to utilise the full Volt Ampere (VA) rating of the converter for active power transfer. The q-axis current is used to control the electromagnetic torque while the d-axis compensates the reactive power demand of the generator. Maintaining unity power factor reduces the amount of current in the stator windings, as they only have to carry the active power obtained in the conversion. This reduces resistive losses in the stator winding and improves efficiency. For a given power output the VA rating of the converter is also minimised. The disadvantage of this control strategy is that it does not use all of the stator current to generate torque (Krishnan, 2010). Thus, for the same generator

torque, its efficiency is lower than that achieved by the maximum torque per ampere control strategy. The phasor diagram for unity power factor control is shown in Figure 2.8.

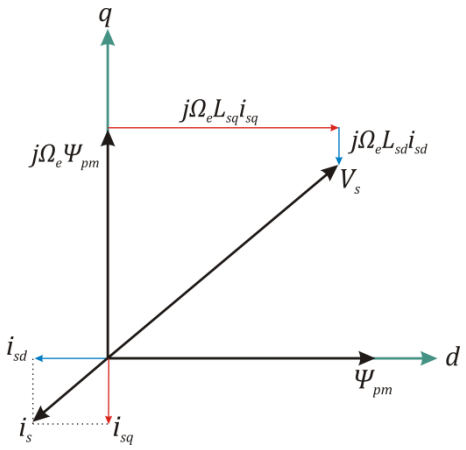

Figure 2.8: Phasor diagram for unity power factor control in the *d*, *q* reference frame.

2.2.2 Generator-Side Converter Control

In this work the maximum torque per ampere control strategy was used to control the speed of the PMSG. The control strategy is presented in Figure 2.9. The measured parameters are the stator currents (i_{sa}, i_{sb}, i_{sc}), rotor electrical position (θ_e) and the rotor speed (Ω_g). It is assumed that the rotor position is measured using an encoder mounted on the rotor.

The controller consists of an inner current loop and an outer torque loop. The measured generator speed is read into a lookup table, which outputs a torque demand (τ_d) according to equation (2.8). This ensures that the turbine follows an optimal torque vs. speed curve that maximises the output power. The torque-producing current reference (i_{sq}^*) is obtained by dividing the torque reference by the generator torque constant (K_t). The parameters for the generator are given in Appendix A.3.

The inner current loop ensures that the q-axis component of the measured current (i_{sq}) reaches the q-axis current reference (i_{sq}^*) and the d-axis component of the measured current (i_{sd}) reaches the d-axis current reference (i_{sd}^*). The d-axis current reference (i_{sd}^*) is set to zero so the maximum torque to current ratio is obtained. The d-axis and q-axis currents are obtained from the measured three phase stator currents (i_{sa}, i_{sb}, i_{sc}) using the transformation given by:

$$\begin{bmatrix} I_{sd} \\ I_{sq} \end{bmatrix} = \frac{2}{3} \begin{bmatrix} \sin(\theta_e) & \sin\left(\theta_e - \frac{2\pi}{3}\right) & \sin\left(\theta_e + \frac{2\pi}{3}\right) \\ \cos(\theta_e) & \cos\left(\theta_e - \frac{2\pi}{3}\right) & \cos\left(\theta_e + \frac{2\pi}{3}\right) \end{bmatrix} \begin{bmatrix} i_{sa} \\ i_{sb} \\ i_{sc} \end{bmatrix} \tag{2.17}$$

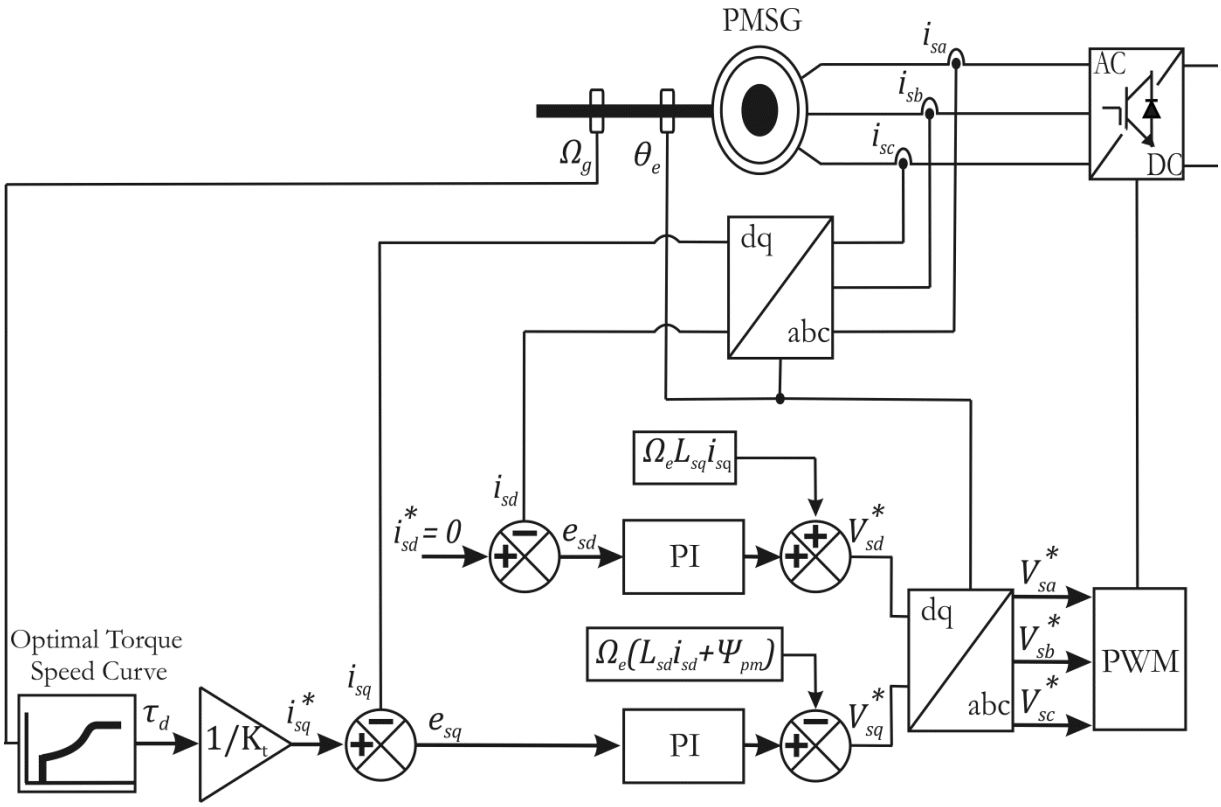

Figure 2.9: Field oriented control scheme for PMSG.

The d-axis and q-axis voltage references V_{sq}^* and V_{sd}^* are generated as below:

$$V_{sd}^* = K_{P_i} e_{sd} + K_{I_i} \int e_{sd} dt + \Omega_e L_{sq} i_{sq} \tag{2.18}$$

$$V_{sq}^* = K_{P_i} e_{sq} + K_{I_i} \int e_{sq} dt - \Omega_e \left(L_{sd} i_{sd} + \Psi_{pm} \right) \tag{2.19}$$

where K_{P_i} and K_{I_i} are the proportional and integral gains of the respective PI controllers. e_{sd} is the d-axis current error $(i_{sd}^* - i_{sd})$. e_{sq} is the q-axis current error $\left(i_{sq}^* - i_{sq}\right)$. The parts on the right hand side of equations (2.18) and (2.19) are decoupling terms. These have little impact on the control but will affect the transient response of the system (Twining & Holmes, 2003).

Finally the d-axis and q-axis voltages are transformed back to a-b-c reference voltages $(V_{sa}^*, V_{sb}^*, V_{sc}^*)$ using the transformation of (2.20). The reference voltages are then used to generate the PWM signals for the generator-side converter.

$$\begin{bmatrix} V_{sa}^* \\ V_{sb}^* \\ V_{sc}^* \end{bmatrix} = \frac{2}{3} \begin{bmatrix} \sin(\theta_e) & \cos(\theta_e) & 1 \\ \sin\left(\theta_e - \frac{2\pi}{3}\right) & \cos\left(\theta_e - \frac{2\pi}{3}\right) & 1 \\ \sin\left(\theta_e + \frac{2\pi}{3}\right) & \cos\left(\theta_e + \frac{2\pi}{3}\right) & 1 \end{bmatrix} \begin{bmatrix} V_{sd} \\ V_{sq} \\ 0 \end{bmatrix} \tag{2.20}$$

Generator-Side Controller design – Current Loop

Figure 2.10 shows the block diagram for the inner current control loop (i_{sq}) of the generator-side converter. The PI controller generates the voltage reference V_{sq}^{*} which is sent to the voltage source converter (VSC). The output from the VSC is sent to the plant.

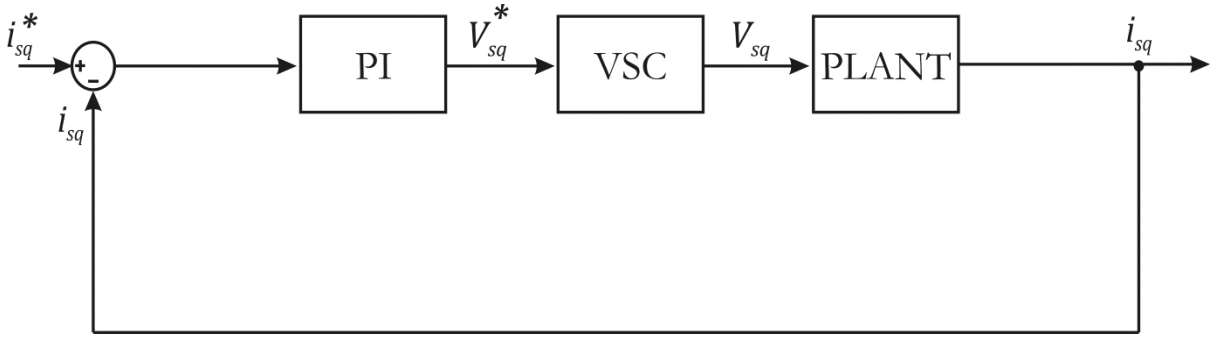

Figure 2.10: Control diagram for *q*-axis current loop.

The transfer function of the PI controller is given as:

$$PI_{isq\_gen}(s) = K_p + \frac{K_I}{s} \tag{2.21}$$

where K_p is the proportional gain and K_I is the integral gain.

The VSC is modelled as a first order lag given as:

$$G_{VSC}(s) = \frac{V_{sq}(s)}{V_{sq}^{*}(s)} = \frac{1}{0.5\,T_s s + 1} \tag{2.22}$$

where T_s is the sampling delay of the PWM converter. The paramaters for the VSC are given in Appendix A.4.

The transfer function of the plant is given as follows (Pena, Clare & Asher, 1996):

$$G_{plant}(s) = \frac{i_{sq}(s)}{V_{sq}(s)} = \frac{1}{L_{sq}s + R_s} \tag{2.23}$$

where R_s is the generator stator resistance and L_{sq} is the generator stator inductance in the q-axis. The parameters for the generator are given in Appendix A.3.

The controller design was done using the frequency response method. This method relies upon adjusting the open loop frequency response characteristic in order to achieve the desired closed loop performance of the system (Ogata, 1996). The following criteria were specified before designing the controller in Figure 2.10:

- Closed loop response should have zero steady state error.
- Maximum overshoot of the step response should be limited to less than 5%.
- The bandwidth should be high enough to ensure that decoupling with the mechanical system is achieved.

To find the damping ratio corresponding to an overshoot of 5% equation (2.24), relating percentage overshoot $(\%OS)$ and damping ratio (ζ), was used. The equation is (Nise, 2004)

$$\zeta = \frac{-\ln(\%OS/100)}{\sqrt{\pi^2 + \ln(\%OS/100)^2}} \tag{2.24}$$

Applying equation (2.24) the damping ratio corresponding to an overshoot of 5% is 0.69. Having obtained the damping ratio it is possible to calculate the phase margin required to give the desired overshoot. The phase margin (M_{ph}) is related to the damping ratio as follows (Nise, 2004):

$$M_{ph} = \tan^{-1}\frac{2\zeta}{\sqrt{-2\zeta^2 + \sqrt{1 + 4\zeta^4}}} \tag{2.25}$$

Equation (2.25) reveals that the required phase margin must be at least 65 degrees to ensure that the overshoot is within limits. Through bode shaping a response that meets the specifications, was achieved with a PI control structure given as follows:

$$PI_{isq\_gen}(s) = \frac{0.62s + 3}{s} \tag{2.26}$$

From the frequency response curves of Figure 2.11 (a) it is clear that the controller gives a good response. The phase margin is 85 degrees, meaning that the overshoot is well within the 5% limit. This is reflected in the step response of Figure 2.11 (b). The system achieves a bandwidth of ≈120Hz leading to a settling time of ≈ 8 ms which can be seen in the step response of Figure 2.11 (b).

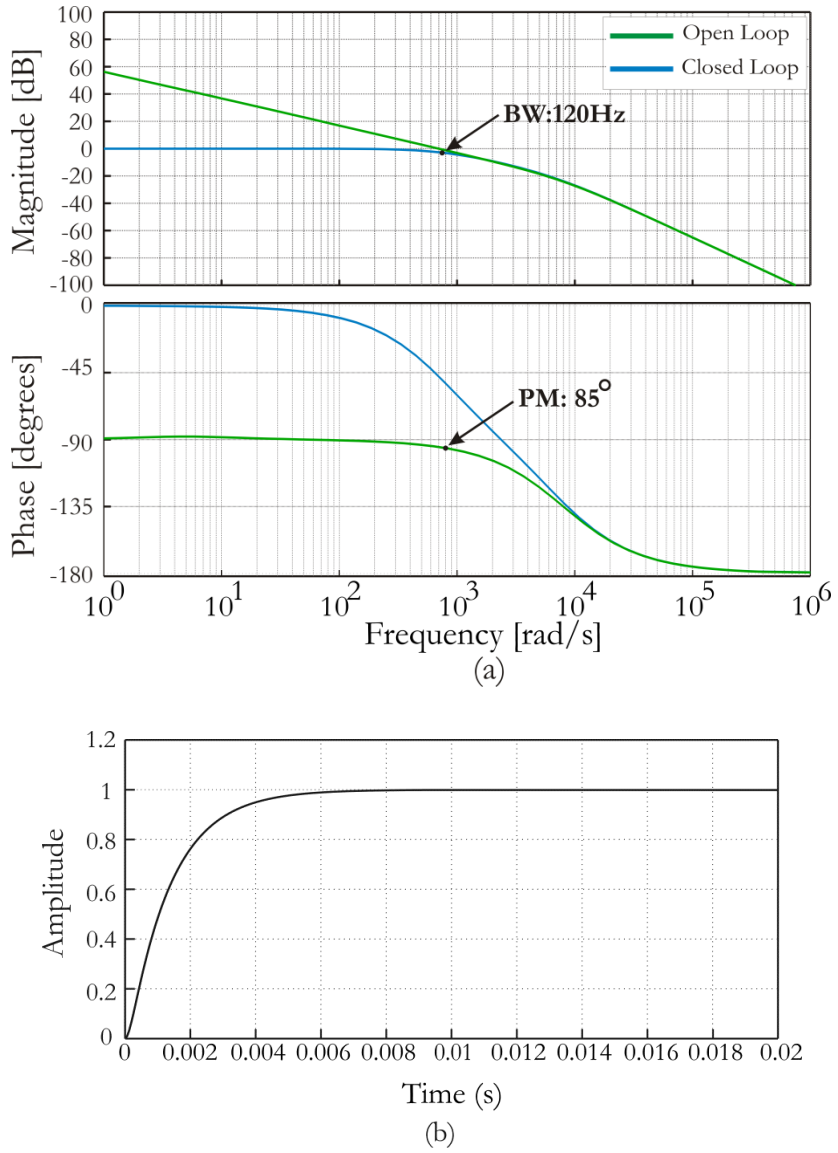

Figure 2.11: (a) Bode plot showing the frequency response of the generator-side q-axis current control loop $\left(PI_{isq\_gen}(s) * G_{VSC}(s) * G_{plant}(s)\right)$ in both closed loop and open loop. (b) Generator-side current control loop step response.

Since the PMSG is non-salient $(L_{sq} = L_{sd})$ the dynamics of the q-axis control loop are considered the same as those of the d-axis; therefore, the same control parameters are used for the d-axis and the q-axis control loops. The control parameters are summarised in Table 2.1.

Controller	K_p	K_I
PI_{isq_gen}	0.62	3
PI_{isd_gen}	0.62	3

Table 2-1: PI controller parameters for the generator side converter

2.2.3 Grid-Side Converter Control

The field oriented control method, although originally developed for motor control applications, can also be used to enable the grid-side converter to control the flow of active and reactive power. When used in this way it is referred to as vector control. A schematic of the grid-side converter is given in Figure 2.12.

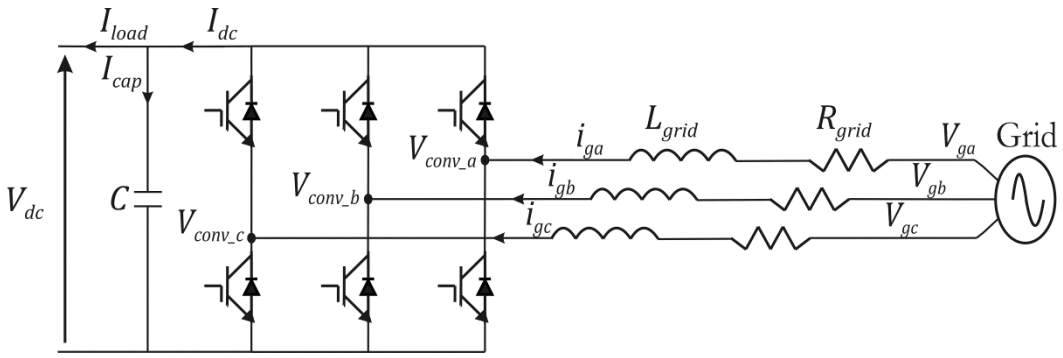

Figure 2.12: Grid side converter arrangement.

From Figure 2.12 the grid voltages $V_{ga}, V_{gb,} V_{gc}$ can be expressed as follows:

$$V_{ga} = i_{ga}R_{grid} + L_{grid}\frac{di_{ga}}{dt} + V_{conv\_a} \tag{2.27}$$

$$V_{gb} = i_{gb}R_{grid} + L_{grid}\frac{di_{gb}}{dt} + V_{conv\_b} \tag{2.28}$$

$$V_{gc} = i_{gc}R_{grid} + L_{grid}\frac{di_{gc}}{dt} + V_{conv\_c} \tag{2.29}$$

These equations in the d, q reference frame are given as follows (Pena, Clare & Asher, 1996):

$$V_d = R_{grid}i_d + L_{grid}\frac{di_d}{dt} - \Omega_{grid}L_{grid}i_{q+}V_{d\_conv} \tag{2.30}$$

$$V_q = R_{grid}i_q + L_{grid}\frac{di_q}{dt} + \Omega_{grid}L_{grid}i_{d+}V_{q\_conv} \tag{2.31}$$

where Ω_{grid} is the synchronous frequency, V_d and V_q are the grid voltages in the d, q reference frame, V_{d_conv} and V_{q_conv} are the converter voltages in the d, q reference frame and i_d and i_q are the grid currents in the d, q reference frame. L_{grid} and R_{grid} are the inductance and resistance between the converter and grid. All parameters of the grid-side converter are in Appendix A4.

If the converter is lossless then a power balance relationship between the power stored in the DC link and the power flowing to the grid can be given as:

$$P = \frac{3}{2}\left(V_d i_d + V_q i_q\right) = V_{dc} I_{dc} \tag{2.32}$$

The current flowing in the DC link can be given as:

$$I_{dc} = C\frac{dV_{dc}}{dt} + I_{load} \tag{2.33}$$

where C is the DC link capacitance, V_{dc} is the DC link voltage, I_{dc} and I_{load} are the DC link current and the load current as shown in Figure 2.12.

If the d-axis is assumed to be aligned with the grid voltage vector and the q-axis leads the d-axis by 90 degrees then $V_q = 0$. Therefore, independent control of the active and reactive power can be achieved by controlling the d and q-axis currents as shown by equations (2.34) and (2.35) (Chinchilla, Arnaltes & Burgos, 2006).

$$P_g = \frac{3}{2}\left(V_d i_d\right) \tag{2.34}$$

$$Q_g = \frac{3}{2}\left(V_d i_q\right) \tag{2.35}$$

It is clear from equations (2.34) and (2.35) that the active power can be controlled solely by the d-axis current and the reactive power can be controlled solely by the q-axis current. The phasor diagram for the field oriented control scheme of the grid-side converter is shown in Figure 2.13, where it is seen that the grid voltage vector contains only a d-axis component.

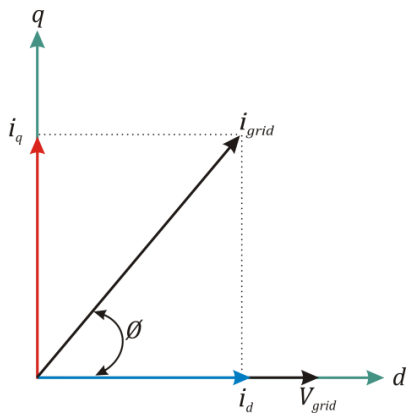

Figure 2.13: Phasor diagram for vector control of grid-side converter in the *d*, *q* reference frame.

The vector control strategy implemented on the grid-side converter controls the active power flow into the grid, via regulation of the DC link voltage, using the d-axis current. The reactive power flow is controlled using the q-axis current as given by equation (2.35).

Figure 2.14 shows the vector control scheme for the grid-side converter. Two control loops are used to control the active and reactive power. A cascaded control loop is used to control the active power flow to the grid, whereby the outer voltage control loop sets the d-axis current reference (i_d^*) of the inner loop. The reactive power is regulated by setting a q-axis current reference (i_q^*). In some cases the grid operator may require the turbine to supply reactive power compensation (Michalke, Hansen, 2009). However, under normal operation the converter will transfer all the active power generated by the TST to the grid; therefore, in this case the q-axis current reference is set to zero. Figure 2.14 shows the situation under normal conditions where the turbine is operating at unity power factor.

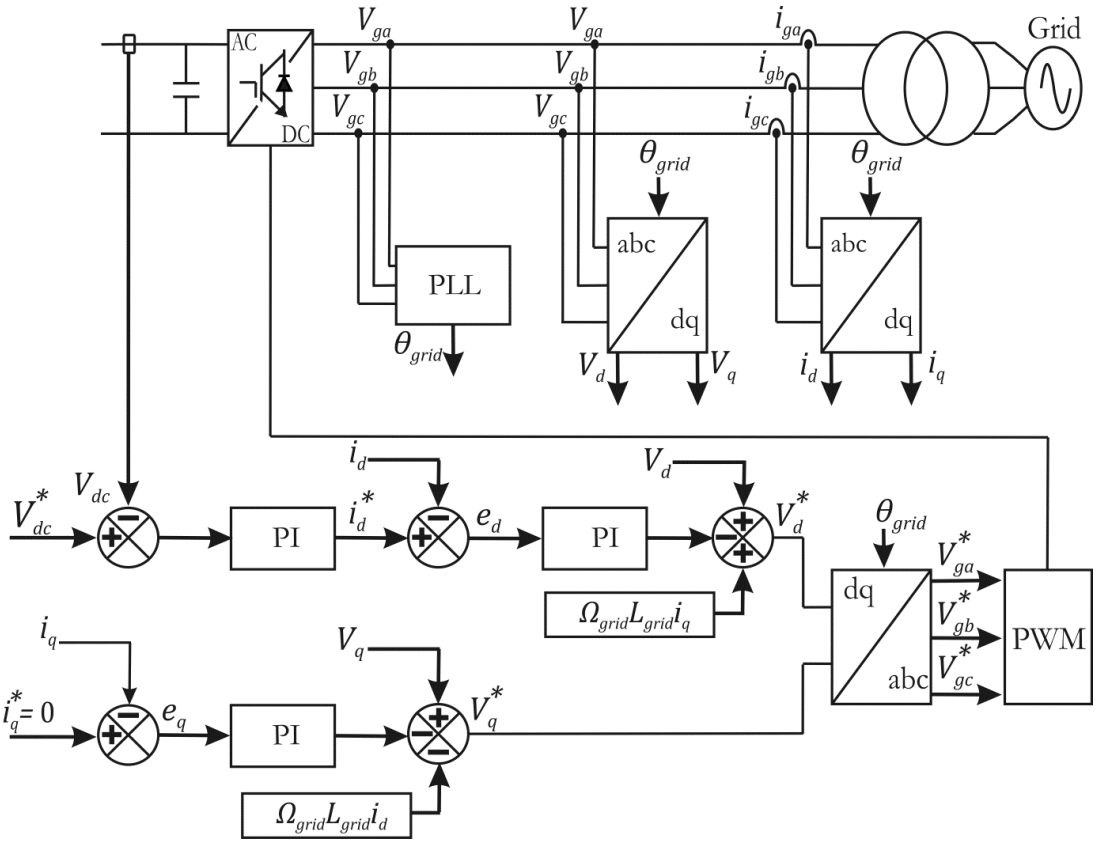

Figure 2.14: Vector control scheme for grid-side converter.

The values for the d-axis and q-axis currents and voltages are obtained from the measured three phase values using the transformation given by:

$$\begin{bmatrix} I_d \\ I_q \end{bmatrix} = \frac{2}{3}\begin{bmatrix} \sin(\theta_{grid}) & \sin\left(\theta_{grid} - \frac{2\pi}{3}\right) & \sin\left(\theta_{grid} + \frac{2\pi}{3}\right) \\ \cos(\theta_{grid}) & \cos\left(\theta_{grid} - \frac{2\pi}{3}\right) & \cos\left(\theta_{grid} + \frac{2\pi}{3}\right) \end{bmatrix}\begin{bmatrix} i_{ga} \\ i_{gb} \\ i_{gc} \end{bmatrix} \tag{2.36}$$

where θ_{grid} is the grid phase angle obtained using a phase locked loop (PLL). The PLL was implemented using a standard block from the SimPowerSystems library in Simulink®. The d-axis and q-axis current loops are identical, with each loop generating a voltage reference (V_q^*, V_d^*) as described by equations (2.37) and (2.38).

$$V_d^* = V_d + \Omega_{grid} L_{grid} i_q - (K_{P_i} e_d + K_{I_i} \int e_d dt) \tag{2.37}$$

$$V_q^* = V_q - \Omega_{grid} L_{grid} i_d - (K_{P_i} e_q + K_{I_i} \int e_q dt) \tag{2.38}$$

K_{P_i} and K_{I_i} are the proportional and integral gains of the respective PI controllers, e_d is the d-axis current error $(i_d^* - i_d)$ and e_q is the q-axis current error $\left(i_q^* - i_q\right)$. To decouple the voltages and allow for independent control of the active and reactive power decoupling terms, $\Omega_{grid} L_{grid} i_q$ and $-\Omega_{grid} L_{grid} i_d$, are included in both equation (2.37) and (2.38). Feed-forward voltage terms (V_d, V_q) are also added to each voltage reference. Decoupling and voltage feed-forward are commonly used and are known to improve the transient response of the system (Blaabjerg et al, 2006; Twining & Holmes, 2003)

Finally the d-axis and q-axis voltages are transformed back to a-b-c reference voltages $(V_{ga}^*, V_{gb}^*, V_{gc}^*)$ using the transformation of (2.39). The grid phase angle (θ_{grid}) is used to ensure synchronisation. The reference voltages are then used to generate the PWM signals for the grid-side converter.

$$\begin{bmatrix} V_{ga}^* \\ V_{gb}^* \\ V_{gc}^* \end{bmatrix} = \frac{2}{3}\begin{bmatrix} \sin(\theta_{grid}) & \cos(\theta_{grid}) & 1 \\ \sin\left(\theta_{grid} - \frac{2\pi}{3}\right) & \cos\left(\theta_{grid} - \frac{2\pi}{3}\right) & 1 \\ \sin\left(\theta_{grid} + \frac{2\pi}{3}\right) & \cos\left(\theta_{grid} + \frac{2\pi}{3}\right) & 1 \end{bmatrix}\begin{bmatrix} V_d \\ V_q \\ 0 \end{bmatrix} \tag{2.39}$$

Grid-Side Controller Design – Current Loop

The block diagram for the inner current control loop (i_d) of the grid-side converter has the same structure as the inner current loop for the generator-side converter (Figure 2.10). The transfer functions are given as follows:

$$PI_{id\_grid}(s) = K_p + \frac{K_I}{s} \tag{2.40}$$

$$G_{VSC}(s) = \frac{V_d(s)}{V_d^*(s)} = \frac{1}{0.5\,T_s s + 1} \tag{2.41}$$

$$G_{plant}(s) = \frac{i_d(s)}{V_d(s)} = \frac{1}{L_{grid}s + R_{grid}} \tag{2.42}$$

All parameters for the converter and grid connection are in Appendix A4. The controller was designed using the same procedure as that used for the generator-side converter. The following criteria were specified before designing the controller:

- Closed loop response should have zero steady state error.
- Maximum overshoot of the step response should be limited to less than 5%.
- The bandwidth should be high enough to ensure that the inner current loop is decoupled from the outer voltage control loop. Thus a minimum bandwidth of 250 Hz was specified.

Once again a damping ratio of 0.69 was chosen to ensure an overshoot of less than 5%, the resulting transfer function of the PI controller $\left(PI_{id\_grid}(s)\right)$ was

$$PI_{id\_grid}(s) = \frac{1.01s + 70}{s} \tag{2.43}$$

From the frequency response curves of Figure 2.15 (a) it is clear that the controller gives a good response. The phase margin is 78 degrees and the overshoot is well within the 5% limit. This is reflected in the step response of Figure 2.15 (b). The system achieves a bandwidth of ≈ 248Hz leading to a settling time of ≈ 40 ms which can be seen in the step response of Figure 2.15 (b). It should be noted that the control parameters used for the d-axis current loop are also applicable to the q-axis.

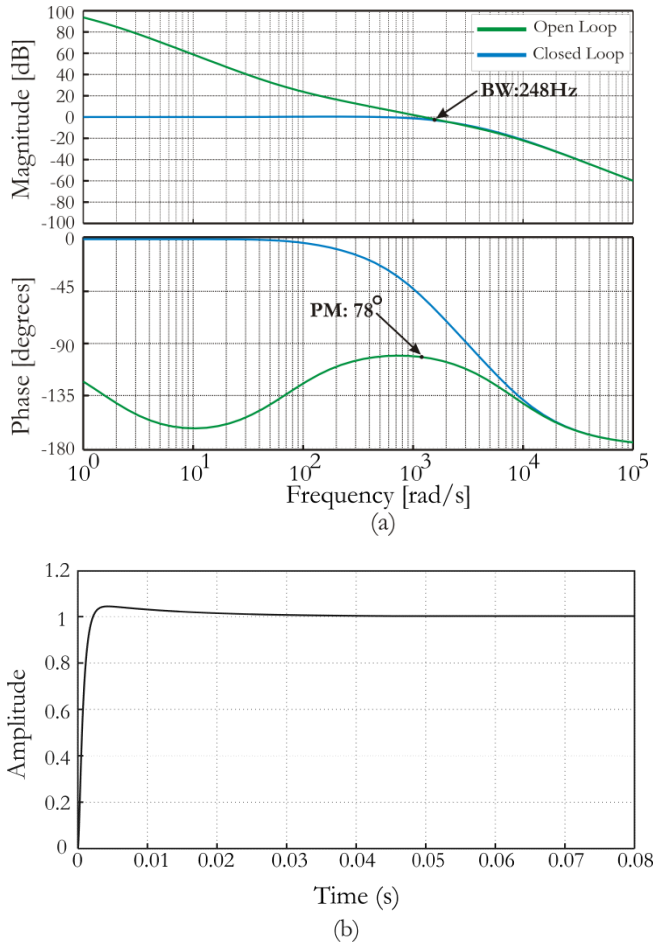

Figure 2.15: (a) Bode plot showing frequency response of the grid-side current control loop $\left(PI_{id\_grid}(s) * G_{VSC}(s) * G_{plant}(s)\right)$ in closed loop and open loop (b) Grid-side current control loop step response.

Grid-Side Controller Design – Voltage Loop

The outer voltage control loop generates the current reference for the inner current loop (Figure 2.16). The inner loop must be faster to ensure that there is no interaction with the outer voltage loop. As a rule of thumb the bandwidth of the inner loop should be 5-20 times faster than that of the outer loop (Liserre, Blaabjerg & Aquila, 2007). If this is the case then, for the purposes of tuning the outer loop, the inner loop can be approximated as a unity gain.

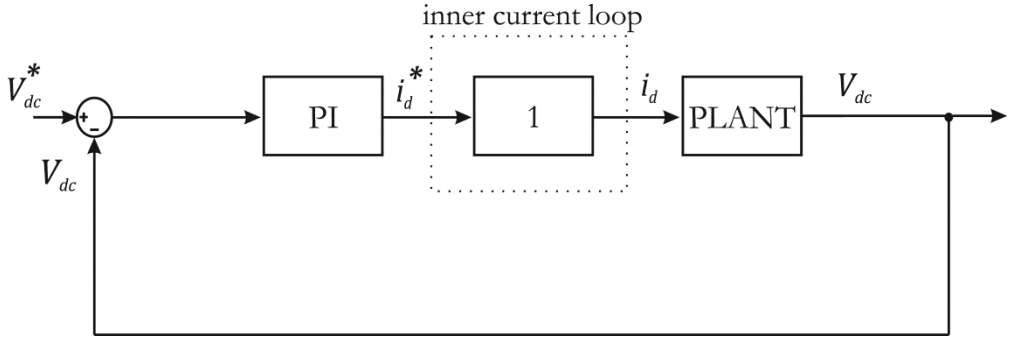

Figure 2.16: Control diagram for outer voltage control loop of grid-side converter.

The dynamics of the plant, relating the DC link voltage (V_{dc}) to the d-axis current (i_d), can be derived from equations (2.32) - (2.34) giving:

$$C\frac{dV_{dc}}{dt} = \frac{3}{2}\cdot\frac{V_d}{V_{dc}}i_d - I_{load} \tag{2.44}$$

The minimum DC link voltage required is determined by the grid side voltage and the amplitude modulation ratio of the converter as (Mohan, Undeland & Robbins, 2002):

$$V_{dc} = \frac{2\hat{V}_{grid\_ph}}{M_a} \tag{2.45}$$

where M_a is the amplitude modulation ratio, $\hat{V}_{grid\_ph}$ is the peak grid phase voltage. Rearranging (2.45) the peak value of the fundamental voltage component in one inverter leg is given by:

$$\hat{V}_{grid\_ph} = M_a\frac{V_{dc}}{2} \tag{2.46}$$

Since the reference frame is oriented along the grid voltage $V_q = 0$ and the grid voltage vector is:

$$\hat{V}_{grid\_ph} = V_d + j0 \tag{2.47}$$

therefore the following is true:

$$V_d = \hat{V}_{grid\_ph} = M_a\frac{V_{dc}}{2} \tag{2.48}$$

By substituting (2.48) into (2.44) it is possible to express the DC link voltage as:

$$C\frac{dV_{dc}}{dt} = \frac{3M_a}{4}i_d - I_{load} \tag{2.49}$$

Using (2.49) a Laplace domain transfer function relating the d-axis current (i_d) to the DC link voltage (V_{dc}), can be given as:

$$\frac{V_{dc}(s)}{i_d(s)} = \frac{3}{4}\cdot\frac{M_a}{Cs} \tag{2.50}$$

The design criteria for the voltage controller were specified as follows:

- Closed loop response should have zero steady state error.
- Maximum overshoot of the step response should be limited to less than 5%.
- The bandwidth should be 20 times lower than that of the inner current loop.

The resulting transfer function of the PI controller $\left(PI_{V_{dc}}(s)\right)$ is:

$$PI_{V_{dc}}(s) = \frac{9.4s + 140}{s} \tag{2.51}$$

The frequency response curves of Figure 2.17 (a) show that the controller gives a good response that meets the design criteria. The phase margin is 78 degrees and the overshoot is within the 5% limit. This is reflected in the step response of Figure 2.17 (b). The system achieves a bandwidth of ≈ 12.3Hz, which is approximately 20 times slower than that of the inner current loop (Figure 2.15 (a))

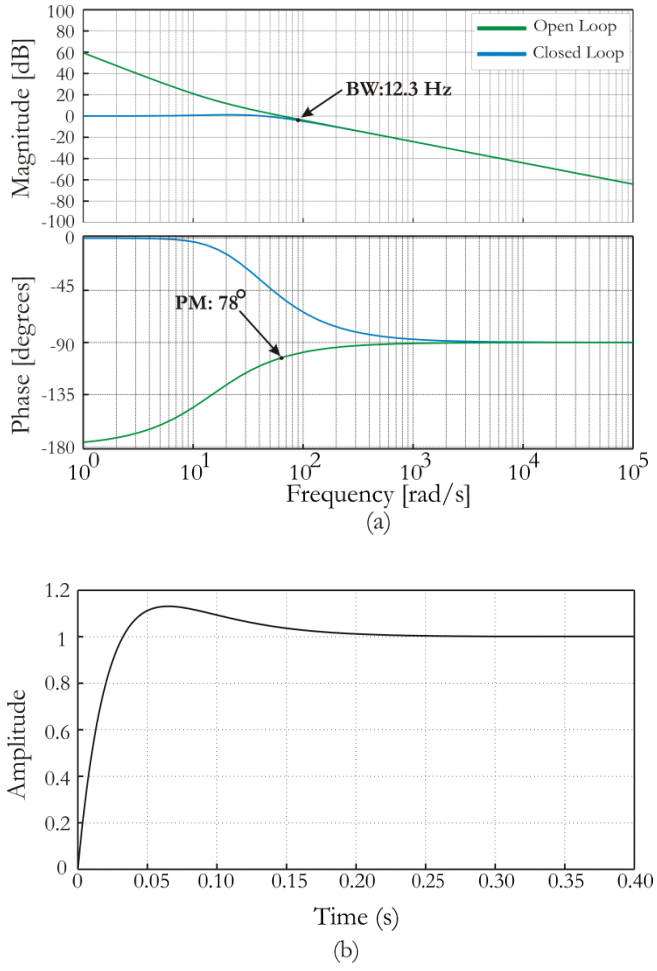

Figure 2.17: (a) Bode plot of the grid-side voltage control loop (b) Voltage control loop step response.

The parameters for the current and DC-voltage controllers of the grid-side converter are summarised in Table 2.2.

Controller	K_p	K_I
PI_{id_grid}	1.01	70
PI_{iq_grid}	1.01	70
$PI_{V_{dc}}$	9.4	140

Table 2-2: PI controller parameters for the grid side converter

2.3 Simulation Results and Discussion

2.3.1 Simulink® Modelling

The full TST model (shown in figure 2.1) was implemented in Simulink® and a block diagram of the implementation is shown in Figure 2.18.

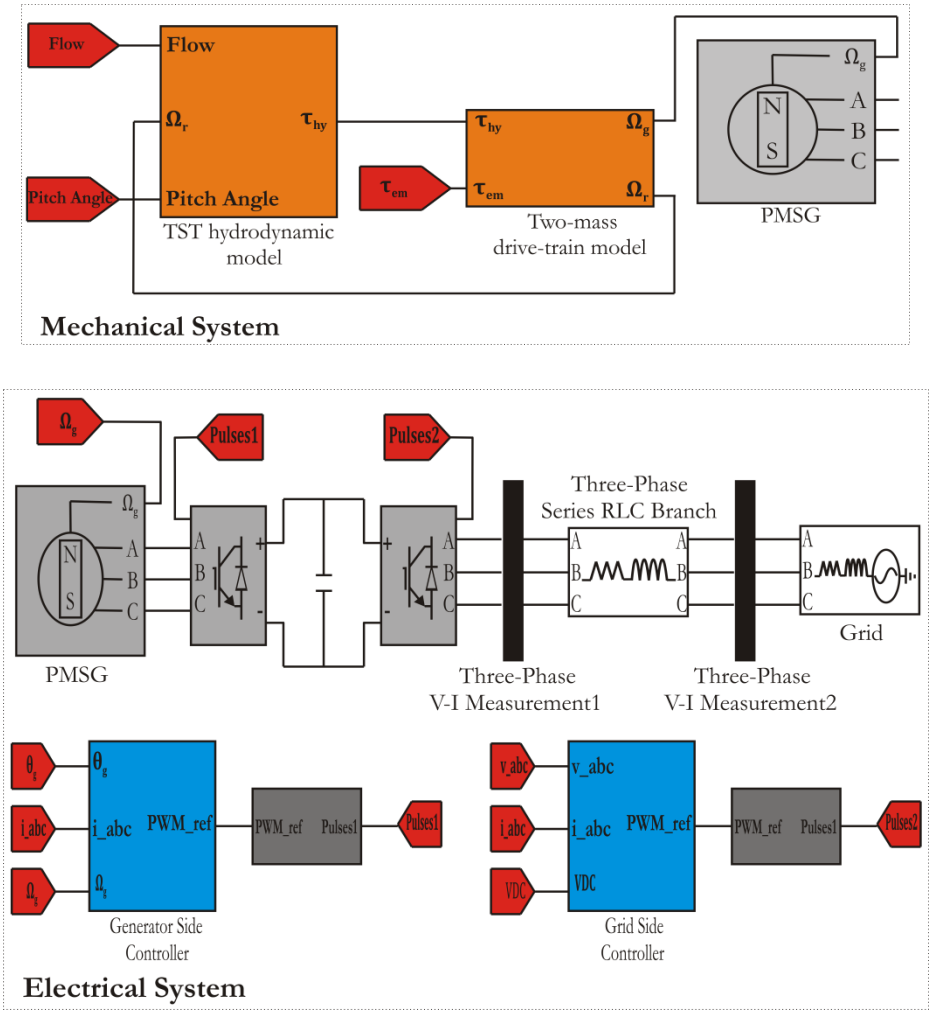

Figure 2.18: Simulink implementation of TST model.

2.3.2 Simulation Results

The aim of simulating the model was to verify the performance of the proposed control strategies when the turbine is operating in below rated flow speeds and the rotor speed is being varied to maintain the optimum C_p value. During this simulation the pitch angle was set to zero, which is a valid assumption when the turbine is operating in below rated flow speeds.

Figure 2.19(a) shows that the turbine is initially experiencing a flow speed of 1m/s and is assumed to be operating at steady state. At the 4 second mark a step change in the flow speed is applied from 1m/s to 2.3m/s. This causes an abrupt change in the hydrodynamic torque (τ_{hy}) shown in Figure 2.20(a). The resulting imbalance between the hydrodynamic torque and the generator torque causes the generator to be accelerated at a rate proportional to the torque difference $(\tau_{hy} - \tau_{em})$. The generator speed (ω_g), which is impeded by inertia, increases as shown in Figure 2.19(b).

The generator torque (τ_{em}) is controlled in accordance with equation 2.8 and increases as shown in Figure 2.20(b). The increasing generator speed causes the hydrodynamic torque to drop until eventually a new steady state operating point is reached at about 4.8 seconds, once the hydrodynamic torque and the generator torque are balanced. The same process occurs at the 8 second mark when the flow reduces from 2.3m/s to 1 m/s only this time the generator is decelerated at a rate proportional to the torque difference $(\tau_{hy} - \tau_{em})$.

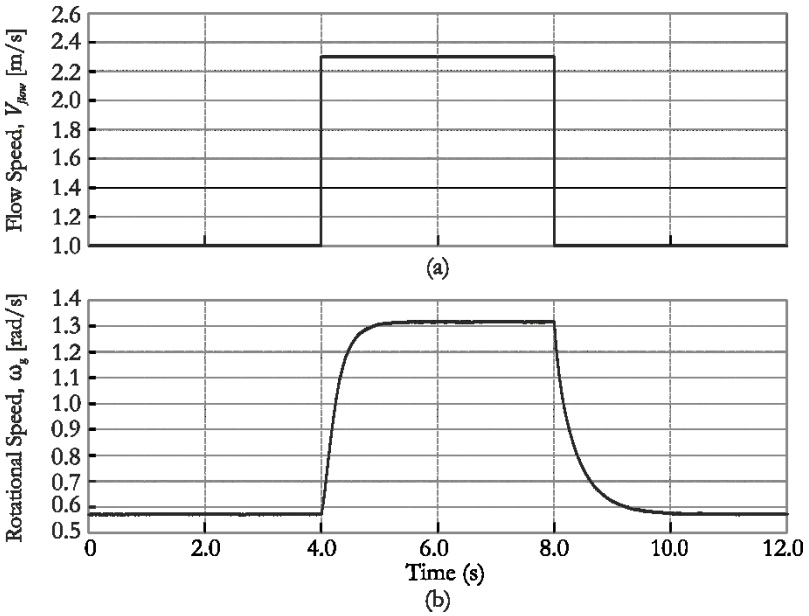

Figure 2.19: (a) Step change in flow speed (V_{flow}). (b) Response of generator rotational speed (ω_g) to step change in flow speed.

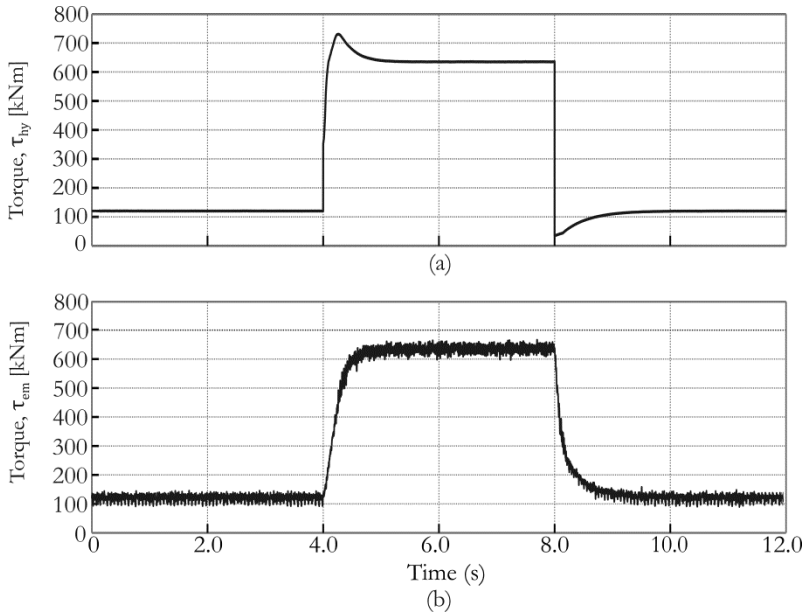

Figure 2.20: (a) Response of hydrodynamic torque (τ_{hy}) to a step change in flow speed (V_{flow}). (b) Response of generator torque (τ_{em}) to a step change in flow speed.

The DC link voltage and current are shown in Figure 2.21 (a) and (b). The controller regulates the DC link voltage at 1400V. The ripple increases slightly after the increase in current at the 4 second mark; however, it remains within 0.5% for the duration of the simulation, which is considered satisfactory.

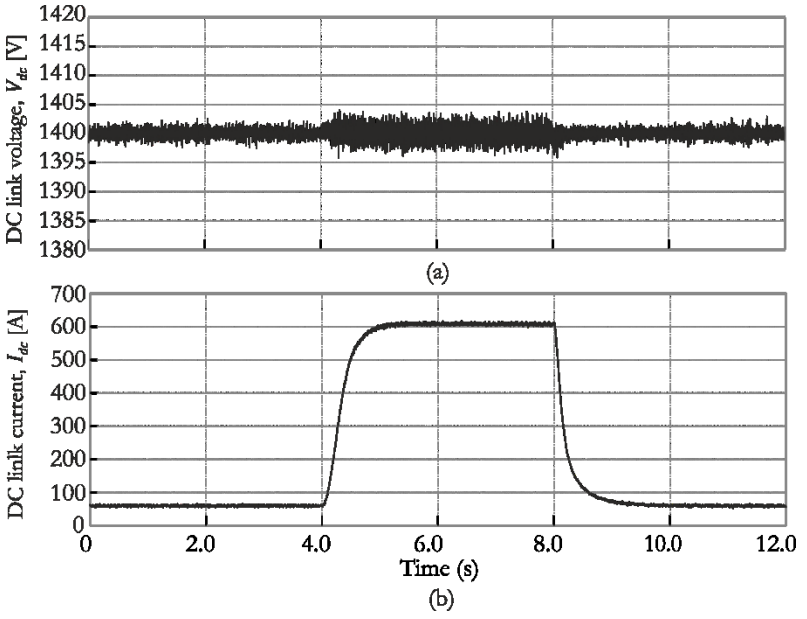

Figure 2.21: (a) DC link voltage (V_{dc}), (b) DC link current (I_{dc}).

Figures 22 (a) and (b) show the d-axis and q-axis currents of the generator. The d-axis current reference is set to zero in order to operate the generator at the maximum torque/ampere ratio. The q-axis current is directly proportional to the electromagnetic torque, which can be seen in

Figure 2.22(a) where the increase in i_{sq} causes a corresponding increase in the electromagnetic torque in Figure 2.20(b). The ripple is approximately 5%.

Figures 2.22 (c) and (d) show the d-axis and q-axis currents on the grid-side. In this simulation the aim was to transfer all the active power from the turbine to the grid; therefore, the q-axis current reference was set to zero. The active power is controlled via the d-axis current which increases at the 4 second mark following the increase in power coming from the turbine. The ripple is approximately 7%. Figure 2.23 shows the active and reactive power transferred to the grid. There is a clear step change in the active power at the 4 second mark, which is proportional to the increase in i_d.

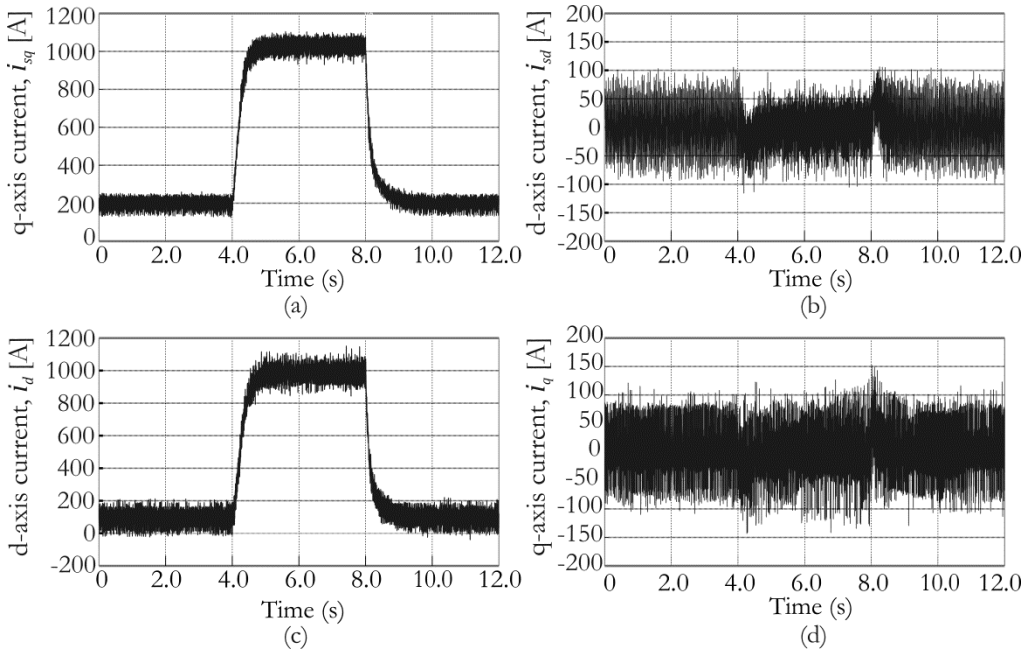

Figure 2.22: (a) q-axis current for generator-side converter. (b) d-axis current for generator-side converter. (c) d-axis current for grid-side converter. (d) q-axis current for grid-side converter.

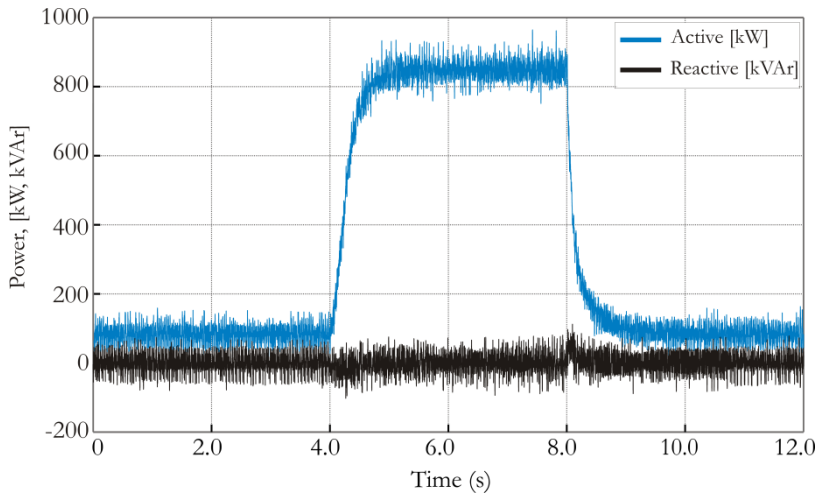

Figure 2.23: Active and reactive power

2.3.3 Discussion

A control scheme that maximises the power output of a TST by allowing the rotor speed to be varied in below rated flow speeds has been developed and simulated. The controller has been applied to a TST incorporating a low speed permanent magnet generator interfaced to the grid through a full-power converter consisting of back-to-back VSCs.

Field oriented control was used for the generator-side converter. Both the maximum torque per ampere and the unity power factor control strategies were investigated. A decision was made to use the maximum torque per ampere control. This controller requires measurements of the generator rotor position and speed, which are obtained using an encoder mounted on the rotor shaft. It is possible to obtain these measurements without the use of an encoder and a number of techniques for estimating the values have been developed (Linke M., 2002; Brahmi J. et al, 2009). However, the implementation of such techniques was considered to be out of the scope of this thesis.

Variable speed operation of the rotor is achieved using the torque of the generator. A lookup table is used to set the generator torque demand based on the rotational speed, thus causing the rotor to track a torque vs. speed trajectory that maximises the output power. Regulation of the torque is achieved using a current control loop.

On the grid-side the control scheme regulates the DC link voltage, thereby controlling the flow of active power to the grid, as well as controlling the flow of reactive power.

Controllers, designed to satisfy a predefined set of criteria, were developed using the frequency response method. When the model was simulated the controllers performed well and were able to maximise power output from the turbine by varying the rotor speed to maintain the optimum TSR. The grid-side converter managed to control the DC link voltage and the power supplied to the grid was kept at unity power factor.

Chapter 3

3. Experimental Testing

Summary:

In this chapter the control strategies developed in Chapter 2 are implemented on a hardware-in-the-loop (HIL) test rig. An overview of the experimental system and the main hardware components is given. The real-time interface used for conducting hardware-in-the-loop experiments, real-time plotting of variables and recording of measurements is presented. Finally, the implementation of the control strategies on the test rig is described and the results of the experiment are discussed.

3.1 Experimental Setup

3.1.1 Overview of Hardware-in-the-Loop Test Rig

The test rig is a scaled prototype designed to emulate the operation of a 1 MW variable speed TST. A block diagram of the test rig is shown in Figure 3.1.

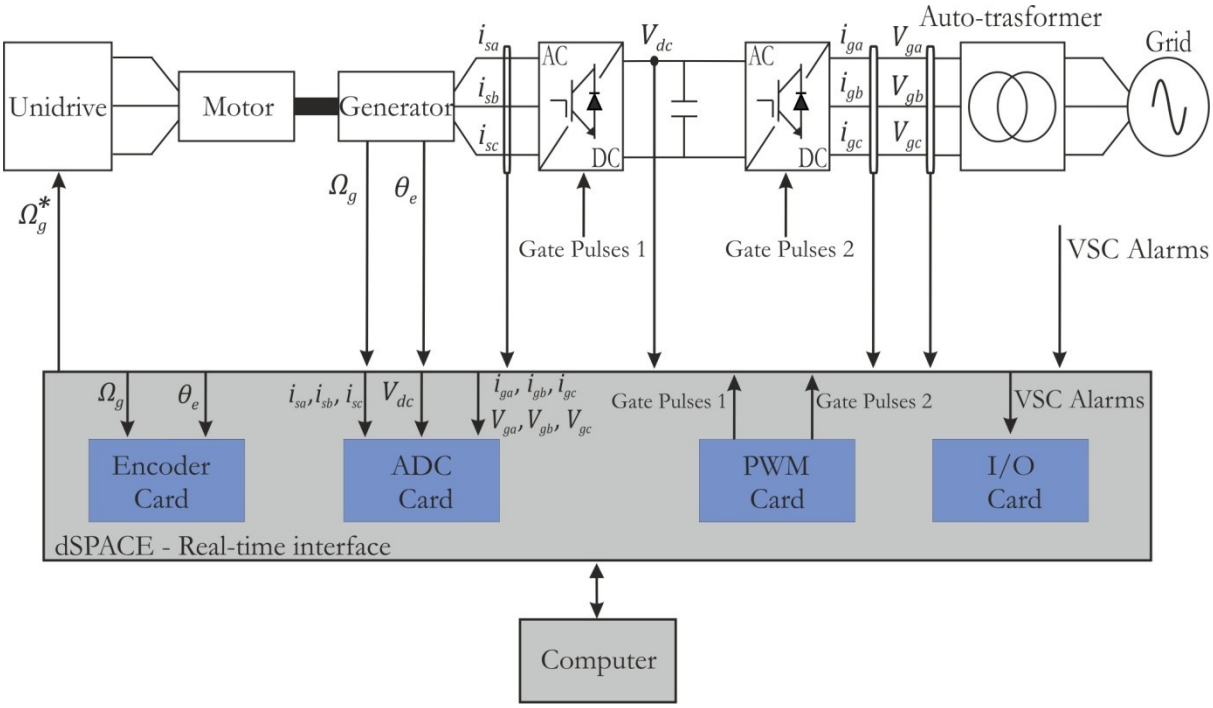

Figure 3.1: Block diagram of experimental test rig.

On the electrical side the rig consists of two VSCs connected in a back-to-back configuration with an intermediate DC link capacitor. The back-to-back converters are connected to the grid through an auto-transformer. The auto-transformer steps down the grid voltages and is used for safety reasons. It means that the DC link can be operated at a lower voltage, making the system safer. Parameters for the auto-transformer and VSCs are given in Appendix C.1.

Two permanently excited synchronous machines joined by a flexible coupling are used to emulate the turbine rotor and generator. A variable speed drive (Unidrive) controls the speed of the motor based on the reference (Ω_g^*) sent to it by the user. The motor essentially emulates the speed of the TST rotor which drives the generator. Both of the machines are rated at 1.2 kW and have integrated encoders which allow the rotor position (θ_e) and speed (Ω_g) to be obtained. These parameters are needed by the controllers. Parameters for the two machines are in Appendix C.1.

Real-time Interface

The control system is first modelled in MATLAB/Simulink®. It is then converted to C code, using the Simulink® real-time workshop toolbox, and loaded onto the dSPACE® unit which contains a high speed digital signal processor. The unit interfaces to a computer allowing the user to monitor and control the system in real-time via the dSPACE® graphical user interface (GUI). The dSPACE® unit also contains a number of data acquisition cards which allow the user to capture and output variables used for control and monitoring purposes. In this experiment four cards were used: an analogue to digital convertor card (DS2003), an encoder interface card (DS3002), a digital input/output (I/O) card (DS4003) and a PWM generator card (DS5101_2). These cards were used to capture and output the variables shown in Figure 3.1.

Measurement Circuits

All of the AC line to line voltage measurements, which are used by the grid-side converter controller, are obtained using the measurement circuit shown in Figure 3.2. The circuit was designed around an ISO124 isolation amplifier. The voltage divider scales down the measured voltage while the amplifier provides isolation between the input and output voltages.

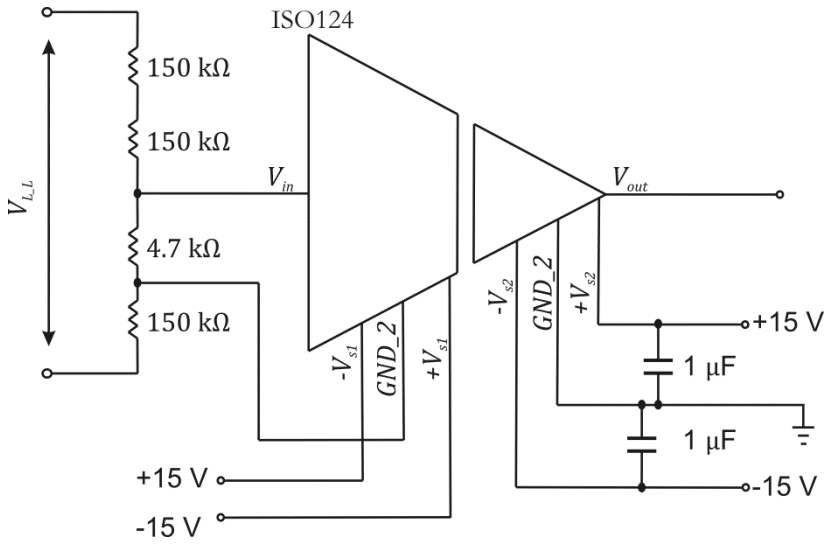

Figure 3.2: AC line to line voltage measurement circuit.

The gain of the circuit is calculated as follows:

$$\frac{V_{out}}{V_{in}} = \frac{4.7\ k\Omega}{R_{total}} = \frac{4.7\ k\Omega}{454.7\ k\Omega} = 0.0103 \tag{3.1}$$

Measurement of the DC link voltage is achieved using a LEM Hall-effect voltage transducer (LV 25-800). The gain of the circuit is as follows:

$$\frac{V_{out}}{V_{in}} = 0.0084 \tag{3.2}$$

The AC current measurements, used by both the grid-side and the generator-side converters, are obtained using a Hall-effect current transducer (LAH 25-NP). These transducers convert the measured currents of the generator and grid to a lower level current and provide galvanic isolation between the input current and the output current. The gain is as follows:

$$\frac{i_{out}}{i_{in}} = 0.001 \tag{3.3}$$

Figure 3.3 shows a picture of the experimental test rig.

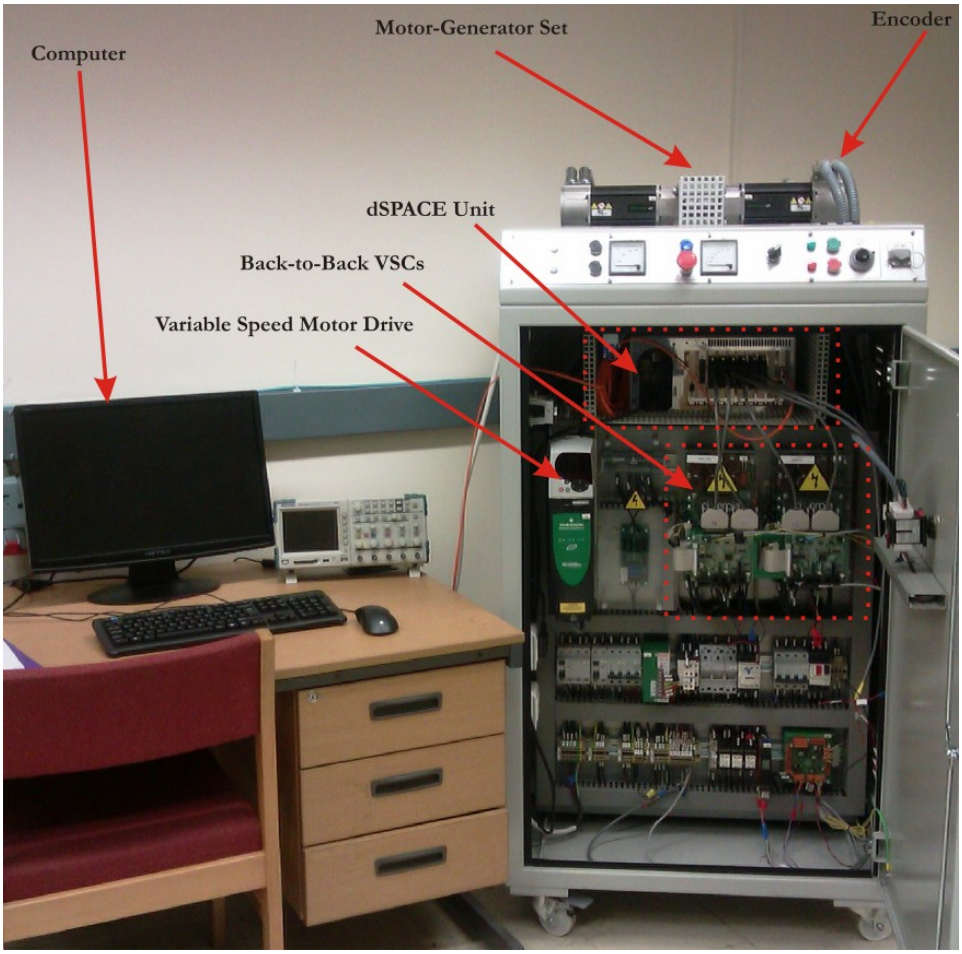

Figure 3.3: Experimental test rig.

3.2 Control System

3.2.1 Generator-Side Converter Control

The parameters of the synchronous machine on the test rig are different to those of the 1 MW machine used in the simulations of Chapter 2; therefore, it was necessary to re-tune the controllers. Furthermore, the output from the 1 MW turbine model was scaled to make it compatible with the 1.2 kW generator on the test rig. A block diagram showing how the generator-side controller was implemented is in Figure 3.4.

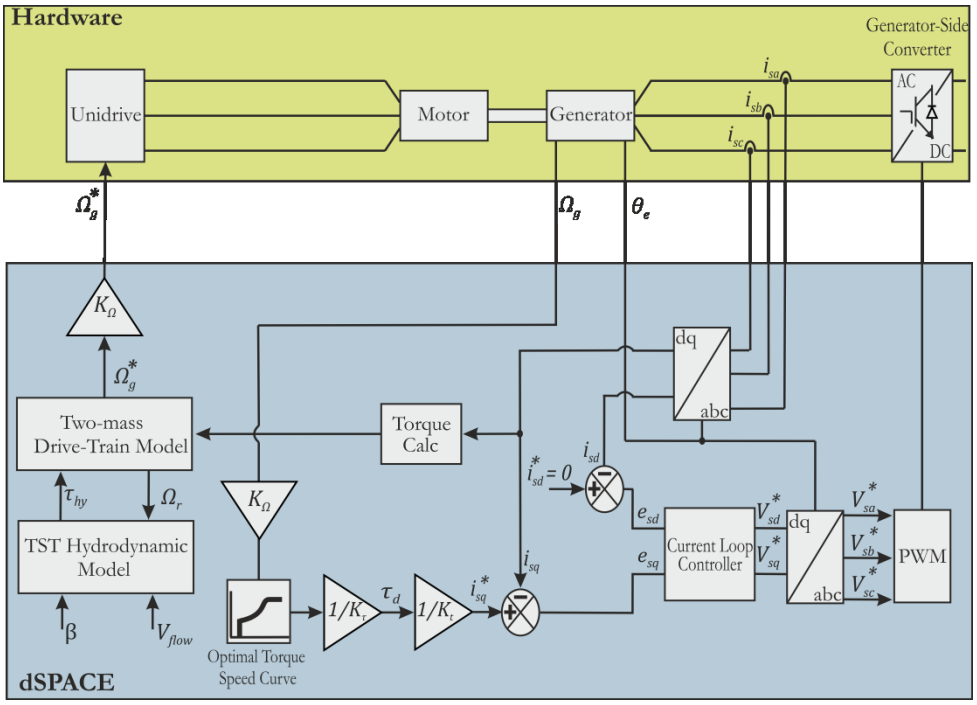

Figure 3.4: Hardware in the loop implementation of generator-side control strategy.

Depending on the flow speed (V_{flow}) being experienced by the TST a speed reference (Ω_g^*) is generated. The generator used in the hardware loop has a higher rated speed and lower rated torque than the 1 MW generator used in simulation. Therefore, to test the 1 MW TST model using the hardware available on the test rig the speed reference (Ω_g^*) was scaled by a factor K_Ω and the torque demand (τ_d) was scaled by a factor K_τ as shown in Figure 3.4. The scaling factors were determined as given in (3.4) and (3.5):

$$K_\Omega = \frac{1800 \text{ rpm}}{13\text{rpm}} = 138.5 \tag{3.4}$$

$$K_\tau = \frac{734753 \text{ Nm}}{3.9 \text{ Nm}} = 188398 \tag{3.5}$$

where K_Ω and K_τ are the scaling factors for the speed and torque. 1800 rpm and 3.9 Nm are the rated speed and torque of the synchronous machine used on the hardware rig. 13 rpm and 734753 Nm are the rated speed and torque of the generator used in simulation. All parameters for the respective machines are in Appendix C.1 and Appendix A.3.

After scaling the speed reference is used by the Unidrive to control the motor, which then drives the generator. The generator speed (Ω_g) and rotor position (θ_e) are measured using an incremental encoder. These variables are then fed back into the dSPACE®. The measured speed is read into a lookup table which outputs a torque demand (τ_d) according to equation (2.8). This ensures that the turbine follows an optimal torque vs. speed curve that maximises the output power. The rotor position is used when converting the three-phase generator currents (i_{sa}, i_{sb}, i_{sc}) to d and q axis currents. The q-axis current is used to calculate the generator reaction torque which is inputted to the two-mass model in order to balance the hydrodynamic torque (τ_{hy}). The d-axis current reference is maintained at zero so the maximum torque to current ratio is obtained.

Generator-Side Controller design – Current Loop

To tune the q-axis current loop for the generator-side converter the same procedure detailed in Section 2.2.2 of Chapter 2 was used. The design criteria are given as follows:

- Closed loop response should have zero steady state error.
- Maximum overshoot of the step response should be limited to less than 5%.
- The bandwidth should be high enough to ensure that decoupling with the mechanical system is achieved.

The transfer functions are as follows:

$$PI_{isq\_gen}(s) = K_p + \frac{K_I}{s} \tag{3.6}$$

$$G_{VSC}(s) = \frac{V_{sq}(s)}{V_{sq}^*(s)} = \frac{1}{0.5\,T_s s + 1} \tag{3.7}$$

$$G_{plant}(s) = \frac{i_{sq}(s)}{V_{sq}(s)} = \frac{1}{L_{sq}s + R_s} \tag{3.8}$$

where T_s is the sampling delay of the PWM converter, R_s is the generator stator resistance and L_{sq} is the generator stator inductance in the q-axis. All parameters are given in Appendix C.1. Through bode shaping a response that meets the criteria, was achieved with a PI controller given as follows:

$$PI_{isq\_gen}(s) = \frac{17.5s + 4500}{s} \tag{3.9}$$

The frequency response curves in Figure 3.5 (a) show the performance of the controller. It can be seen that the performance is similar to that achieved by the controller designed in Chapter 2. The phase margin is 85 degrees, meaning that the overshoot is well within the 5% limit defined in the criteria. This is reflected in the step response of Figure 3.5 (b). The bandwidth is ≈120Hz leading to a settling time of ≈ 8 ms which can be seen in the step response of Figure 3.5 (b).

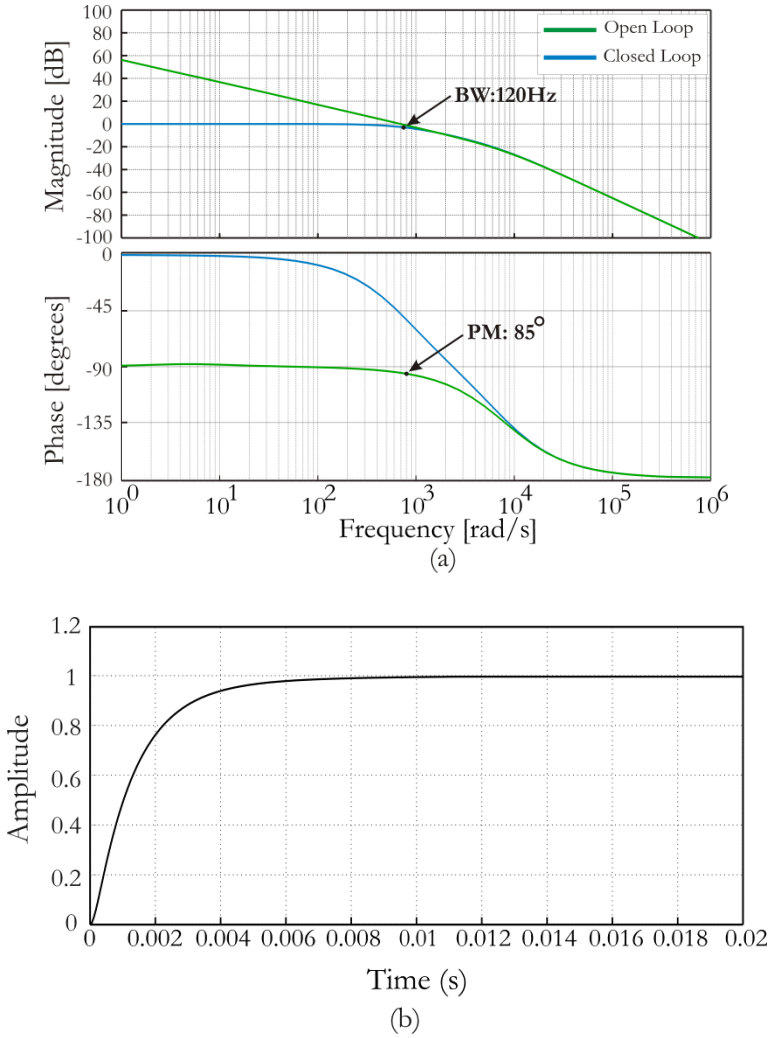

Figure 3.5: (a) Bode plot showing the frequency response of the generator-side *q*-axis current control loop $\left(PI_{isq\_gen}(s) * G_{VSC}(s) * G_{plant}(s)\right)$ in both closed loop and open loop for hardware in the loop experiment. (b) Generator-side current control loop step response.

The same control parameters were used for the d-axis and the q-axis control loops. The control parameters are summarised in Table 3.1.

Controller	K_p	K_I
PI_{isq_gen}	17.5	4500
PI_{isd_gen}	17.5	4500

Table 3-1: PI controller parameters for the generator-side converter of hardware in the loop test rig.

3.2.2 Grid-Side Converter Control

A block diagram showing how the grid-side controller was implemented on the experimental test rig is given in Figure 3.6.

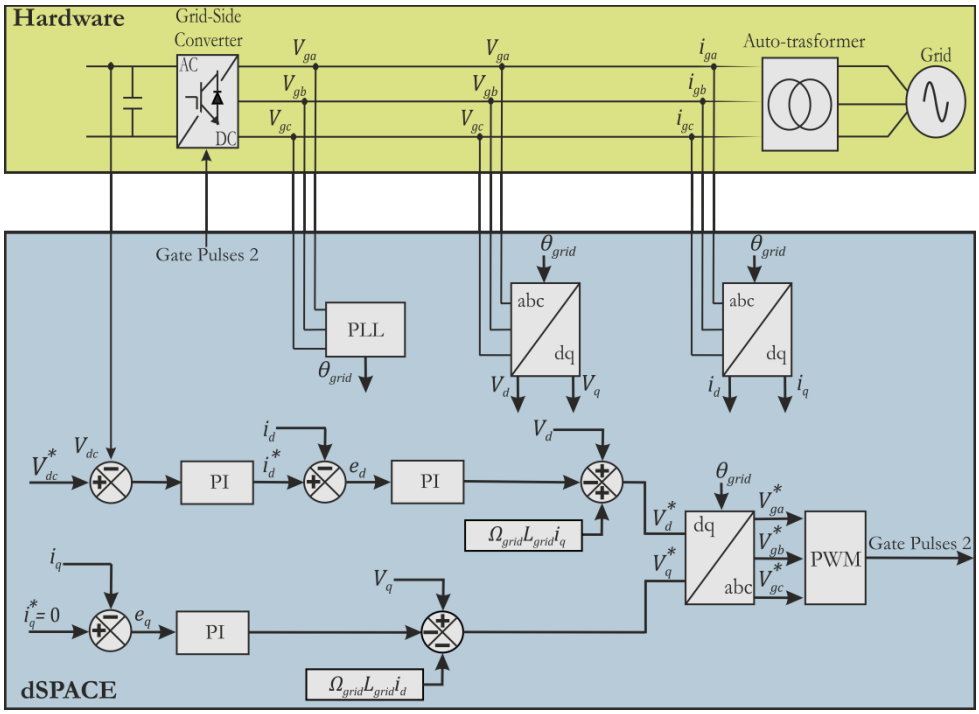

Figure 3.6: Hardware in the loop implementation of grid-side control strategy.

The three-phase currents (i_{ga}, i_{gb}, i_{gc}) are read into to the dSPACE® and used by the controller to generator the error terms e_d and e_q. The three-phase voltages (V_{ga}, V_{gb}, V_{gc}) are also read into the dSPACE® and used to generate the feed-forward voltage terms V_d and V_q. The grid phase angle (θ_{grid}) is used to ensure synchronisation and is obtained using a PLL. The PLL was implemented using a standard block from the SimPowerSystems library in Simulink®. Reference voltages $(V_{ga}^*, V_{gb}^*, V_{gc}^*)$ are used to generate the PWM gate pulses which are sent to the grid-side converter on the hardware rig.

Grid-Side Controller Design – Current Loop

The grid-side controller was designed using the same procedure described in Section 2.2.3 of Chapter 2. The inner current loop was tuned first followed by the outer voltage loop. The bandwidth of the inner current loop was designed to be ≈ 20 times faster than that of the outer voltage loop to ensure that the inner loop was decoupled from the outer loop. The design criteria are summarised as follows:

- Closed loop response should have zero steady state error.
- Maximum overshoot of the step response should be limited to less than 5%.
- The bandwidth should be high enough to ensure that the inner current loop is decoupled from the outer voltage control loop. Thus a minimum bandwidth of ≈ 250 Hz was specified.

The transfer functions of the inner current loop are given as follows:

$$PI_{id\_grid}(s) = K_p + \frac{K_I}{s} \tag{3.10}$$

$$G_{VSC}(s) = \frac{V_d(s)}{V_d^*(s)} = \frac{1}{0.5\,T_s s + 1} \tag{3.11}$$

$$G_{plant}(s) = \frac{i_d(s)}{V_d(s)} = \frac{1}{L_{grid}s + R_{grid}} \tag{3.12}$$

where T_s is the sampling delay of the PWM converter, L_{grid} and R_{grid} are the inductance and resistance between the converter and grid. All parameters are given in Appendix C.1. Through bode shaping a response that meets the criteria, was achieved with a PI control structure given as follows:

$$PI_{id\_grid}(s) = \frac{4.6s + 20}{s} \tag{3.13}$$

The frequency response curves in Figure 3.7 (a) show the performance of the controller. The phase margin is 81 degrees, meaning that the overshoot is well within the 5% limit defined in the criteria. This is reflected in the step response of Figure 3.7 (b). The bandwidth is ≈245Hz leading to a settling time of ≈ 4 ms which can be seen in the step response of Figure 3.7 (b). The same parameters used for the q-axis current loop were used for the d-axis.

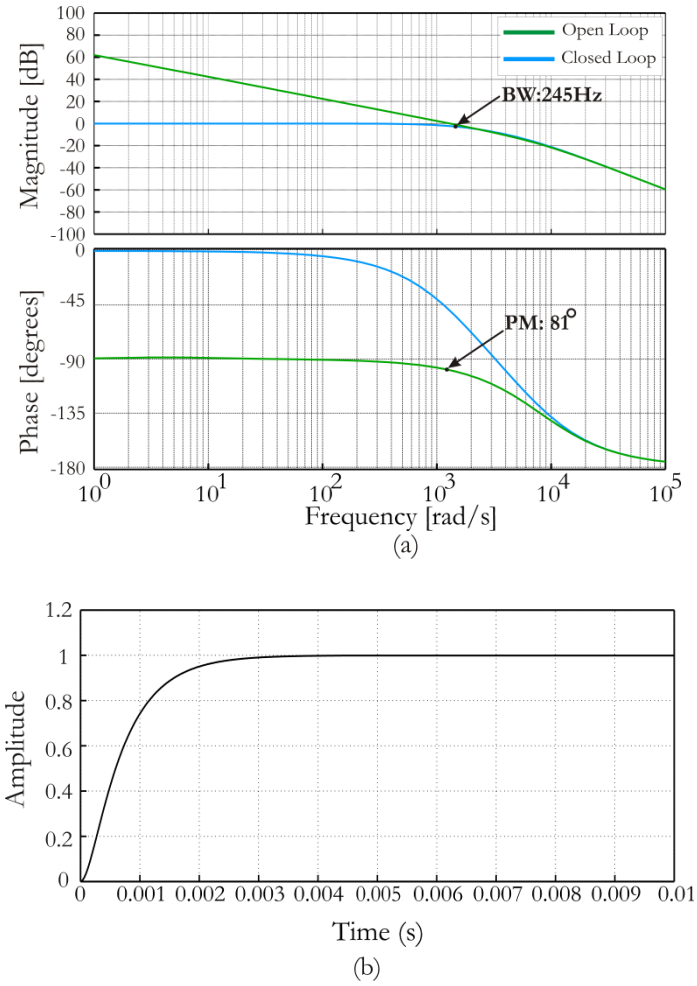

Figure 3.7: (a) Bode plot showing frequency response of the grid-side current control loop $\left(PI_{id\_grid}(s) * G_{VSC}(s) * G_{plant}(s)\right)$ in closed loop and open loop (b) Grid-side current control loop step response.

The outer voltage loop was designed to be 20 times slower than the inner current loop. When tuning the outer loop, the inner loop was approximated as a unity gain as shown in Figure 2.16. The transfer function relating the d-axis current (i_d) to the DC link voltage (V_{DC}) is given as:

$$\frac{V_{dc}(s)}{i_d(s)} = \frac{3}{4} \cdot \frac{M_a}{Cs} \tag{3.14}$$

where C is the DC link capacitance and M_a is the amplitude modulation ratio. Parameters are given in Appendix C.1.

The PI controller $\left(PI_{V_{dc}}(s)\right)$ used in the outer voltage control loop is given as follows:

$$PI_{V_{dc}}(s) = \frac{0.12s + 0.8}{s} \tag{3.15}$$

The frequency response curves of Figure 3.8 (a) show that the controller gives a good response that meets the design criteria. The phase margin is 85 degrees and the overshoot is within the 5% limit. This is reflected in the step response of Figure 3.8b. The system achieves a bandwidth of ≈ 12.25 Hz, which is 20 times slower that of the inner current loop (Figure 3.7 (a)).

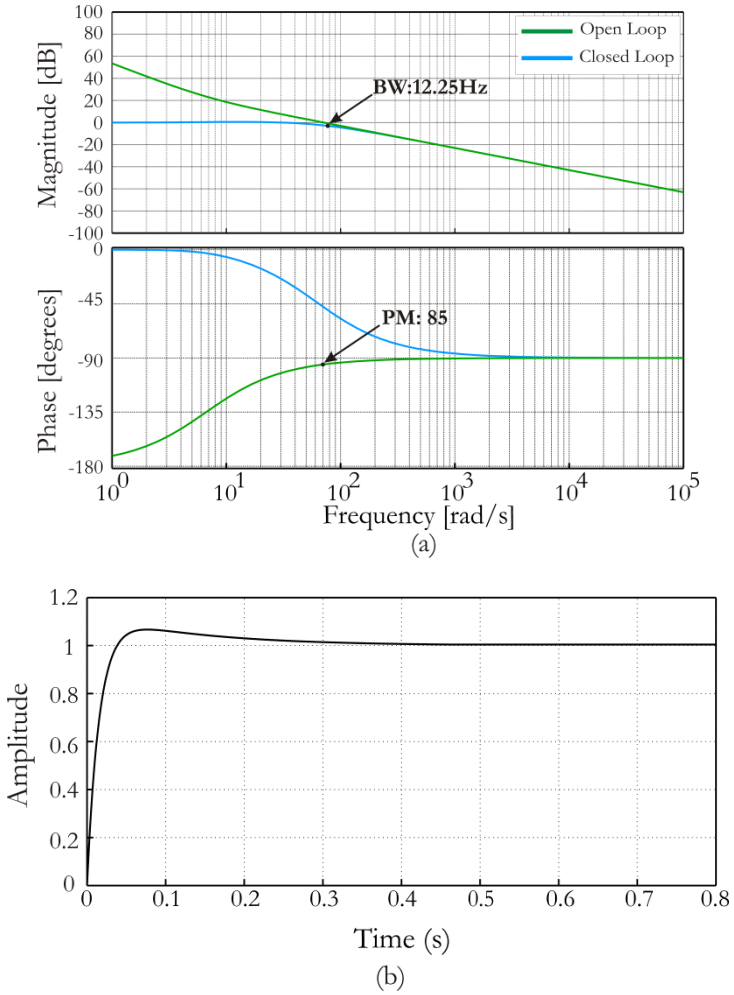

Figure 3.8: (a) Bode plot of the grid-side voltage control loop (b) Voltage control loop step response.

The parameters for the grid-side converter are summarised in Table 3.2.

Controller	K_p	K_I
PI_{id_grid}	4.6	20
PI_{iq_grid}	4.6	20
$PI_{V_{dc}}$	0.12	0.8

Table 3-2: PI controller parameters for the grid-side converter of hardware in the loop test rig

3.3 Experimental Results and Discussion

3.3.1 Experimental Results

To verify the controllers a similar test to that carried out in Section 2.3.2 of Chapter 2 was undertaken. The turbine was assumed to be operating in below rated flow speeds and the pitch angle (β) was set to zero. At the 30 second mark a step change in the flow speed was applied from 1m/s to 2.3m/s as shown in Figure 3.9 (a). The generator speed (Ω_g), which is controlled in accordance with equation 2.8, increases as shown in Figure 3.9 (b).

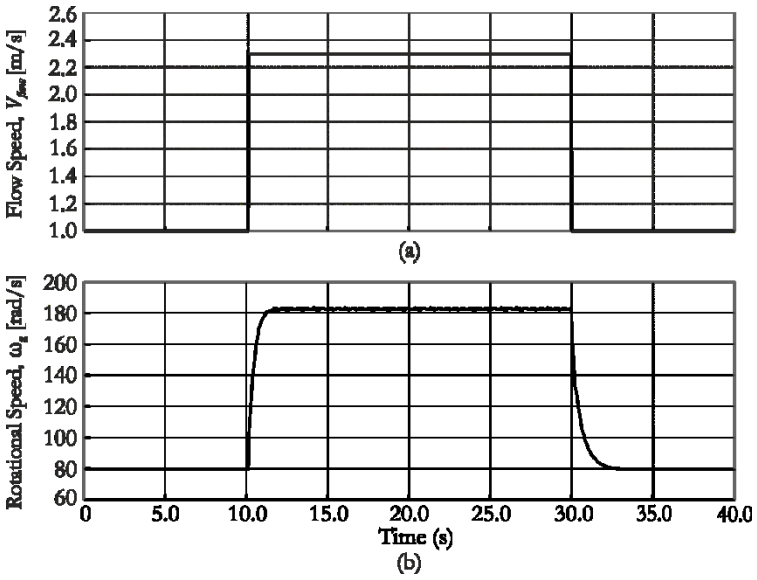

Figure 3.9: (a) Step change in flow speed (V_{flow}). (b) Response of generator rotational speed (Ω_g) to step change in flow speed.

The hydrodynamic torque (τ_{hy}) and the electromagnetic torque (τ_{em}) are given in Figure 3.10. Following the step change in flow speed at the 10 second mark the hydrodynamic torque increases abruptly. However, because the generator speed (Ω_g) is impeded by inertia the electromagnetic torque - which is proportional to the square of the generator speed as given by equation 2.8 – increases more slowly. Eventually the system reaches a new steady state operating point, where the hydrodynamic torque and the generator torque are balanced, at approximately 11 seconds. Figure 3.11 shows the generator phase currents (i_{sa}, i_{sb}, i_{sc}). As expected the value of the currents increases from approximately 0.3 Amps to 2.2 Amps following the step change in flow speed.

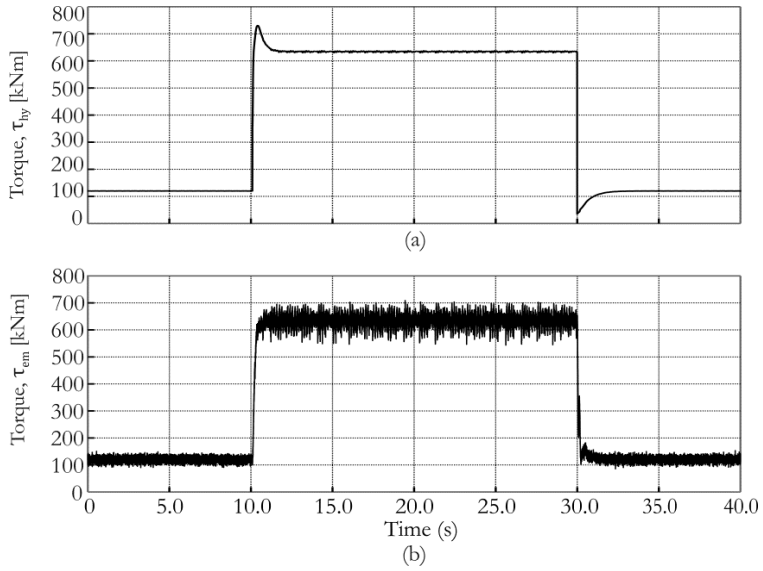

Figure 3.10: (a) Response of hydrodynamic torque (τ_{hy}) to a step change in flow speed (V_{flow}). (b) Response of generator torque (τ_{em}) to step change in flow speed.

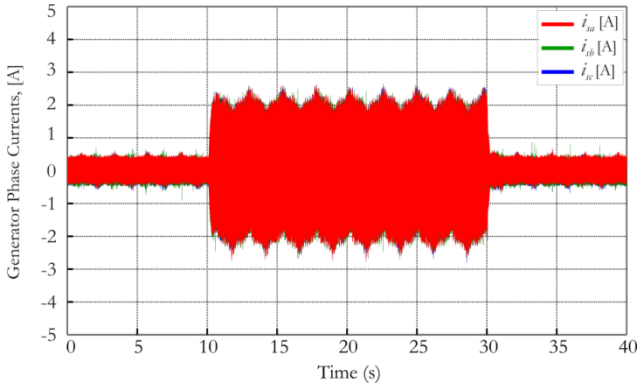

Figure 3.11: Generator phase currents (i_{sa}, i_{sb}, i_{sc}).

The DC link voltage is shown in Figure 3.12. The controller regulates the DC link voltage at 400V. Two transient peaks at the 10 second and 40 second marks are visible and correspond to the increase and decrease in current coming from the generator at those times. With the exception of the transient peaks the ripple remains within 1% for the duration of the simulation.

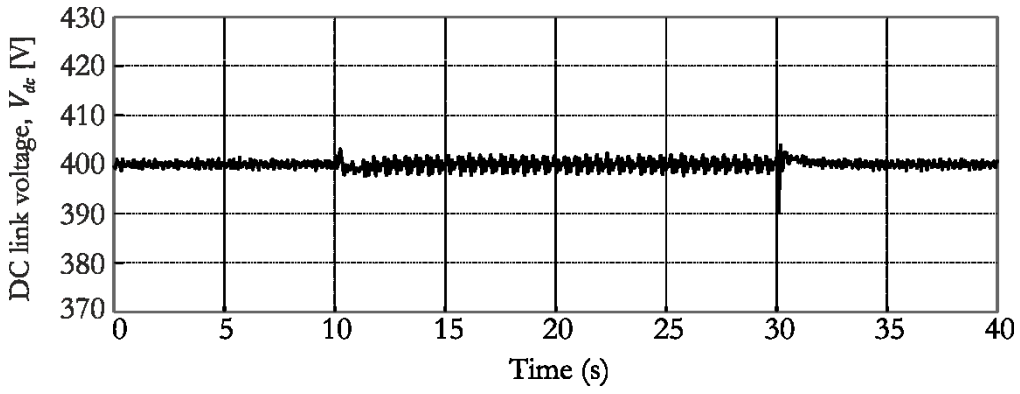

Figure 3.12: DC link voltage (V_{dc}).

Figures 3.13 (a) and (b) show the d-axis and q-axis currents of the generator. The d-axis current (i_{sd}) reference is set to zero in order to operate the generator at the maximum torque/ampere ratio. The q-axis current (i_{sq}) is directly proportional to the electromagnetic torque, and as a result it can be seen to increase at the 10 second mark as the generator torque demand increases.

Figures 3.13 (c) and (d) show the d-axis and q-axis currents on the grid-side. The aim was to transfer all the active power from the turbine to the grid; therefore, the q-axis current reference was set to zero. The active power is controlled via the d-axis current which increases at the 10 second mark, following the increase in power coming from the turbine. Figure 3.14 shows the active and reactive power transferred to the grid. It can be seen that the active power increases at the 10 second mark whereas the reactive power remains the same.

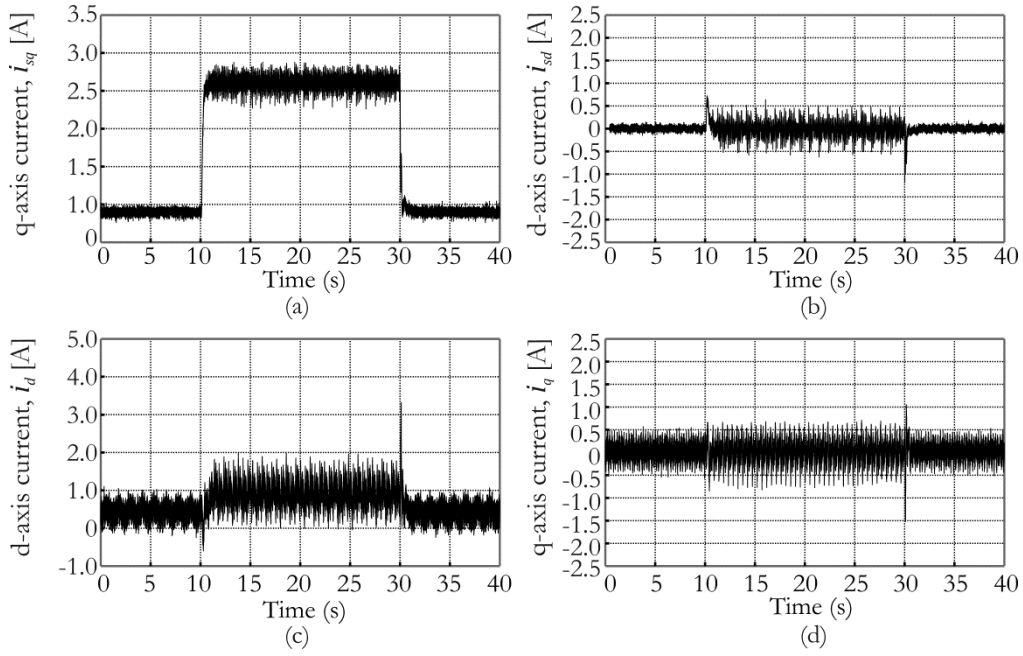

Figure 3.13: (a) q-axis current for generator-side converter. (b) d-axis current for generator-side converter. (c) d-axis current for grid-side converter. (d) q-axis current for grid-side converter.

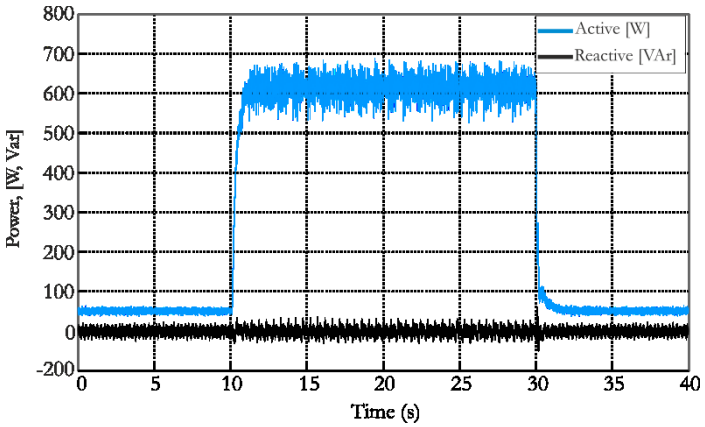

Figure 3.14: Active and reactive power

3.3.2 Discussion

The control schemes developed in Chapter 2 have been implemented on a hardware in the loop test rig. The PI controllers of both the grid-side and generator-side control strategies were re-tuned since the parameters of the test rig differed from those used in simulation. As was the case in simulation the control scheme was able to maximise the power output of the TST during below rated operation. When subjected to a step change in flow speed the controller varied the rotor speed using the generator reaction torque, thus causing the turbine to track an optimum torque vs. speed trajectory that maximises the output power.

Once again the grid-side converter was used to regulate the DC link voltage. The regulation achieved by the controller was satisfactory; however, transient spikes in the voltage and changes in the ripple were observed when the turbine was subjected to a step change in flow speed. These can be seen in Figure 3.12. The regulation could be improved by altering the control parameters slightly; however, an optimal control design was not the aim of this work. The reason the performance of the controller is not quite as predicted by the frequency response analyses is likely due to the parameters on the hardware rig differing from those used to design the controller. Obtaining values for the parameters with absolute precision is difficult and there is likely to be some variation. Furthermore, the mathematical model used to design the controller is only a simplified model that does not take into account all the dynamics of the real system. Therefore, one would expect there to be some difference between the predicted performance and that achieved in the experiment.

Chapter 4

4. Design and Control of Pitch and Stall Regulated Tidal Stream Turbine Rotors

Summary:

Two control strategies for regulating the power and speed of a horizontal axial flow TST are proposed in this section. The first strategy involves pitching the turbine blades to regulate the speed and power output of the rotor while the second strategy relies on the stall characteristic of the turbine blade. Momentum theory and blade element theory are introduced. From these theories, governing equations are derived and used to design two dynamic TST rotor models. One of the models has fixed pitch rotor blades while the other model has variable pitch blades. The performance of each model is then verified using the blade element momentum (BEM) code GH Tidal Bladed® (Bossanyi, 2009). Following verification of the models the objective is to use the dynamic models to test and compare the performance of the respective control strategies in terms of performance under turbulent flows, loading and energy yield.

4.1 Hydrodynamics of Axial Flow Tidal Stream Turbines

4.1.1 Actuator Disk Theory and the Betz Limit

The actuator disk theory is used to describe how a turbine rotor extracts energy from the flow. This theory assumes an idealised model of the turbine rotor, which is described as an actuator disk. A stream tube is placed around the disk forming the boundaries of the control volume, which are the surface of the stream tube and the two cross sections of the stream tube (Figure 4.1). The control volume is divided into four stations. Station 0 is far upstream, station 1 is just before the actuator disk, station 2 is just after the actuator disk and station 3 is far downstream. The assumptions on which the actuator disk theories are based are well documented (Manwell, McGowan & Rogers, 2002). Among these assumptions are the following: all flow into and out of the actuator disk is axial, the flow is incompressible and the static pressures (p) far upstream and far downstream of the actuator disk are both equal to the ambient static pressure.

As the flow field moves through the actuator disk kinetic energy is extracted, and as a result the velocity (V) of the flow is reduced downstream of the disk. Conservation of mass means that the diameter of the flow field must increase as the velocity decreases; hence, the cross-sectional area (A) of the stream tube is smaller upstream of the actuator disk than it is downstream. As the mass flow rate remains the same everywhere along the stream tube the following is true:

$$\rho A_0 V_0 = \rho A_{DISK} V_{DISK} = \rho A_3 V_3 \tag{4.1}$$

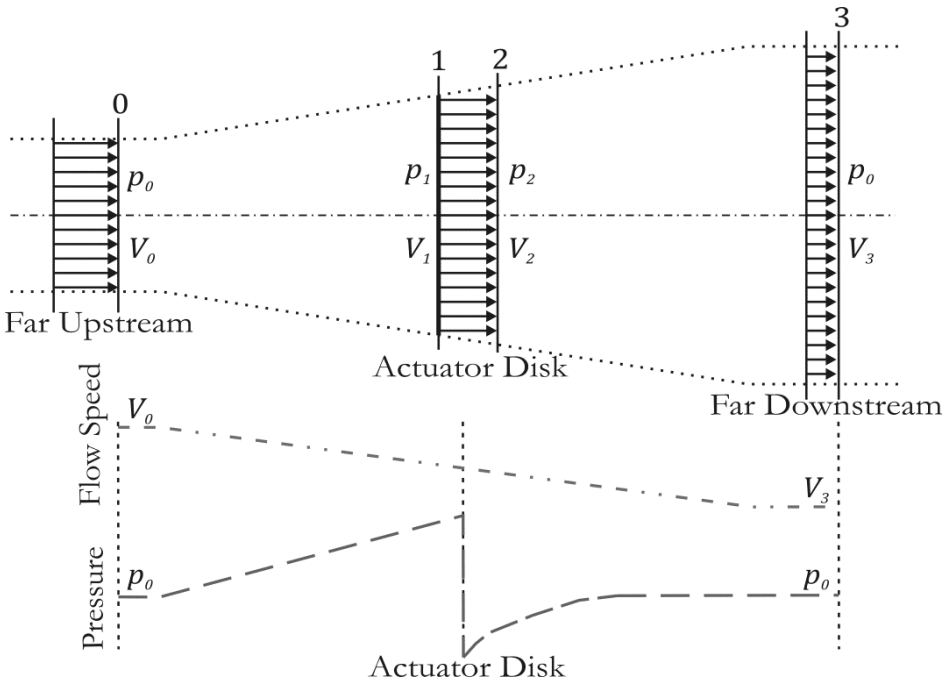

Figure 4.1: Actuator disk with stream tube. V = flow velocity, p = pressure: 0,1,2,3 indicate locations.

Stations 1 and 2 on the stream tube are considered to be infinitely close to each other. So the velocity of the flow passing through the actuator disk (V_{Disk}) is constant.

$$V_1 = V_2 = V_{Disk} \tag{4.2}$$

However, Figure 4.1 shows that there is an overall reduction in the flow velocity along the length of the stream tube. Therefore, because momentum is conserved the actuator disk must exert a thrust force (T) that is equal to the rate of change of momentum (Burton, et al., 2001):

$$\text{Rate of change of momentum} = \rho A_{Disk} V_{Disk} (V_0 - V_3) \tag{4.3}$$

So the thrust force that the actuator disk exerts on the flow is given as follows:

$$T = \rho A_{Disk} V_{Disk} (V_0 - V_3) \tag{4.4}$$

Applying the Bernoulli equations between station 0 and 1, then 2 and 3, it can be shown that the thrust force exerted by the actuator disk is proportional to the pressure difference across it.

$$p_0 + \frac{1}{2}\rho V_0^2 = p_1 + \frac{1}{2}\rho V_{Disk}^2 \tag{4.5}$$

$$p_2 + \frac{1}{2}\rho V_{Disk}^2 = p_0 + \frac{1}{2}\rho V_3^2 \tag{4.6}$$

Using Equation (4.5) and (4.6) gives the pressure drop across the actuator disk as:

$$p_1 - p_2 = \frac{1}{2}\rho(V_0^2 - V_3^2) \tag{4.7}$$

It follows that the thrust on the actuator disk can be expressed as:

$$T = A_{Disk}(p_1 - p_2) \tag{4.8}$$

Substituting Equation (4.7) into (4.8) gives:

$$T = \frac{1}{2} A_{Disk}\rho(V_0^2 - V_3^2) \tag{4.9}$$

Using equations (4.4) and (4.9) the velocity at the actuator disk, V_{Disk} can be expressed as:

$$V_{Disk} = \frac{V_0 + V_3}{2} \tag{4.10}$$

Equation (4.10) shows that the velocity at the actuator disk is the average of the velocity far upstream and far downstream of the disk. The fractional reduction in velocity, from that far upstream of the actuator disk to that at the actuator disk is called the axial induction factor (a) and is defined as (Manwell, McGowan & Rogers, 2002):

$$a = \frac{V_0 - V_{Disk}}{V_0} \tag{4.11}$$

Using equations (4.10) and (4.11) expressions for the flow velocity at the actuator disk and far downstream of the actuator disk can be obtained in terms of the axial induction factor.

$$V_{Disk} = V_0(1 - a) \tag{4.12}$$

$$V_3 = V_0(1 - 2a) \tag{4.13}$$

For a turbine with zero loading, the flow velocity at the rotor (V_{Disk}) is equal to the undisturbed velocity upstream of the disk (V_0), while an operating and hence loaded turbine slows down the flow velocity to a lower value. It can be seen from equation (4.13) that momentum theory only applies up to $a = 0.5$. For axial induction factors greater than 0.5 V_3 starts to become negative and the relationship breaks down.

Having derived equations for the thrust force on the actuator disk and the flow velocity at the actuator disk it is possible to express the power extracted as:

$$P = TV_{Disk} \tag{4.14}$$

By substituting equation (4.9) into (4.14) the power can be given as:

$$P = \frac{1}{2}A_{Disk}\rho(V_0^2 - V_3^2)V_{Disk} \tag{4.15}$$

And by substituting for V_3 and V_{Disk} from equations (4.12) and (4.13) the power can be expressed in terms of the axial induction factor (a) as:

$$P = \frac{1}{2} A_{Disk} \rho 4a(1-a)^2 V_0^3 \tag{4.16}$$

Rotor efficiency is expressed in terms of the power coefficient (C_P), which is a ratio between the power in the flow and that extracted by the rotor. Using equation (4.16) C_P becomes:

$$C_P = \frac{Rotor\ power}{Power\ in\ flow} = \frac{P}{\frac{1}{2}\rho A_{Disk} V_0^3} \quad \therefore \quad C_P = 4a(1-a)^2 \tag{4.17}$$

From equations (4.9), (4.12) and (4.13) the axial thrust on the disk can be written given as:

$$T = \frac{1}{2} \rho A_{Disk} V_0^2 [4a(1-a)] \tag{4.18}$$

Finally by using equation (4.18) the thrust coefficient (C_T) can be given as:

$$C_T = \frac{T}{\frac{1}{2}\rho A_{Disk} V_0^2} \quad \therefore \quad C_T = 4a(1-a) \tag{4.19}$$

Using the actuator disk model, equations for power and thrust as a function of axial induction factor have been obtained. It is clear from equation (4.16) that the power a TST is able to extract from the flow is proportional to the cube of the flow velocity far upstream of the rotor, and the axial induction factor. The thrust coefficient (C_T) and power coefficient (C_P) have also been derived. These coefficients are plotted against axial induction factor in Figure 4.2.

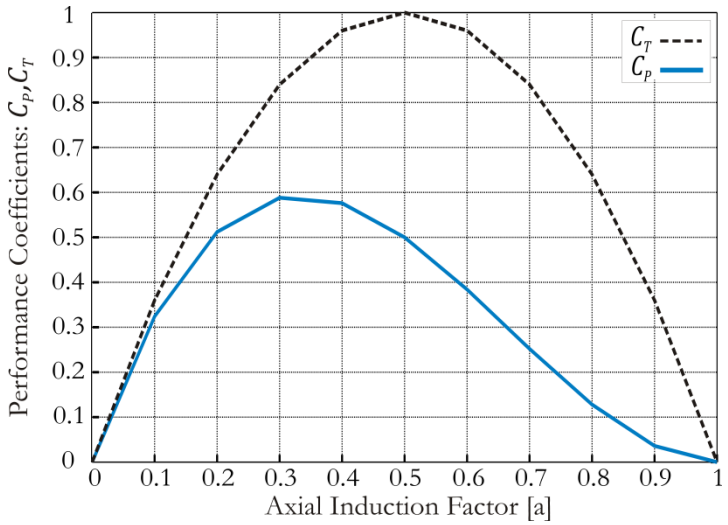

Figure 4.2: Power (C_P) and Thrust Coefficients (C_T) versus Axial Induction Factor

Differentiating the expression for (C_p) and setting it equal to zero gives the maximum as 0.593 (the Betz limit), which occurs at $a = \frac{1}{3}$. This shows that for an ideal rotor the flow speed at the rotor should be $\frac{2}{3}$ of the velocity far upstream for the rotor to operate with maximum efficiency. At the maximum power point $\left(a = \frac{1}{3}\right)$ C_T has a value of $\frac{8}{9}$. The Betz limit imposes a limit on the amount of energy a turbine can extract from the flow regardless of design (Schubel, Crossley, 2012). The existence of this physical limit is intuitive when one considers that the energy extracted is directly proportional to the reduction in flow speed over the turbine, as per equation (4.15). From this equation 100% energy extraction would imply a flow velocity downstream of the turbine of zero $(V_3 = 0)$. This is not possible and would violate the continuity equation (4.1).

It is common to express the power and thrust produced by the turbine in terms of the performance coefficients (C_P) and (C_T); therefore, by using equations (4.17) and (4.19) we can write equations (4.16) and (4.18) as follows:

$$P = \frac{1}{2} A_{DISK} \rho V_0^3 C_P \tag{4.20}$$

$$T = \frac{1}{2} A_{DISK} \rho V_0^2 C_T \tag{4.21}$$

4.1.2 Angular Momentum Theory and Wake Rotation

The actuator disk theory used to derive the Betz limit assumes that the flow beyond the rotor is axial and does not take into account the rotation in the wake of the turbine rotor. The actuator disk model used by Betz describes a turbine where kinetic energy is extracted from the flow resulting in a reduction in the flow velocity downstream of the rotor. On a real turbine energy is extracted through torque. As the flow passes through the rotor it will exert a force on the blades that is tangential to the plane of rotation *i.e.* in the direction of the blades rotation. Due to the conservation of angular momentum, if the flow is exerting a torque on the rotor then the rotor must be exerting a torque on the flow that is equal in magnitude and opposite in direction. Therefore, the torque that the rotor exerts on the flow will cause it to rotate in the opposite direction to the rotation of the rotor as shown in Figure 4.3. Rotational energy in the wake is considered a loss as it does not increase the pressure drop across the rotor; therefore, it does not increase the power extracted. It reduces the rotor efficiency to less than that predicted by Betz.

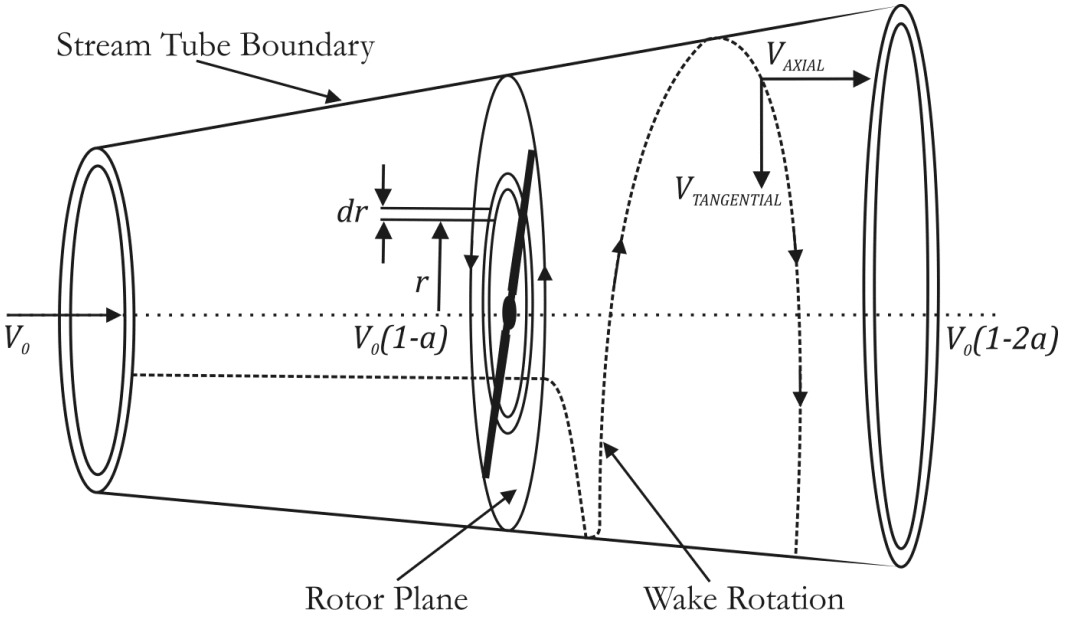

Figure 4.3: Stream tube model illustrating the rotation of wake.

Taking a small annular element of the rotor as shown in Figure 4.3, that is a distance r from the centre of rotation and dr thick it is possible by considering the conservation of angular momentum, to calculate the torque exerted by the rotor on this annular element of fluid. The equation is given as follows (Manwell, McGowan & Rogers, 2002):

$$d\tau = \rho\omega r^2 V_{DISK} 2\pi r dr \tag{4.22}$$

where $2\pi r dr$ is the cross sectional area of the annular tube shown in Figure 4.3 and ω is the rotational velocity induced in the wake by the rotor. It is possible to define the angular induction factor as (Manwell, McGowan & Rogers, 2002):

$$a' = \frac{\omega}{2\Omega_r} \tag{4.23}$$

where Ω_r is the rotational velocity of the rotor. By substituting for ω and V_{Disk} in equation (4.22) from equations (4.23) and (4.12) the torque can be expressed in terms of the axial and angular induction factors as follows:

$$d\tau = 4a'(1-a)\frac{1}{2}\rho V_0 \Omega_r r^2 2\pi r dr \tag{4.24}$$

The power output from the rotor is:

$$P = \int \Omega_r d\tau \tag{4.25}$$

By substituting for $d\tau$ with equation (4.24) it is possible to express the power produced by the rotor as follows:

$$P = \frac{1}{2}\rho A V_0^3 \frac{8}{\lambda^2} \int a'(1-a)\lambda_r^3 d\lambda_r \tag{4.26}$$

It is clear from equation (4.26) that the power extracted by the rotor is a function of both the axial and the rotating motion of the flow stream, which is in contrast to the simple momentum theory of Betz where the power is purely a function of the axial flow speed. It can also be seen that when angular momentum is considered the power also becomes a function of λ_r, which is defined as the local TSR. The TSR is the ratio between the tangential velocity of the rotor blades and the undisturbed axial flow. When referenced to the tangential velocity at the rotor blade tip it is given as in equation (1.5). When referenced to some intermediate radius along the blade, as in equation (4.26), it is given as follows:

$$\lambda_r = \frac{\Omega_{r\_sec}}{V_0} = \frac{r\lambda}{R} \tag{4.27}$$

where Ω_{r_sec} is the blade section velocity at some intermediate radius along the blade, λ is the TSR referenced to the rotor blade tip and R is the rotor blade radius. Using equation (4.26) the C_P value is:

$$C_P = \frac{P}{\frac{1}{2}\rho A_{DISK} V_0^3} \quad \therefore \; C_P = \frac{8}{\lambda^2} \int a'(1-a)\lambda_r^3 d\,\lambda_r \tag{4.28}$$

By taking into account the rotation in the wake the C_P value becomes a function of the TSR and exhibits a maximum value at a particular TSR as shown by equation (4.28).

4.1.3 Blade Element Theory

During operation a TST rotor is exposed to a complex three dimensional flow field that varies spatially and temporally over its swept area. Power production depends on the interaction between the rotor and the flow. It is the hydrodynamic forces generated as the flow passes through the rotor which determine the performance and loads of the turbine.

Blade element theory (BET) provides a way to relate the physical geometry of a rotor blade to its hydrodynamic performance. Momentum theory alone does not provide the necessary information to design a rotor blade. By applying the theories for the momentum of the axial flow and of the radial flow components to a rotor blade with a specific geometry it is possible to obtain the hydrodynamic forces acting in both the axial and tangential directions over the entire length of the blade. BET assumes that the blade is divided up into a finite number of sections (or elements) each of which is a distance r from the centre of rotation and dr thick, as shown in Figure 4.4.

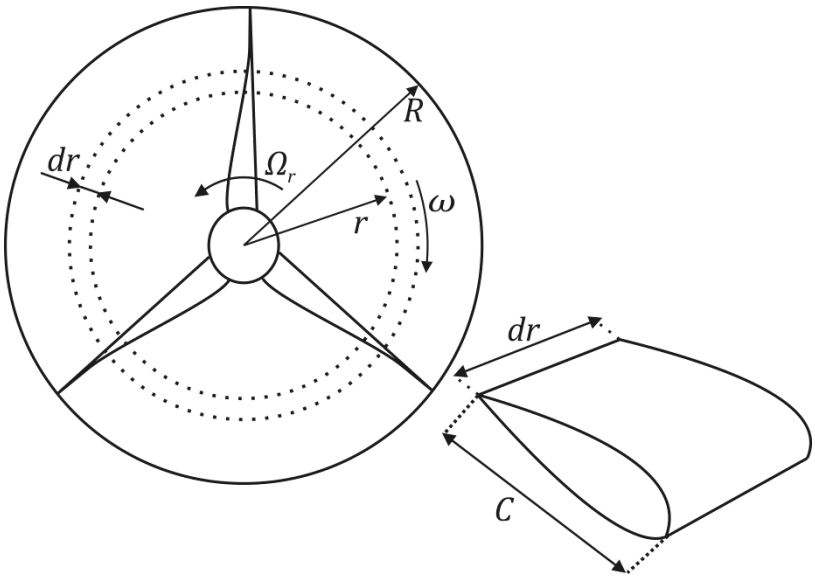

Figure 4.4: Blade Section.

Each element operates hydrodynamically as a two dimensional aerofoil whose hydrodynamic forces can be calculated based on the local flow conditions. By calculating the hydrodynamic forces acting on each element and then integrating along the blade span the total loading, in both the axial and tangential directions can be determined for each blade (Hau, 2006). The total force in the axial direction gives the thrust experienced by the rotor, while the total force in the tangential direction provides the driving torque which used in conjunction with the angular velocity of the rotor (Ω_r) provides the power.

The forces produced by fluid moving over an element of the rotor blade, which is at a radius (r) from the centre of rotation, are shown in Figure 4.5. The aerofoil cross-section at radius r operates at an angle θ_P with respect to the plane of rotation. The flow velocity far upstream of the rotor is V_0 and the axial velocity at the rotor disk is $V_0(1-a)$. The relative flow velocity tangential to the blade element is $\Omega r(1+a')$ (Manwell, McGowan & Rogers, 2002). The axial and tangential velocities combine to form the relative flow velocity (V_{Rel}) at which the flow strikes the blade, which is at an angle of attack (α) to the aerofoil chord line. The relative flow forms an angle (φ) relative to the plane of rotation and an angle (γ) relative to the axis of rotation.

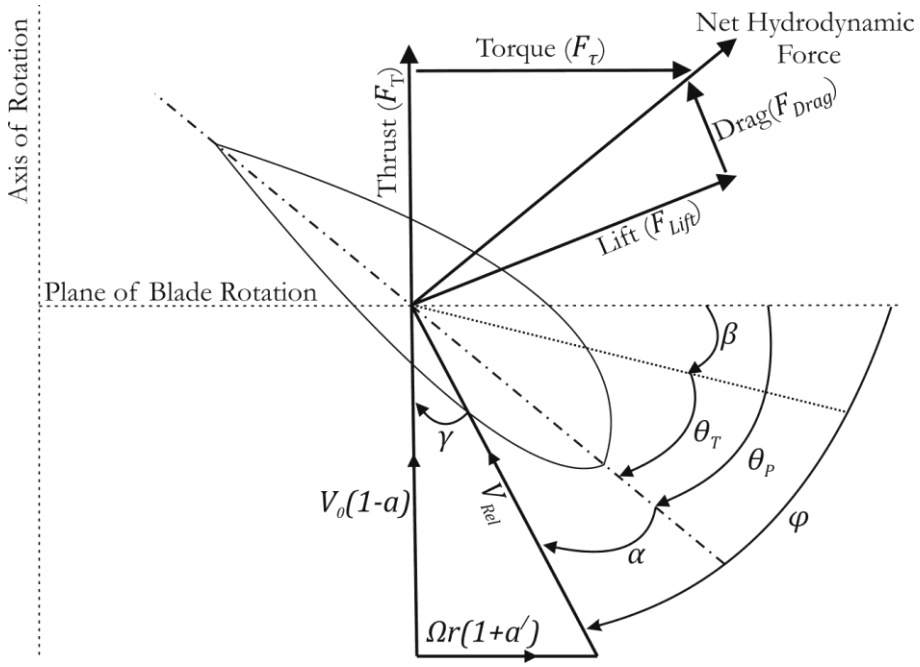

Figure 4.5: Velocities, forces and angles on a blade element.

- β= Blade pitch angle.
- θ_T= Section twist angle.
- θ_P= Section pitch angle.
- α= Angle of attack.
- φ = Angle of relative flow to rotor plane.
- $\gamma_=$ Angle of relative flow to rotor axis.

The motion of the fluid around the aerofoil generates a lift force (F_{Lift}) which acts perpendicular to the relative flow and a drag force (F_{Drag}) which acts parallel to the relative flow. The lift and drag forces acting on the blade element of Figure 4.5 can be expressed as follows:

$$F_{Lift} = C_l(\alpha)\frac{1}{2}\rho {V_{Rel}}^2 C d_r \tag{4.29}$$

$$F_{Drag} = C_d(\alpha)\frac{1}{2}\rho {V_{Rel}}^2 C d_r \tag{4.30}$$

Where C_l and C_d are the coefficients of lift and drag. C is the length of the aerofoil chord line. The coefficients of lift and drag are both a function of the angle of attack (α). As observed in Figure 4.5 the angle of attack is equal to:

$$\alpha = \varphi - \theta_p \tag{4.31}$$

Considering the geometry of Figure 4.5 it is also possible to derive expressions for the thrust (F_T) and driving torque (F_τ) experienced by the blade element operating at a distance r from the centre of rotation. They are given as follows:

$$F_T = F_{Lift}\mathrm{Cos}\varphi + F_{Drag}\mathrm{Sin}\varphi \tag{4.32}$$

$$F_\tau = (F_{Lift}\mathrm{Sin}\varphi - F_{Drag}\mathrm{Cos}\varphi)r \tag{4.33}$$

Substituting for F_{Lift} and F_{Drag} from equations (4.29) and (4.30), equations (4.32) and (4.33) are given as:

$$F_T = \frac{1}{2}\rho V_{Rel}^2 (C_l(\varphi - \theta_P)\mathrm{Cos}\varphi + C_d(\varphi - \theta_P)\mathrm{Sin}\varphi) C d_r \tag{4.34}$$

$$F_\tau = \frac{1}{2}\rho V_{Rel}^2 (C_l(\varphi - \theta_P)\mathrm{Sin}\varphi - C_d(\varphi - \theta_P)\mathrm{Cos}\varphi) C r d_r \tag{4.35}$$

It can be seen that both the lift and drag forces contribute to axial thrust loading. However, the drag also acts to reduce the driving torque, and therefore the power output. So it is desirable to choose aerofoil sections that produce a high C_l/C_d ratio to ensure good conversion efficiency.

In summary the simple momentum theory of Betz provides a C_P of 0.593, showing that just over half the available energy in the flow stream can be extracted. Taking into consideration the wake rotation reduces the amount of energy available for extraction further and means that the C_P value becomes a function of TSR as well as θ_P, which is controllable in the case of variable pitch rotors. At high TSRs C_P will approach the Betz limit because for a given power level a higher

rotational speed implies less torque. Less torque means the wake rotation is reduced; thus, increasing the amount of kinetic energy available for extraction. Relating the momentum theory to the geometry of the blade allows the hydrodynamic forces to be derived, showing that C_P is reduced even further by the effects of hydrodynamic drag. Furthermore, the C_P will have a maximum value at a particular TSR. This has implications on turbine control, particularly in below rated flow speeds where the objective is to operate the rotor at maximum efficiency.

4.2 Above Rated Control Objectives and Strategies

4.2.1 Control Development Process

Development of a control system can be broken into a number of steps. The first step is to identify the control objectives. The second step is to develop a control strategy, which will define the operating point of the turbine for each flow speed. The third step involves developing a dynamic model for which the controller will be designed. The fourth step is defining how the control strategy will be realised. This step mainly involves identifying what the controlled variables are, what the reference signals are, how these signals will be obtained and what control structure will be used. The penultimate step, prior to implementation, is to examine the dynamics of the plant between the input and output of the system and test the closed loop performance of the controller. This section looks at the first three steps identified above, whereas the last two steps are addressed in chapter 5.

4.2.2 Control Objectives

At any tidal site there is likely to be a variation in the flow speed, with the maximum speeds occurring infrequently. TST's will be subjected to the effects of turbulence and surface waves which will cause further variations in the flow (Milne, et al., 2010). This means that TST's will need to be regulated, with a means of limiting output power and shedding mechanical load in high flow speeds (Fraenkel, 2010b). Designing a turbine capable of operating at the maximum flow speed seen at a site will not be economic and it will operate at less than 100% capacity for much of the time. Above rated flow speed, there is enough power in the flow for the turbine to be able to extract its rated power output. The objective of a power regulation strategy is to find a way to lower the operating power coefficient such that the correct power is generated as the flow speed increases. The flow speed at which the turbine produces its peak output power is referred to as the rated power. Above the rated value the objective is to shed the excess power and keep the turbine operating within the specified limits.

4.2.3 Power Regulation Philosophies

The operation and control of horizontal axial flow wind turbines in high wind speeds has been reported comprehensively in the literature (Bianchi, De Battista & Mantz, 2010), and can equally be applied for TSTs. Existing and proposed TST designs use either fixed pitch or variable pitch blades. Most fixed pitch designs rely on the stall characteristic of the rotor blades to regulate the output power. These turbines are designed so that as rated power is reached the rotor speed is either held constant, or reduced as the flow speed continues to increase. Since the pitch angle is also constant this has the effect of increasing the angle of attack (α). Once the angle of attack reaches a critical point the C_l/C_d ratio drops abruptly and the blade will begin to stall, which reduces the hydrodynamic efficiency of the rotor and limits the output power. Figure 4.6 shows the forces acting on a blade element before (green) and after (red) the occurrence of stall.

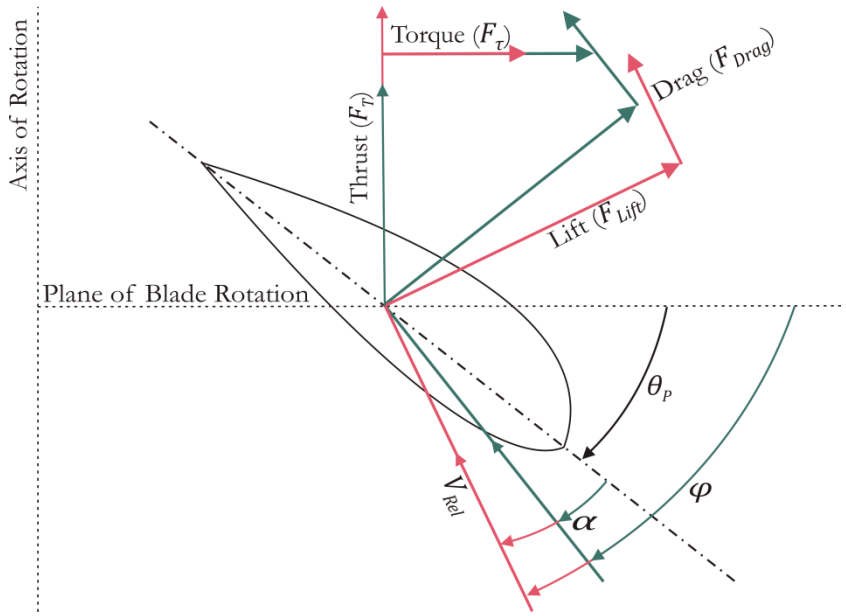

Figure 4.6: Forces on a blade element before (Green) and after (Red) the occurrence of stall.

Figure 4.6 shows that as the turbine goes into stall the driving torque (F_τ) is reduced, whereas the thrust force (F_T) increases significantly leading to higher loading on the rotor and support structure.

Variable pitch turbines can vary the pitch angle of the blades, either independently or collectively, to regulate output power. The blades can be pitched so that the angle of attack increases to actively induce stall above rated flow speed or the blades can be pitched to feather as flow speed increases. Figure 4.7 shows how the forces acting on a blade element change when the blade is pitched to feather following an increase in axial flow speed. The blade element in black experiences a flow speed V_n and forms an angle θ_P with respect to the plane of rotation.

The blade element in red experiences a flow speed V_{n+1} and forms an angle θ_{P+1} with respect to the plane of rotation. As the axial flow speed increases from V_n to V_{n+1} the relative flow angle φ will increase as the relative flow (V_{Rel}) rotates towards the rotor axis. If the blade was fixed pitch this would result in the angle of attack α increasing; however, in this case when the flow speed increases the pitch angle θ_P is increased, which reduces the angle of attack α. This causes the lift coefficient (C_l) to drop, reducing the efficiency of the rotor. From Figure 4.7 the thrust force (F_T) reduces at high flow speeds and the driving torque (F_τ) remains constant. This is in contrast to the stall regulated turbine where thrust increases and driving torque reduces at higher flow speeds.

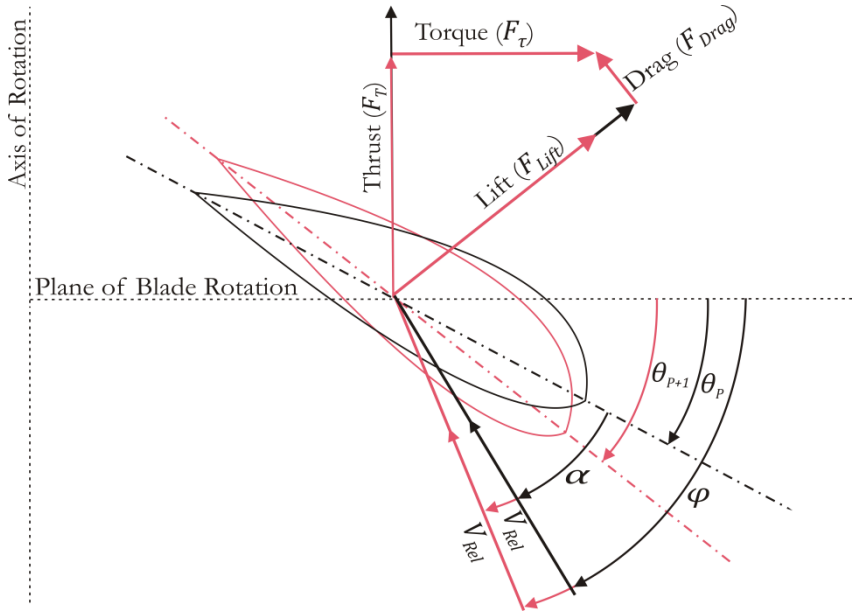

Figure 4.7: Pitching to feather forces on a blade element (Black: Blade is at fine pitch (θ_P) and flow is (V_n); Red: Pitch angle is increased to (θ_{P+1}) and flow is (V_{n+1}) .

In this section two regulation methods are introduced. The first assumes the use of a variable speed stall regulated turbine that has fixed pitch blades and the second assumes the use of a variable speed pitch regulated turbine where the blades can be pitched to feather.

4.2.4 Power Regulation by Pitching to Feather

This control strategy is shown in Figure 4.8. In low flows the rotor speed is regulated at Ω_{r_min}. Below rated speed (between A and G) the turbine is operated in variable-speed mode so that the optimum TSR is maintained, causing the turbine to follow the C_{P_Max} locus. This is achieved by controlling the rotor speed through the generator reaction torque as described in Section 2.1.2 of Chapter 2. The Generator torque demand (τ_d) is set according to equation (2.8) and the turbine is made to follow an optimal torque vs. speed trajectory.

At point G the rotational speed reaches the upper limit (Ω_{r_max}) and is therefore regulated at this point. The turbine will then operate along the segment GH as the flow speed increases from V_{n-1} to V_n. At point H, the turbine reaches rated power and the generator torque is held at a constant (τ_n). Under this condition, further increase in flow speed will increase the hydrodynamic torque, resulting in fluctuation of rotational speed which causes the output power to vary. To avoid this and to keep the turbine operating at H the rotor blades must be pitched. This regulates the rotor hydrodynamic torque; thus, regulating rotor and generator speed and producing constant power. In the case where the rotor speed limit is not reached until V_n the torque speed trajectory can reduce to AH_2 as opposed to AGH.

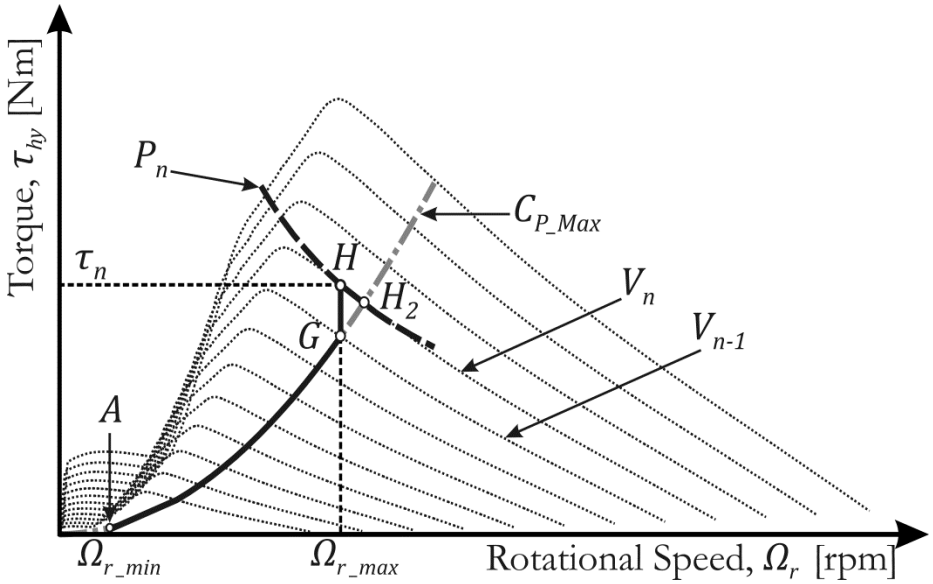

Figure 4.8: Variable-Speed variable-pitch (pitch-to-feather) control strategy (adapted from Bianchi, De Battista & Mantz, 2010, P.69).

4.2.5 Power Regulation by Stall

This is summarized in Figure 4.9 both for passive and speed-assisted stall regulation. Below rated both turbines operate in variable-speed mode and track the C_{P_Max} locus. The passive stall regulated turbine operates between points A and E in flow speeds below rated. If E is reached, the speed is limited and the turbine follows segment ED. At D, representing the maximum power that can be generated, the turbine goes into deep stall with flow separation occurring along the length of the blade. For flow speeds above this point the hydrodynamic power reduces and the turbine operation moves back along ED to G. Therefore, a passive stall regulated turbine is unable to maintain rated output power. The power falls away as the turbine goes deeper into stall as shown in Figure. 4.10.

On the other hand, the speed-assisted stall turbine operates between A and B (Figure. 4.9) in flow speeds below rated. At B, rotational speed is limited and the turbine follows segment BC, reaching rated power at C. As flow speed increases the generator torque increases to reduce speed and drag the rotor into stall, whilst keeping the turbine operating on the rated power curve P_n. Eventually the turbine goes into deep stall at D, and moves back along segment CD to G_1. The power curve for the assisted stall scheme is in Figure 4.10. It shows that rated power (P_n) is maintained up to the cut-out flow speed (V_{max}). Since the speed-assisted regulation allows a TST to follow the ideal power curve, this strategy is seen as superior to passive stall regulation. Therefore, the speed-assisted stall regulation is proposed for use in this thesis.

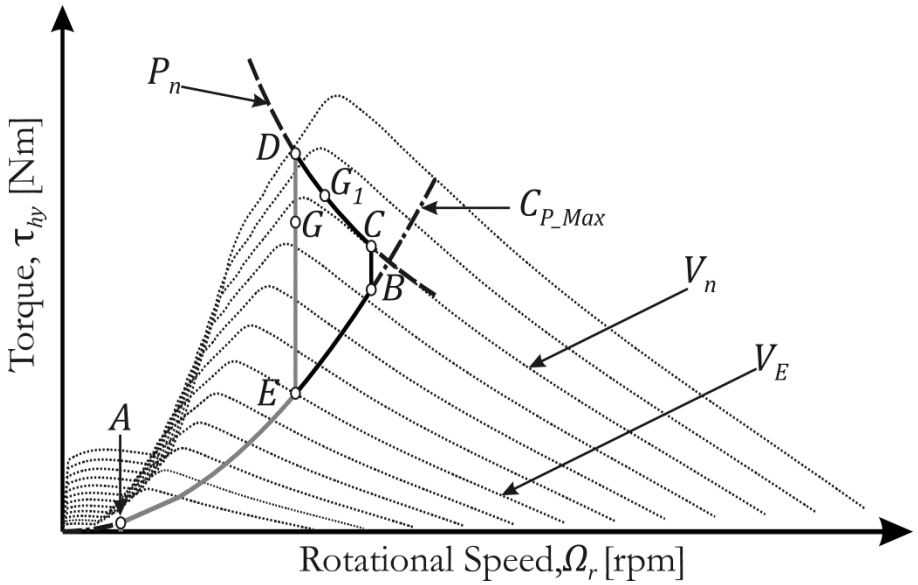

Figure 4.9: Variable-speed fixed pitch control strategies with passive ($AEDG$) and speed-assisted ($ABCDG^1$) stall regulation (adapted from Bianchi, De Battista & Mantz, 2010, P.66).

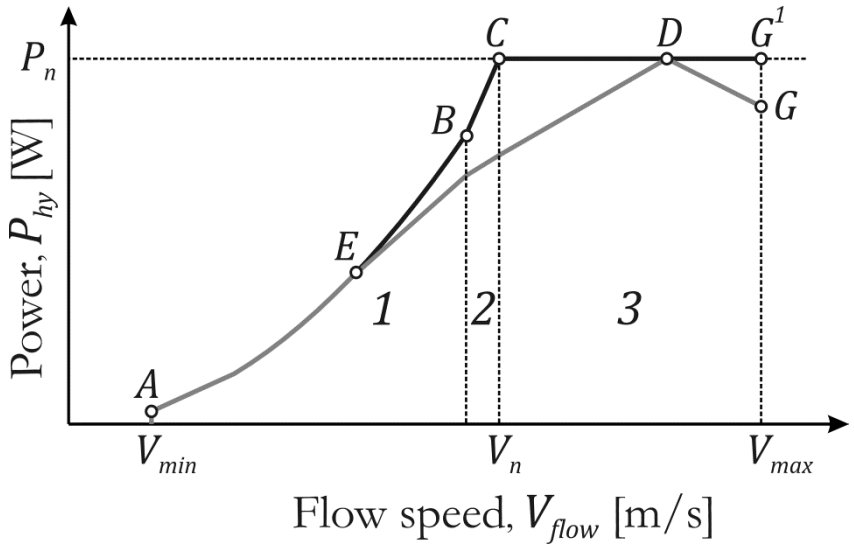

Figure 4.10: Power curve for variable-speed fixed pitch control strategies with passive ($AEDG$) and speed-assisted ($ABCDG^1$) stall regulation.

4.3 Rotor Design and Modelling

4.3.1 Tidal Stream Turbine Model Description

Two generic 1 MW TST models have been developed and verified using GH Tidal Bladed®. The salient characteristics of each turbine model are in Appendix D.1.

An effort was made to keep both turbine models as similar as possible so that a fair comparison could be made. Each rotor has three blades and is mounted on a 1.8m diameter hub. An NACA 63-424 series aerofoil defines the primary shape of the turbine blades. This foil was chosen because it is a relatively thick section (necessary to provide adequate structural strength) while still offering a good lift to drag ratio. Bir, Lawson & Li (2011) have also recommended the use of NACA 63 series foils on TSTs because they are more resistant to cavitation than other foils and less sensitive to leading edge roughness.

The C_l/C_d ratio is called the glide ratio. Values greater than 100 are not uncommon and the angles of attack at which the maximum ratio occurs are typically in the range 5 – 10°. The coefficients of lift (C_l) and drag (C_d) as a function of angle of attack for the NACA 63-424 aerofoil section were obtained numerically using XFOIL (Drela, 1989). The results are shown in Figure 4.11. From this figure the glide ratio is at a maximum when the angle of attack is 7.5°, and it has a value of 118. It can also be seen that at about 25° the glide ratio drops rapidly as C_d increases and C_l decreases.

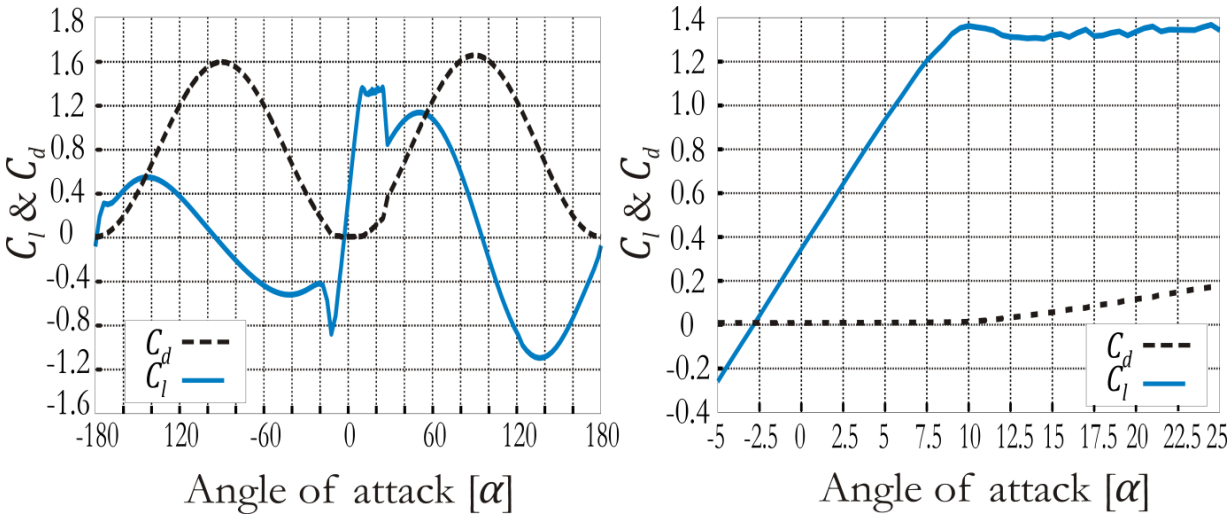

Figure 4.11: Coefficients of lift C_l and drag C_d as a function of angle of attack (left: -180° < α > 180°; right: -5° < α < 25°)

4.3.2 Optimal Blade Design

To design a turbine rotor blade that uses a particular aerofoil shape the geometric parameters (chord length and twist angle along the blade span) need to be specified. These parameters will determine the blade plan shape. The rotor design equations are derived using the BEM theory. Usually a designer will design the blades to operate with optimum efficiency at the specified design condition *i.e.* the blade is designed so that the power coefficient is at a maximum when the blade is operating at the design TSR. It was shown earlier in the chapter that for a given TSR the power coefficient is a function of both the axial (a) and angular induction factors (a'). It was also shown that the power coefficient reaches a maximum when $a = \frac{1}{3}$. For optimised operation, as well as the axial induction factor being equal to $\frac{1}{3}$, the tangential induction factor (a') along the blade span must follow the relationship (Burton, et al., 2001):

$$a' = \frac{1-a}{\lambda^2 r^2} \tag{4.36}$$

Changing the induction factors away from these values will reduce the amount of power available to the rotor. The power coefficient derived from general momentum theory is as given in equation (4.28). This equation expresses the power coefficient purely as a function of the local TSR, and the axial and tangential induction factors with no consideration being given to blade geometry. By combining the momentum theory with the blade element theory it is possible to relate the power coefficient to the geometry of the blade as follows:

$$C_{P=}\frac{8}{\lambda^2}\int_{\lambda_H}^{\lambda} F\lambda_r^3 a'(1-a)[1-\left(\frac{C_d}{C_l}\right)\cot\varphi]d\lambda_r \tag{4.37}$$

From equation (4.37) it can be seen that the power coefficient depends not only on the local TSR $(\lambda_r)$and the axial (a) and tangential (a') induction factors but also on the glide ratio (C_l/C_d), the tip-loss factor (F) and the relative wind angle (φ). Normal design procedure is to select the aerofoil shape first, the glide ratio included in equation (4.37) can then be chosen so that it has a maximum value. This can be found from the two dimensional polar diagram, like that shown in Figure 4.11, of that aerofoil. Note, that when $C_d \approx 0$ equation (4.37) is the same as that derived from general momentum theory (equation 4.28). The remaining terms in equation (4.37) are the tip-loss factor, relative wind angle and the local TSR. For a given blade number the tip-loss factor depends solely on the relative wind angle and the local TSR. So by establishing a

relationship between the relative wind angle and the local TSR the optimum relative wind angle for a certain local TSR can be determined. The relationship is given as follows (Manwell, McGowan & Rogers, 2002):

$$\varphi_{opt} \approx MAX\{sin^2\varphi(cos\varphi - \lambda_r sin\varphi)(sin\varphi + \lambda_r cos\varphi)\} \tag{4.38}$$

The optimisation can be performed by taking the partial derivative of equation (4.38) and setting it equal to zero:

$$\frac{\delta}{\delta\varphi}\{sin^2\varphi(cos\varphi - \lambda_r sin\varphi)(sin\varphi + \lambda_r cos\varphi)\} = 0 \tag{4.39}$$

After some algebra equation (4.39) reveals equations for the relative wind angle and chord length distribution for a Betz optimum blade operating at a particular TSR. They are as follows:

$$\varphi_{opt} = \frac{2}{3} tan^{-1}\left(\frac{1}{\lambda_r}\right) \tag{4.40}$$

$$C = \frac{8\pi r}{BC_l}(1 - cos\varphi) \tag{4.41}$$

For practical reasons, such as cost and ease of fabrication, rotor blades are not always optimal. Often simplifications will be made such as (Schubel, Crossley, 2012):

- Reducing the angle of twist.
- Linearization of the chord distribution.
- Reducing the number of differing aerofoil profiles.

Despite this it is common practice to start off with an optimum blade shape, and then to make modifications as required.

4.3.3 Blade Design Procedure

The design procedure begins by dividing each blade into i number of sections, each of which is a distance r from the centre of rotation and dr thick. Next an estimate of the rotor diameter required to produce the desired power output is needed. This can be calculated from the following equation:

$$P = \frac{1}{2}\rho\pi R^2 {V_{flow}}^3 C_{P\_opt}\eta \tag{4.42}$$

At this stage C_{P_opt} is estimated in order to provide an initial blade length. For this design C_{P_opt} is estimated to be 0.42, the efficiency (η) is assumed to be 0.95, and the water density (ρ) is 1027kg/m^3. Assuming the remaining variables are as given in Appendix D.1 then using equation (4.42) the blade radius (R) is 10.6m.

The Local TSR at each blade section is then calculated using equation 4.43 and is given as:

$$\lambda_{r,i} = \lambda_{design}\left(\frac{r_i}{R}\right) \tag{4.43}$$

where λ_{design} is the TSR selected prior to design. Several aspects such as torque, mechanical stress, noise and cavitation[5] need to be considered when selecting an appropriate TSR. Increasing the TSR can increase efficiency (Hau, 2006), however high TSRs lead to increased noise and cavitation. As discussed by Fraenkel (2002) the need to avoid the occurrence of cavitation means that blade tip velocities on TSTs need to be limited to around 12-15m/s. This means that for a blade of a given length there will be a maximum limit on the TSR that can be selected. Higher TSRs also lead to slimmer blades with reduced chord lengths, which can lead to cost reduction due to less material being used in the blades. However, if blades are too slim difficulties will be experienced with maintaining structural integrity and ensuring the survivability of the blades. For three bladed axial flow rotors TSRs in the range 4-10 are recommended (Manwell, McGowan & Rogers, 2002). The rotors designed in this thesis assume a design TSR of 5.6. This value was arrived at after a number of design iterations and seemed to offer good performance while ensuring that the blades were thick enough to provide reasonable structural strength.

[5] Cavitation occurs when the pressure in a flowing liquid drops below the vapour pressure of the liquid and then subsequently increases again. This process leads to the generation and implosion of cavitation bubbles. Implosion of these cavitation bubbles on the surface of turbine or propeller blades leads to cyclic stress which will ultimately damage the blades. A comprehensive treatise of cavitation and its effects is given in Franc & Michel (2005).

Having chosen a design TSR the optimum relative wind angle for each blade section is determined as follows:

$$\varphi_{opt,i} = \frac{2}{3} tan^{-1}\left(\frac{1}{\lambda_{r,i}}\right) \tag{4.44}$$

Finally the chord length at each section along the blade is determined as follows:

$$C_i = \frac{8\pi r_i}{BC_{l\_design}}\left(1 - cos\varphi_{opt,i}\right) \tag{4.45}$$

where C_{l_design} is chosen so that the glide ratio is at a maximum at each blade element. From Figure 4.11 it can be seen that this occurs when $C_{l\_design} = 1.204$. Finally the twist distribution is determined using equation (4.46), which is derived from Figure 4.5 and given as:

$$\theta_{P,i} = \varphi_{opt,i} - \alpha_{design} \tag{4.46}$$

where α_{design} is the angle of attack corresponding to the chosen design lift coefficient $C_{l,design}$. From Figure 4.11 $\alpha_{design} = 7.5°$. A circular cross section is used at the blade root of both the pitch and stall regulated turbine blades. The circular section transitions to the NACA-63-424 airfoil shape at 23% of the blade span. Furthermore, when designing the blades the chord distributions are kept the same in both the pitch and stall regulated turbines, varying from a maximum length of 1.67m near the root to 0.47m at the tip. Only the twist distributions (Figure. 4.12) of each blade are varied to obtain the desired operating characteristics. A full description of the chord and twist distributions as well as the variation of structural properties along the length of both the pitch and stall regulated blades is provided in Appendix D.3 and D4 respectively.

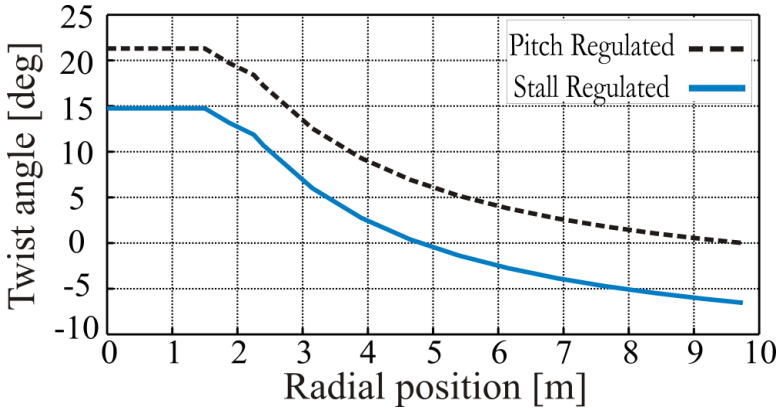

Figure 4.12: Twist angle distributions for pitch and stall regulated blade designs.

As can be seen in Figure 4.12, the twist distribution of the stall regulated blade is chosen such that it will operate at a higher angle of attack closer to stall and shed power as the flow speed increases. This is confirmed by its narrower C_P curve shown in Figure 4.13. In above rated operation, (segment CD of Figure. 4.9), the turbine will require a limited speed reduction to maintain constant power, ensuring that the generator rated torque is kept within limits. Unfortunately this means that it is less efficient than its pitch counterpart. This is evidenced by the peak C_P values in Figure 4.13 of 0.414 for the stall regulated rotor and 0.447 for the pitch regulated rotor. The result is an increase in axial load (more force is transferred into axial load rather than into rotating the blade), likely to be higher for the stall regulated rotor. As discussed by Bourlis and Bleijs (2010) it is common for turbines using stall regulation to have steep peaky C_P curves.

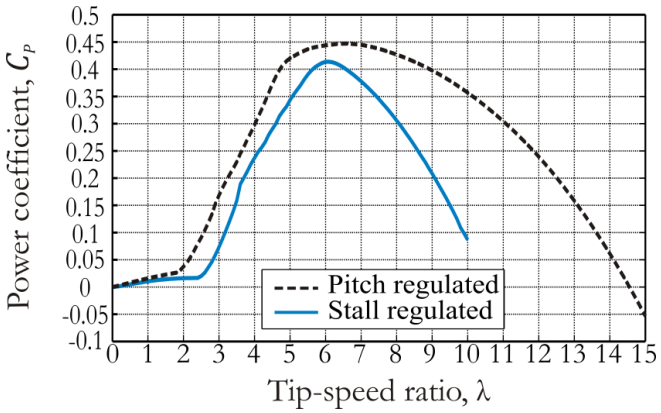

Figure 4.13: C_P curves for pitch and stall regulated rotors

These C_P curves were obtained by inputting the blade designs for both the assisted stall and pitch regulated turbines in GH Tidal Bladed®. In Chapter 5 a more detailed performance assessment and comparison between the pitch and assisted stall regulated turbines will be undertaken, with performance under turbulent flows, loading and energy yield being evaluated in GH Tidal Bladed®.

Chapter 5

5. Performance of Pitch and Stall Regulated Tidal Stream Turbines

Summary:

The control strategies introduced in Chapter 4 for a stall and pitch regulated horizontal axial flow, variable speed TST are implemented. In below rated flow speeds both turbines are operated in variable-speed mode so that the optimum TSR is maintained. One of the turbines has variable pitch blades, which in above rated speed are pitched to feather in order to regulate power. The other turbine has fixed pitch blades and uses a speed-assisted stall strategy to regulate power above rated flow speed. The dynamic characteristics of each turbine model are examined, and the control system design behind both strategies is done in MATLAB. Following implementation of the controllers, a comparative analysis in terms of performance under turbulent flows, loading and energy yield is carried out using GH Tidal Bladed®.

5.1 Comparative Assessment of Pitch and Stall Regulated Turbines

5.1.1 Steady State Performance and loading Analysis

Two variable speed turbine models have been developed and control strategies appropriate for use with each model were proposed. The parameters of each TST model are given in Appendix D.1. In both cases a frequency converter (as detailed in Chapter 2) is used to decouple the generator from the fixed frequency of the grid. The TST configuration used for each model is shown in Figure 5.1.

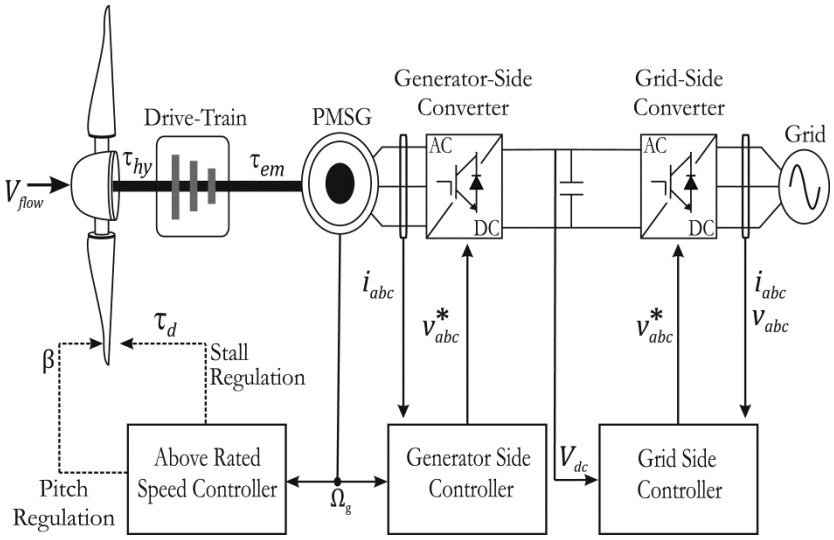

Figure 5.1: TST configuration based on a TST and a full power converter.

Both models were implemented in GH Tidal Bladed® and the steady power output (P), thrust force (F_T), out-of–plane blade root bending moment (M_y), and in-plane blade root bending moment (M_x) were computed. M_x acts about an axis parallel to the rotor plane and is driven primarily by inertial and gravitational forces, whereas M_y acts perpendicular to the rotor plane and is primarily driven by F_T (Milne, et al., 2010). The coordinate system is shown in Figure 5.2 followed by the steady outputs in Figure 5.3.

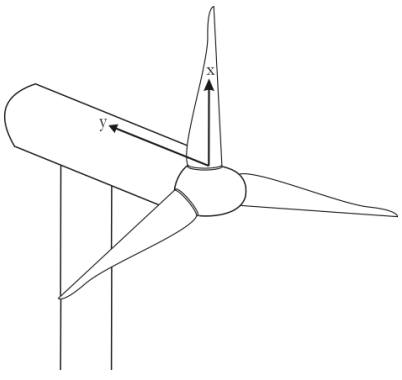

Figure 5.2: Blade coordinate system

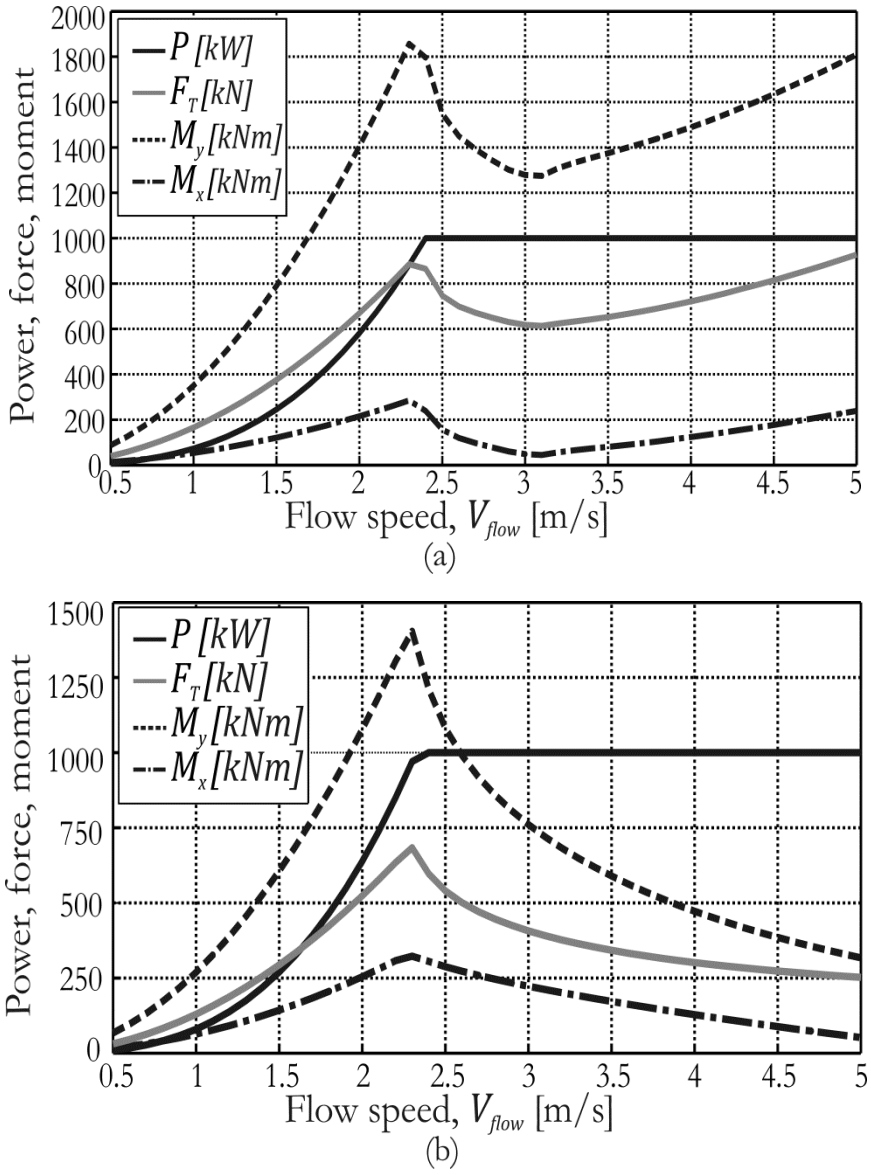

Figure 5.3: Steady outputs (power, thrust force and blade root bending moments) as function of flow speed: (a) speed-assisted stall regulation; (b) pitch regulation.

The results in Figure 5.3 are for steady state conditions only. The impact of structural and controller dynamics, and time varying environmental conditions such as turbulence and shear, are not accounted for at this stage.

F_T is higher for the stall regulated turbine over the entire operating range. This is due to the design of the blades, which on the stall regulated turbine have been designed to operate at a higher angle of attack closer to stall (Manwell, McGowan & Rogers, 2002). M_y dominates in both cases, being higher for the stall regulated TST over the entire operating range of the turbine. In contrast, M_x is significantly lower for both turbines and of a similar magnitude.

The performance coefficients for the pitch and stall regulated rotors are shown in Figure 5.4. The maximum power coefficient (C_P) for the stall regulated rotor is 0.414 compared with 0.447 for the pitch regulated rotor. These values occur at a TSR of about 6. This is the TSR that the rotor operates at when extracting maximum power. It can be seen that the thrust coefficient of the stall regulated rotor is 24% higher at the operating point than the pitch regulated rotor. This explains the higher thrust forces seen in Figure 5.3 for the stall regulated rotor.

The points at which the torque coefficient curves (C_Q) cross the x axis in Figure 5.4 are the points to which each of the rotors will accelerate if they are simply allowed to freewheel as the flow speed increases. Such a scenario could occur if the generator reaction torque was lost due to a network connection failure. This point is referred to as the runaway point (Winter, 2011b).

The thrust coefficient (C_T) for the stall regulated rotor at the runaway point is 86% higher than for the pitch regulated rotor. So over speeding of the stall regulated rotor would be undesirable and will result in a significant increase in the thrust force, which will need to be absorbed by the support structure.

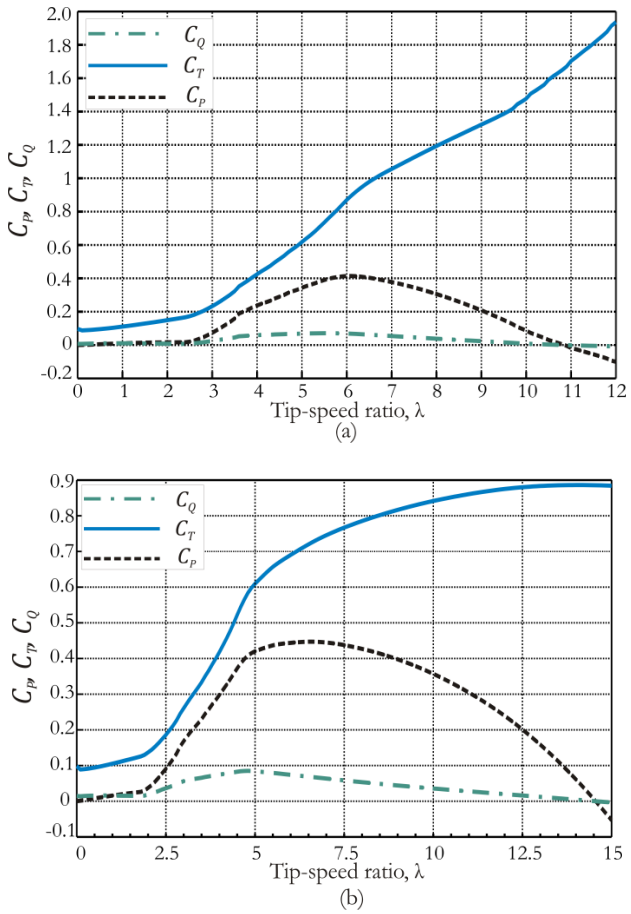

Figure 5.4: Performance Coefficients: power coefficient (C_P), thrust coefficient (C_T) and torque coefficient (C_Q) as a function of tip-speed ratio: (a) Assisted stall regulated rotor; (b) Pitch regulated rotor.

5.1.2 Control System Design

To compare the loads and energy yield under dynamic inflow conditions, with a fully dynamic controller and with the modal dynamics of the rotor blades included it is necessary to specify and tune controllers for both turbines. Below rated both turbines operate in variable speed mode, where the rotor speed is varied by controlling the generator reaction torque in accordance with equation (2.8), so that the turbine follows an optimal torque vs. speed curve. The optimal torque reference is obtained through a look-up table. Since the electric time constant is much smaller than the mechanical time constant of the system, the electrical dynamics are assumed to be in steady state. Therefore, for the controllers designed in this section the variable speed drive, consisting of both the PMSG generator and frequency converter, is modelled as a first order lag with time constant $\tau = \frac{1}{L_{sq}+R_s}$. R_s is the PMSG stator resistance and L_{sq} is the generator stator inductance in the q-axis.

The blades and the support structure of each turbine are modelled as single linear flexible components using a modal approach whereby the structural dynamics are represented as modes with a specific frequency and shape. This means that the effects of blade flexibility and vibrations on the performance and mechanical loading of the turbine can be accounted for. Garrad Hassan & Partners Ltd (2009) recommends that as a minimum 4 blade modes should be considered: two flapwise (deflections in the out-of-plane direction) and two edgewise (deflections in the in-plane direction). Only the modal dynamics relating to the rotor blades of each turbine (4 modes in total) are considered in this work. Details of the blade modes for each turbine and their respective frequencies are given in Appendix D.2.

5.1.3 Pitch Regulated Tidal Stream Turbine Control

The steady-state operating curve for the variable speed pitch regulated TST is reviewed in Figure 5.5. Below rated (between points A and H) the turbine operates in variable speed mode and the pitch angle is set to fine pitch to extract the maximum power available from the flow. Once rated torque (τ_n) is reached at point H the generator torque demand is held constant and the pitch angle of the blades is adjusted in order to regulate the rotor speed and keep the turbine operating on the constant power curve (P_n) at point H.

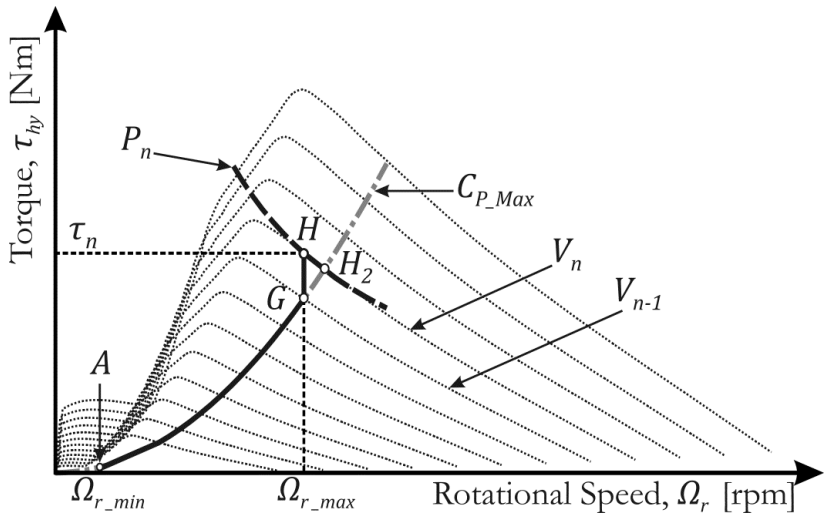

Figure 5.5: Variable-Speed variable-pitch (pitch-to-feather) control strategy (adapted from Bianchi, De Battista & Mantz, 2010, P.69).

Figure 5.6 shows a simple model of the pitch system which is active in above rated flow speeds. The transfer function relating the pitch angle demand (β_{ref}) to the pitch angle (β) is a first order lag given as:

$$G_{act}(s) = \frac{1}{1 + sT_{act}} \tag{5.1}$$

where T_{act} is the pitch actuator time constant. A rate limiter and an angle limiter are then used to ensure that the actuator limits are not exceeded. All data on the Pitch system is provided in Appendix D.6.

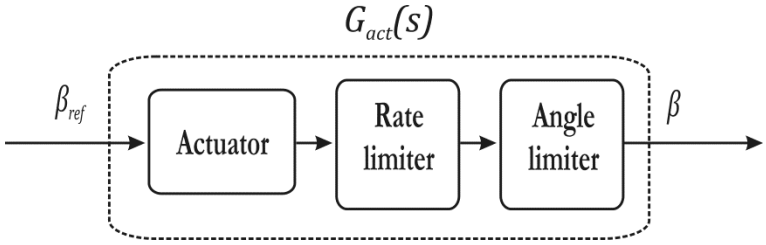

Figure 5.6: Pitch System Model.

Figure 5.7 shows the pitch angle control loop for a pitch regulated TST (Burton, et al., 2001). This is active above rated, with the generator torque demand (τ_d) held constant. The controller generates the pitch angle demand (β_{ref}) from the generator speed error. This is sent to the pitch system, where rate and position limits are applied. The output from the pitch system is the pitch position demand (β) which is sent to the plant. The plant in Figure 5.7 is a simplified dynamic model containing selected dynamics related to the turbine and is assumed to be a single input single output system (SISO).

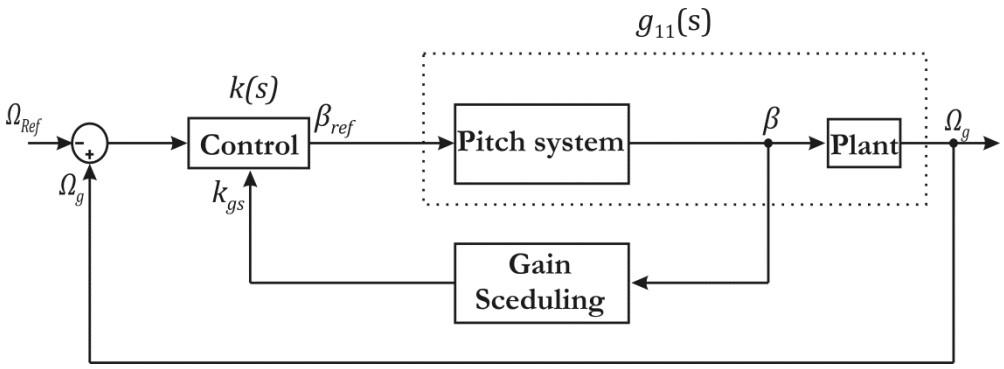

Figure 5.7: Pitch angle Control for above rated Flow Speed.

The pitch system and plant dynamics were derived using the linearisation module of GH Tidal Bladed® (Garrad Hassan & Partners Ltd, 2009). The module linearises each turbine model at a number of steady-state operating points and gives the model states and selected outputs at each operating point. The linearised model of the pitch system and plant at each operating point is provided in state-space form as:

$$\Delta\dot{x} = A\Delta x + B\Delta u \tag{5.2}$$

$$\Delta y = C\Delta x + D\Delta u \tag{5.3}$$

where Δu is the control input vector, Δx is a vector of system states, and Δy is a vector of outputs. A, B, C and D are the state-space matrices where A represents the state matrix, B is the control input gain matrix, C relates the measured output Δy to the turbine states and D relates the control input to the output.

The linearisation module allows the user to generate simplified linear models that contain only a subset of the total dynamics of the turbine. The decision to neglect certain dynamics will depend on the user's objective. For the pitch controller design the model is simplified so that the state of the plant at each operating point is defined by thirty state variables (*i.e.* the state matrix is a 30 x 30). Dynamics relating to the rotor blades and the pitch system are included in the linearised model. To simplify the control design dynamics related to the support structure are neglected. This simplified model is suitable to describe the dominant dynamics and to formulate the control strategy. A full list of the state variables contained in Δx, for the pitch controlled turbine model, is given in Appendix D.5.

After combining the dynamics of the pitch system with those of the plant the system is as shown in Figure 5.8

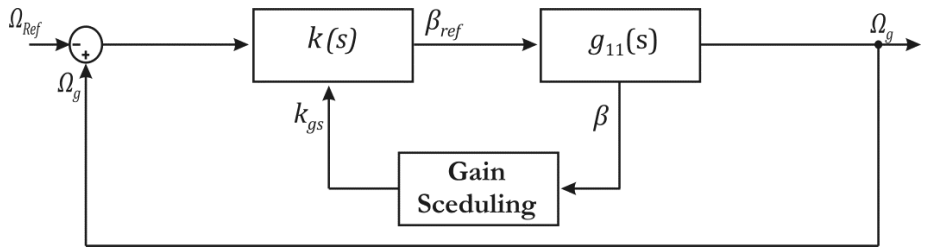

Figure 5.8: Pitch control: $g_{11}(s)$ contains the dynamics of the pitch system and plant, $k(s)$ is the controller. k_{gs} is a gain that is applied as a function of the pitch angle β.

$k(s)$ is the transfer function of the controller and $g_{11}(s)$, representing the combined dynamics of the pitch system and plant, is a transfer function relating pitch angle demand (β_{ref}) to rotational speed (Ω_g). k_{gs} is a gain applied as a function of pitch angle (β). The transfer function $g_{11}(s)$ was obtained from the state-space model of (5.2) and (5.3) using the equation (Ogata, 1996):

$$g_{11}(s) = [C(sI - A)^{-1}B + D]u(s) \tag{5.5}$$

where A, B, C and D are the state-space matrices, I is an identity matrix and $u(s)$ is an input vector. Using equation (5.5) a system of the form shown in (5.6) was obtained relating pitch position demand (β_{ref}) and generator speed (Ω_g).

$$\Omega_g(s) = g_{11}(s)\beta_{ref}(s) \tag{5.6}$$

Since the dynamics of the turbine vary non-linearly according to the operating point, and hence the flow speed, a series of transfer functions $(g_{11}(s))$ relating β_{ref} to Ω_g were obtained at operating points ranging from rated flow speed up to 5.0m/s in steps of 0.1m/s. All of the open loop transfer functions $(g_{11}(s))$ have the same structure, which is given as follows:

$$g_{11}(s) = k_{11} \cdot \frac{(s + z_{11})}{(s + 5)(s + p_{11})} \cdot \frac{n_{11}(s)}{d_{11}(s)} \tag{5.5}$$

where k_{11} is a gain, p_{11} is a left-hand plane pole (LHPP) in the range of 2.9-15.4 rad/s; z_{11} is a left-hand plane zero (LHPZ) in the range of 39-79 rad/s. $n_{11}(s)$ are polynomials with complex conjugate zeroes of high frequency in both the left half plane (LHP) and the right half plane (RHP). $d_{11}(s)$ are polynomials with complex conjugate poles of high frequency in the LHP. All poles and zeros contained in $n_{11}(s)$ and $d_{11}(s)$ are related to the dynamics of the rotor blades. The location of the poles and zeros in $g_{11}(s)$ varies with operating point leading to a series of unique transfer functions which describe the plant over the entire operating range of the pitch mechanism. Figure 5.9(*a*) shows the Bode plot of all $g_{11}(s)$ as functions of flow speed (V_{flow}).

Figure 5.9(b) shows frequencies before the occurrence of the resonances present in 5.9(a). Since $g_{11}(s)$ is an open loop transfer function the plots show the open loop characteristics.

Inspection of all $g_{11}(s)$ shows that they are stable for all flow speeds; however, one non-minimum phase zero pair (or right-hand plane zero, RHPZ) is present in $n_{11}(\mathrm{s})$. It is known that RHPZs impose limitations on the achievable performance by introducing phase lag into the system (Doyle, Francis & Tannenbaum, 1990). In addition, the presence of weakly damped complex conjugate LHPPs in $d_{11}(\mathrm{s})$ and LHPZs in $n_{11}(\mathrm{s})$ results in resonant and inverse resonant peaks in the magnitude plot and a sudden change of phase angle in the phase plot. This can clearly be seen in Figure 5.9(a). These undesirable dynamics occur at frequencies above 10^4 rad/s. To avoid these undesirable dynamics, which are associated with the blade modes, the bandwidth of the controller $k(s)$ is restricted to at least a decade below 10^4 rad/s.

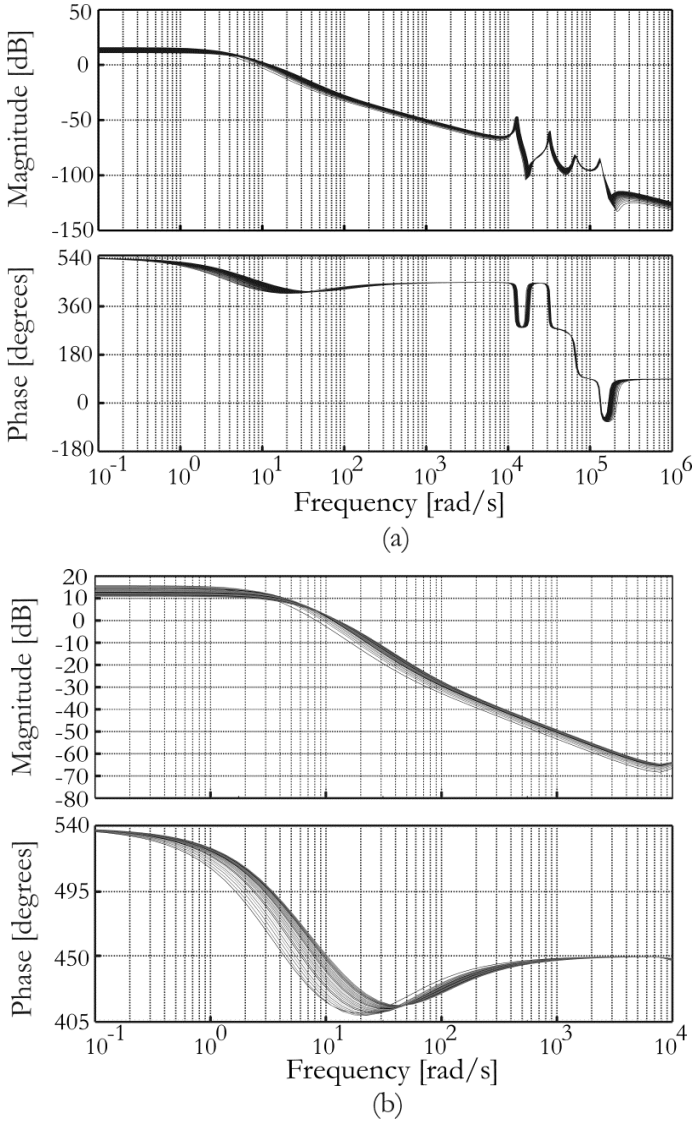

Figure 5.9: Bode plot of $g_{11}(s)$ for (a) frequency regions including resonant poles and zeroes; (b) low frequencies before the occurrence of resonances.

A control design for $k(s)$, given in (5.6) as $k_{c\_pi}(s)$, that provides satisfactory performance was achieved as follows:

$$k_{c\_pi}(s) = k_{gs} \cdot \frac{(s+3)}{s} \tag{5.6}$$

It consists of a proportional integral (PI) controller. The gain k_{gs} is adjusted for each above rated operating point. This gain scheduling is necessary to compensate for the non-linear behaviour of the turbine above rated flow speed. When operating close to the rated flow speed the hydrodynamic torque is less sensitive to changes in pitch angle than when the turbine is operating in higher flow speeds. So more control gain is required at low flow speeds, close to the rated value, than at higher flow speeds. Therefore, k_{gs} in (5.6), was adjusted as a function of blade pitch angle (β), to achieve a similar bandwidth for all the plants over the entire operating range of the pitch mechanism. The set of gains (k_{gs}) is given in Appendix D.7.

Figure 5.10 shows the bode plot for the open loop system including the dynamics of the PI controller of (5.6) $\left(K_{c\_pi}.g_{11}(s)\right)$. The indicators of performance which can be inferred from the open loop frequency response are the gain crossover frequency (point where the open loop frequency response crosses 0 dB), phase margin and gain margin. A larger crossover frequency indicates faster response. Gain and phase margin are measures of stability in closed loop and larger values indicate higher relative stability (Ogata, 1996). Generally a gain margin of at least 6 dB and a phase margin of at least 40 degrees are considered satisfactory (Kundur, 1994). For the system $\left(K_{c\_pi}.g_{11}(s)\right)$ in Figure 5.10 the bandwidth is in the region of 135-170 rad/s and the stability margins for all cases are satisfactory (phase margin: $M_{ph} >$ 60 degrees; gain margin $M_g \approx$ 15 dB). These characteristics reflect in an adequate step response shown in Figure 5.11.

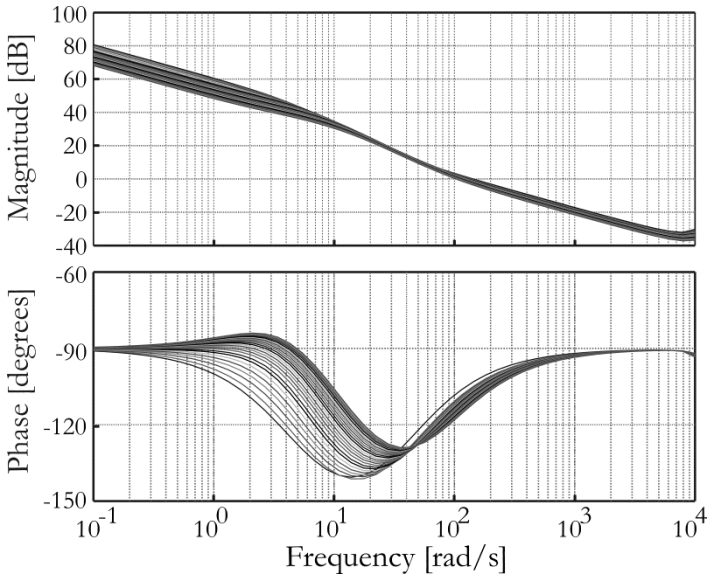

Figure 5.10: Performance assessment of pitch control loop using PI control structure: Bode plot of $K_{c\_pi} \cdot g_{11}(s)$ for frequencies below 10^4 rad/s.

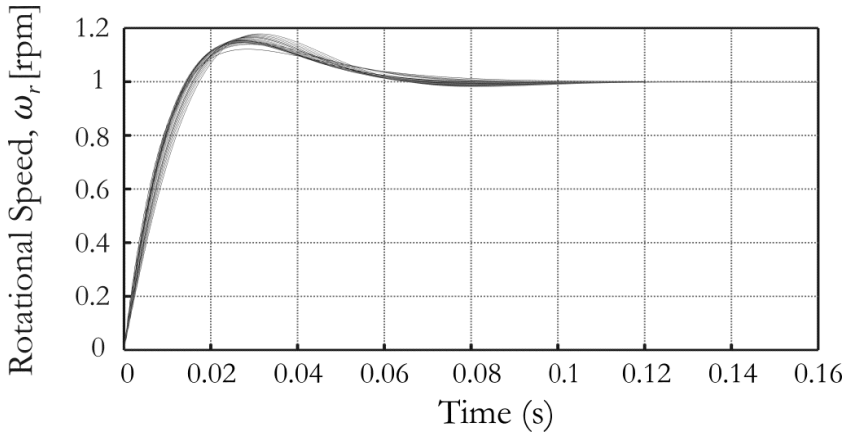

Figure 5.11: Performance assessment of the pitch control loop using PI control structure: step response.

Although the performance of the PI controller of (5.6) is satisfactory it can be improved, which is evident from Figure 5.11 where the step responses exhibit an overshoot of 15-20%. Lifting the phase at the gain crossover frequency will increase the phase margin and reduce the overshoot. This is achieved by adding a lead term to the PI controller of (5.6) producing a new control structure $K_{\text{c\_pi\_lead}}(s)$, which is given as follows:

$$K_{c\_pi\_lead}(s) = k_{gs} \cdot \frac{(s+7.5)}{s} \cdot \frac{(s+12)}{(s+60)} \tag{5.7}$$

Figure 5.12 shows the Bode plot of the open loop system $\left(K_{c\_pi\_lead} \cdot g_{11}(s)\right)$, with the inclusion of a lead term, for frequencies below 10^4 rad/s. It can be seen that the phase has been lifted at the gain crossover frequency and the bandwidth has increased for all conditions and is now in

the region of 225-320 rad/s. The control design also has a higher phase margin ($M_{ph} \approx 90$ deg). However, the gain margin is slightly reduced ($M_g \approx 10$ dB) through the inclusion of the additional lead term. The improvement made by this controller reflects in the step response of Figure 5.13, where it can be seen that the overshoot present in Figure 5.11 has been eliminated.

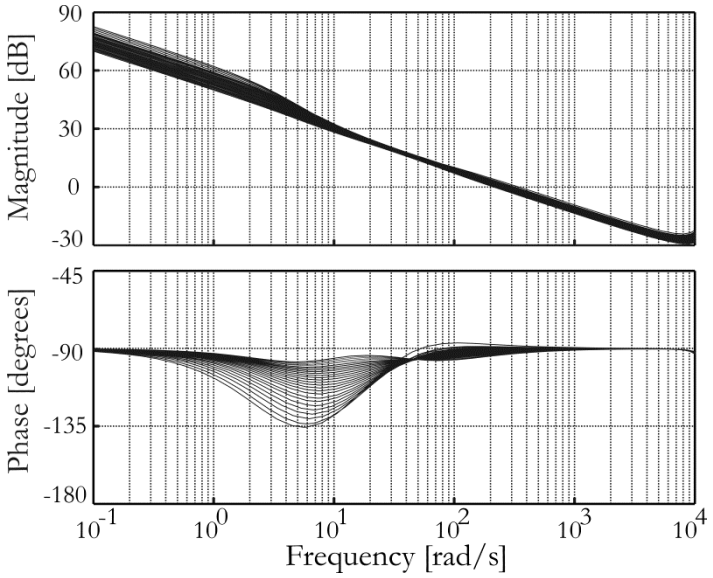

Figure 5.12: Performance assessment of pitch control loop with additional lead term: Bode plot of $K_{c\_pi\_lead} \cdot g_{11}(s)$ for frequencies below 10^4 rad/s.

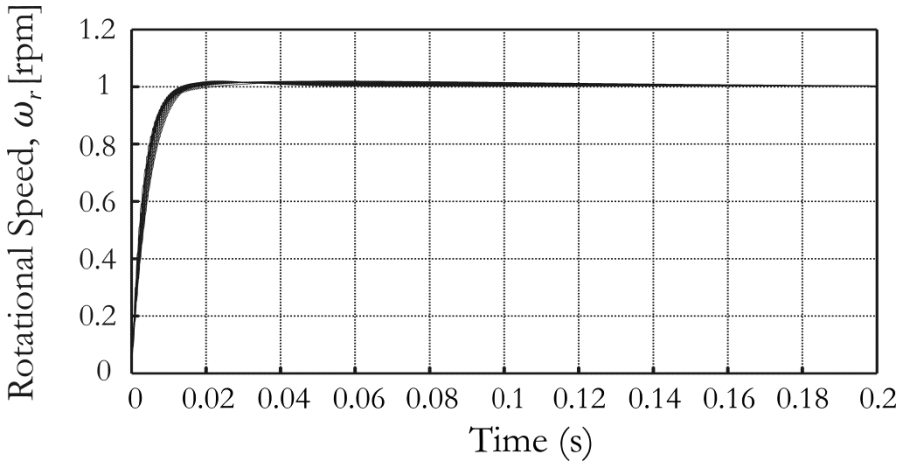

Figure 5.13: Performance assessment of the pitch control loop with additional lead term: step response.

5.1.4 Stall Regulated Tidal Stream Turbine Control

The steady-state operating curve for the variable speed stall regulated TST is reviewed in Figure 5.14. The objective in above rated flow speeds (segment CDG^1) is to keep the turbine operating on the rated power curve (P_n).

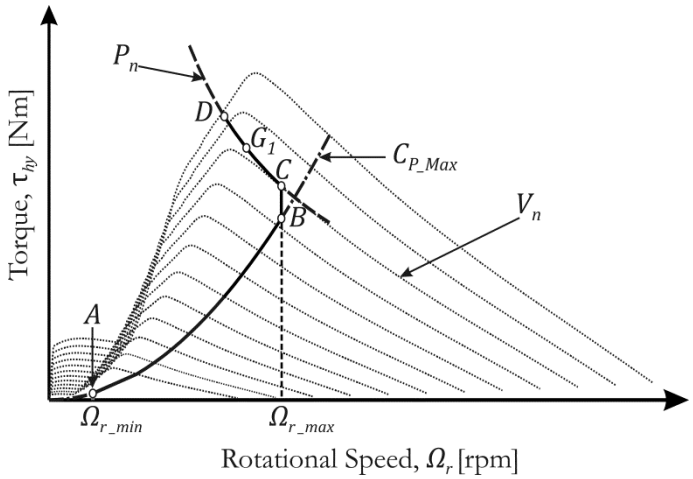

Figure 5.14: Variable-speed-assisted stall regulation control strategy (adapted from Bianchi, De Battista & Mantz, 2010, P.66).

A number of methods for controlling speed-assisted stall regulated wind turbines (which could equally be applied to TST's) are discussed in the literature (Bourlis & Bleijs, 2010; Ekelund, 1994; Boukhezzar & Siguerdidjane 2005). One method is to use a speed feedback loop, as shown in Figure 5.15, where the speed is regulated in order to keep the turbine operating at rated power. To obtain the speed reference (Ω_{Ref}) Bourlis & Bleijs (2010) propose the use of a Kalman filter whereby the hydrodynamic torque is estimated by using a measurement of the generator rotational speed. They then obtain the speed reference as follows:

$$\Omega_{Ref} = \frac{P_n}{\hat{\tau}_{hy}} \tag{5.8}$$

where P_n is the rated power and $\hat{\tau}_{hy}$ is the estimated hydrodynamic torque.

In this thesis, to simplify the controller design and to avoid the use of an observer, it was assumed that a measurement of the turbine's low speed shaft torque (τ_m) was available. The speed reference was then calculated as in (5.8), using the measured torque value (τ_m) rather than the estimated value $(\hat{\tau}_{hy})$. Figure 5.15 shows how the inner speed control loop continuously updates the generator torque demand (τ_d) to ensure that the generator speed (Ω_g) tracks the

reference (Ω_{Ref}). V_{flow} is the flow speed and is used as a gain scheduling variable to tailor the controller to the changes in the dynamics of the turbine as the operating point changes.

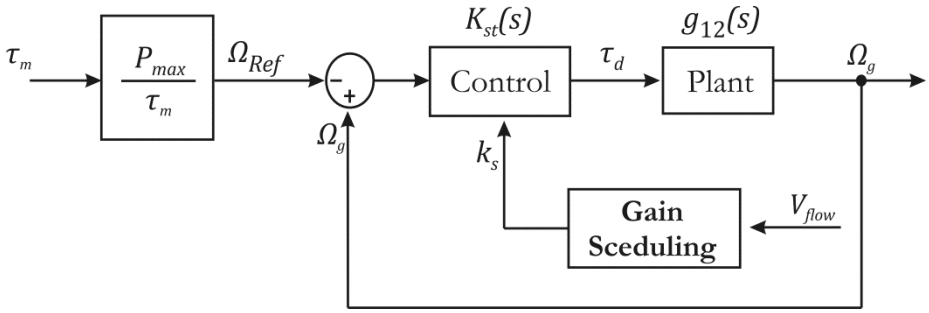

Figure 5.15: Variable-speed stall regulated control strategy

As was the case for the pitch regulated turbine the plant block in Figure 5.15 is a simplified linearised model of the turbine. The linearised model is in state space form as shown in (5.2) and (5.3). Dynamics relating to the rotor blades are included in the linearised model. A full list of the state variables contained in Δx for the stall regulated turbine model is given in Appendix D.5.

Following a similar procedure as for the pitch regulated turbine, a family of SISO plants relating generator torque demand (τ_d) and generator speed (Ω_g) for above rated operating points up to 5.0m/s in steps of 0.1m/s were obtained as follows:

$$\Omega_g(s) = g_{12}(s)\tau_d(s) \tag{5.9}$$

The open loop transfer function of $g_{12}(\mathrm{s})$ has the following structure:

$$g_{12}(\mathrm{s}) = \frac{k_{12}}{(\mathrm{s}+10)(\mathrm{s}-p_{12})} \cdot \frac{n_{12}(\mathrm{s})}{d_{12}(\mathrm{s})} \tag{5.10}$$

where k_{12} is a gain, p_{12} is a RHPP in the range of 0.4-17.7 rad/s. $n_{12}(\mathrm{s})$ are polynomials with complex conjugate zeroes of high frequency in both the LHP and the RHP. $d_{12}(s)$ are polynomials with complex conjugate poles of high frequency in the LHP and the RHP. The location of the poles and zeros present in $g_{12}(s)$ varies with operating point. Figure 5.16(a) shows the open loop response of $g_{12}(s)$ as a function of flow speed V_{flow}. Figure 5.16(b) shows the response before the occurrence of the resonances present in Figure 5.16(a).

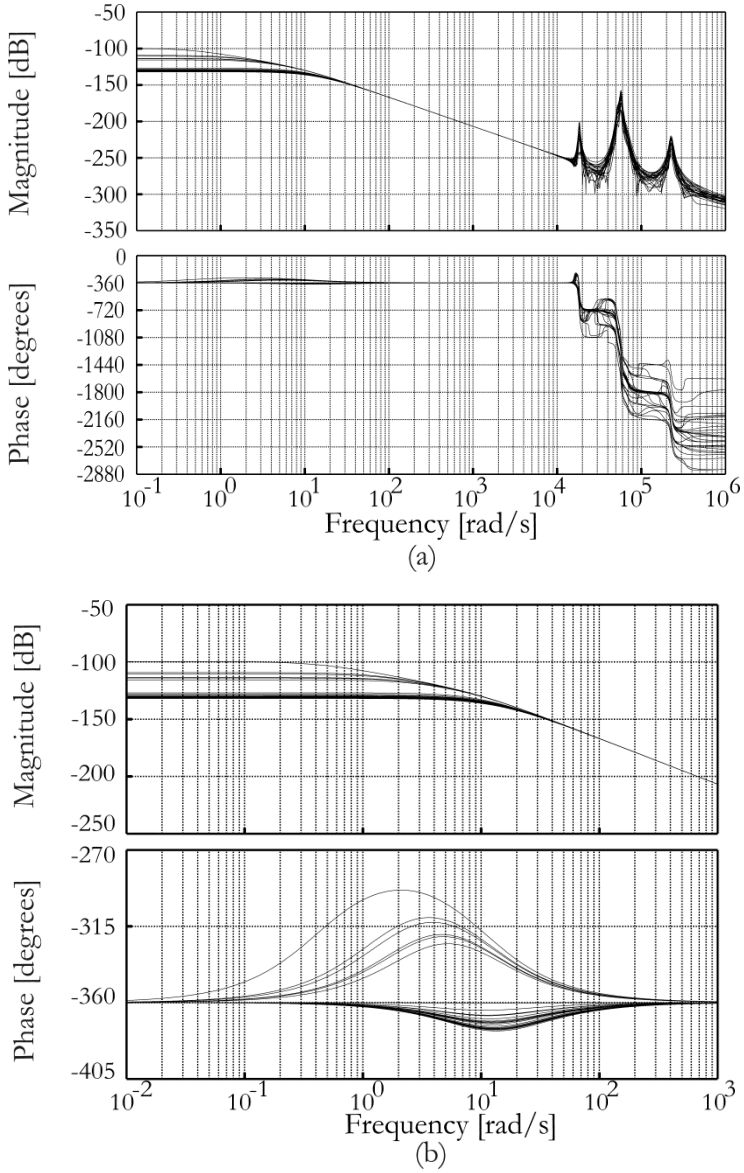

Figure 5.16: Bode plot of $g_{12}(s)$ for (a) frequency regions including resonant poles and zeros; (b) low frequencies.

Looking at the structure of the family of plants $(g_{12}(s))$ given in (5.10) it is clear that they are unstable due to the presence of p_{12}, the low frequency RHPP, which is caused by the hydrodynamics and varies with the operating point. Such instability is not unique to the model in this thesis but is always the case (Leithead & Connor, 2000). Below the rated flow speed (segment ABC of Figure 5.14) the dynamics of the stall regulated turbine are stable; however, above rated (segment (CDG^1) of Figure 5.14) the dynamics are unstable. This instability results from the nonlinear dependence of the hydrodynamic torque (τ_{hy}) on the rotor speed (Ω_r). This is explained by Leithead & Connor (2000). Looking at Figure 5.17, assume that the turbine is operating at rated power (P_n) in the stall region at point a where the rotor speed is Ω_{r_a}, hydrodynamic torque is τ_{hy_a} and the generator torque is τ_{em}. If the rotor speed is then

displaced to Ω_{r_b} then to keep the turbine operating on the line of constant power one might decrease the generator torque ($P = \Omega_r \tau_{em}$). However, decreasing the generator torque will actually cause the turbine to diverge away from point a because the hydrodynamic torque increases with rotor speed in the stall region. So if the rotor speed is displaced from Ω_{r_a} the turbine will move away from the operating point with increasing acceleration and become unstable.

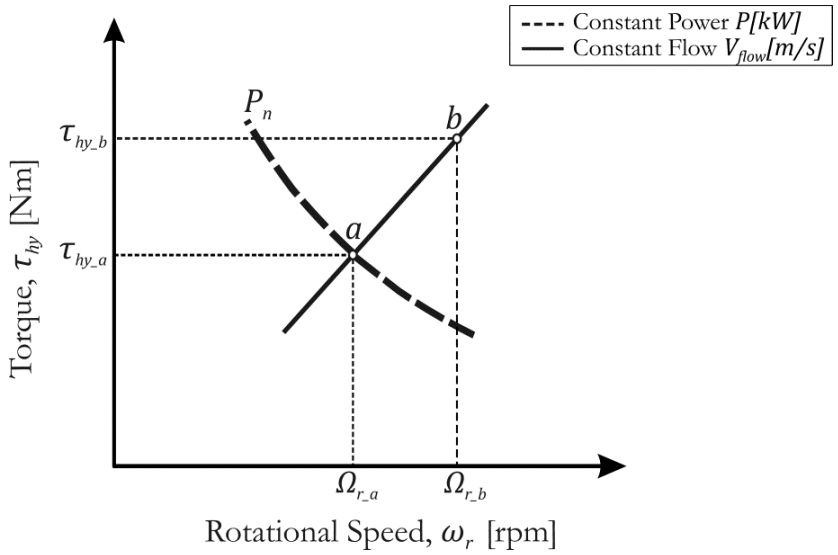

Figure 5.17: Instability of variable speed stall regulated turbine when tracking rated power.

As well as being unstable there are also at least 5 complex pairs of RHPZs that appear in each $n_{12}(s)$ in the family of plants $(g_{12}(s))$. As opposed to the pitch regulated TST, the controller not only has to restrict the bandwidth below the frequencies of the RHPZs, but also stabilize the plant. The complex RHPZs and LHPZs of $n_{12}(s)$ and LHPPs of $d_{12}(s)$ occur at high frequencies and are weakly damped. These characteristics are reflected in resonant and inverted resonant peaks in the magnitude plot and sudden change of phase in the phase plot (Figure 5.16(a)). The losses in phase are greater than was the case for the pitch regulated TST due to the additional RHPZs.

It is important to highlight that when the turbine enters into deep stall, at V_{flow}= 3.1m/s, the dynamics of the turbine change and the frequency of the RHPP (p_{12}) becomes greater than that of the LHPP pole (10 rad/s). As a result of this two controllers were designed: one for operation between the rated flow speed up to 3.0 m/s and an additional one for flow speeds above 3.0 m/s. The bandwidth was restricted by at least a decade below 10^4 rad/s. Appropriate designs for each controller are given as follows:

$$k_{st1}(s) = k_{s1} \cdot \frac{(s + 0.25)}{s} \cdot \frac{(s + 7)}{(s + 60)} \tag{5.11}$$

$$k_{st2}(s) = k_{s2} \cdot \frac{(s + 4.25)}{s} \cdot \frac{(s + 4.5)}{(s + 120)} \tag{5.12}$$

The controller described by (5.11) is active above rated flow speeds up to 3.0m/s, switching to (5.12) for flow speeds greater than 3.0m/s. The structure of both (5.11) and (5.12) consists of a PI cascaded with a lead term that improves stability margins. The gains k_{s1} and k_{s2} are adjusted as a function of flow speed to achieve a similar bandwidth for all flow speeds over which (5.11) and (5.12) are active. The gains are given in Appendix D.7. For the work in this thesis it was assumed that a flow speed measurement was available for the purposes of scheduling the controllers.

It is acknowledged that there are practical difficulties with obtaining an accurate measurement of flow speed. Point measurements are not accurate because the flow will vary both spatially and temporally over the swept area of the rotor. However, numerous methods for estimating flow speed from measureable variables of the turbine have been proposed (Ekelund, 1997; Bourlis & Bleijs, 2010) and have proven effective. Thus using flow speed as a gain scheduling variable is viable and could practically be achieved.

The Bode plots of $K_{st1}.g_{12}(s)$ and $K_{st2}.g_{12}(s)$ are shown in Figure 5.18. It can be seen that the bandwidth for the conditions before deep stall is between 24–36 rad/s, and between 60-80 rad/s after the TST enters into deep stall. The control design has good stability margins (before deep stall: $M_{ph} > 65$ deg; $M_g \approx 100$ dB; after deep stall: $M_{ph} > 45$ deg; $M_g \approx 80$ dB). The step response of the plants is shown in Figure. 5.19. It can be seen that the performance worsens when the turbine enters into deep stall (*i.e.*, for flow speeds above 3.0m/s) as shown in Figure.5.19 (b). The performance could be improved by using a more complex control structure, but designing and implementing such a controller would be more challenging and the simplicity offered by (5.11) and (5.12) would be lost.

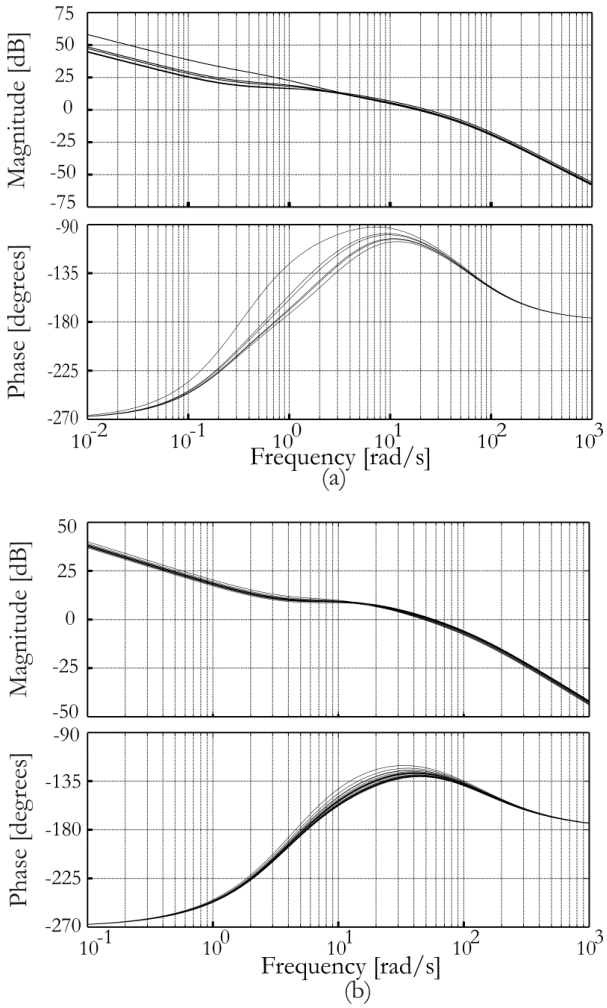

Figure 5.18: Bode plot for frequencies below 10^3 rad/s: (a) before deep stall (b) after deep stall.

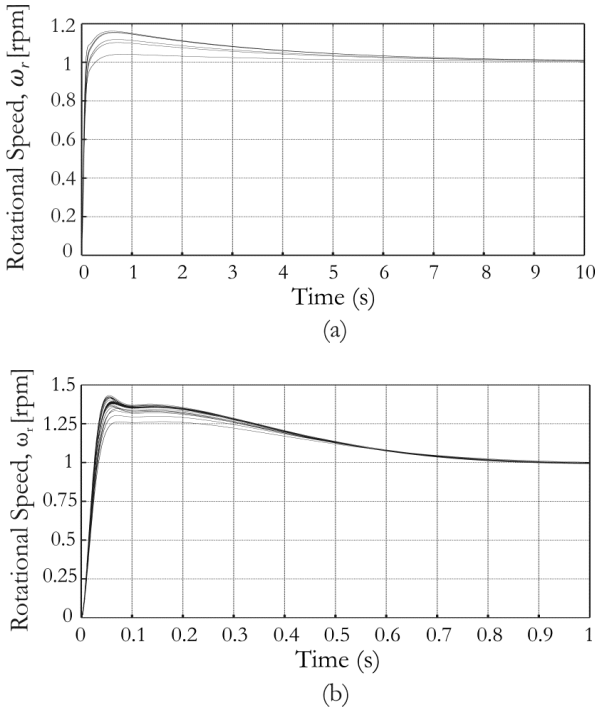

Figure 5.19: Performance of the stall control loop: step response (a) before deep stall; (b) after deep stall.

5.1.5 Dynamic Performance and Loading Analysis

To test the performance of the controllers' simulations were run in GH Tidal Bladed® under time varying environmental conditions. To do this the controllers were first converted from the continuous to the discrete domain using the zero-order-hold method with a sampling time of 2 kHz (The MathWorks Inc, 2010). Once the equivalent discrete versions of the transfer functions had been obtained the difference equations were determined (Dorf & Bishop, 2008) and then coded in C++. The C++ scripts were then compiled as a dynamic link library (DLL). The DLL is then able to communicate with the simulation as detailed by Garrad Hassan & Partners Ltd (2009). As would be the case with a real controller the external controller runs on a discrete time-step. The choice of sampling rate is based on the closed loop bandwidth of the system, with reasonable sampling rates being 10 to 30 times the bandwidth (Gopal, 2009). To ensure that this was the case a time step of 0.0005s (2 kHz rate) was used.

To verify the performance of the controllers at flow speeds close to rated and at higher flow speeds two simulations, 1 and 2, were run using different flow velocities for each. Time histories of the hub height flow velocities used in each simulation are shown in Figure 5.20. The flow regimes were generated by defining mean flow speeds of 2.6 and 3.8m/s respectively and imposing turbulence intensities on each of 5% using the von Karman spectral model. Tower shadow effects and structural dynamics of the blades were included (Garrad Hassan & Partners Ltd, 2009); those of the support structure were not.

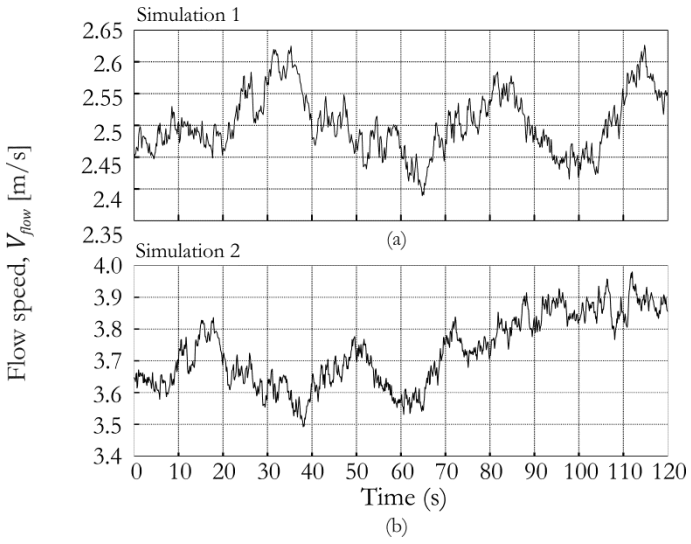

Figure 5.20: Hub height flow velocities (V_{flow}) for simulations 1 and 2: (a) Mean flow speed 2.6m/s + longitudinal turbulence intensity of 5%, (b) Mean flow speed 3.8m/s + longitudinal turbulence intensity of 5%.

Figure 5.21(a) shows the rotational speeds for the variable speed pitch and assisted stall regulated TSTs for simulation 1. As expected the rotor speed of the pitch regulated machine is regulated at rated speed (13RPM) and as a result the output power, shown in Figure 5.21(b), is also regulated at the rated value of 1000kW. For the stall regulated TST the rotor speed varies as the reference speed (Ω_{Ref}) from Figure 5.15 is tracked. The resulting output power is shown in figure 5.21(b).

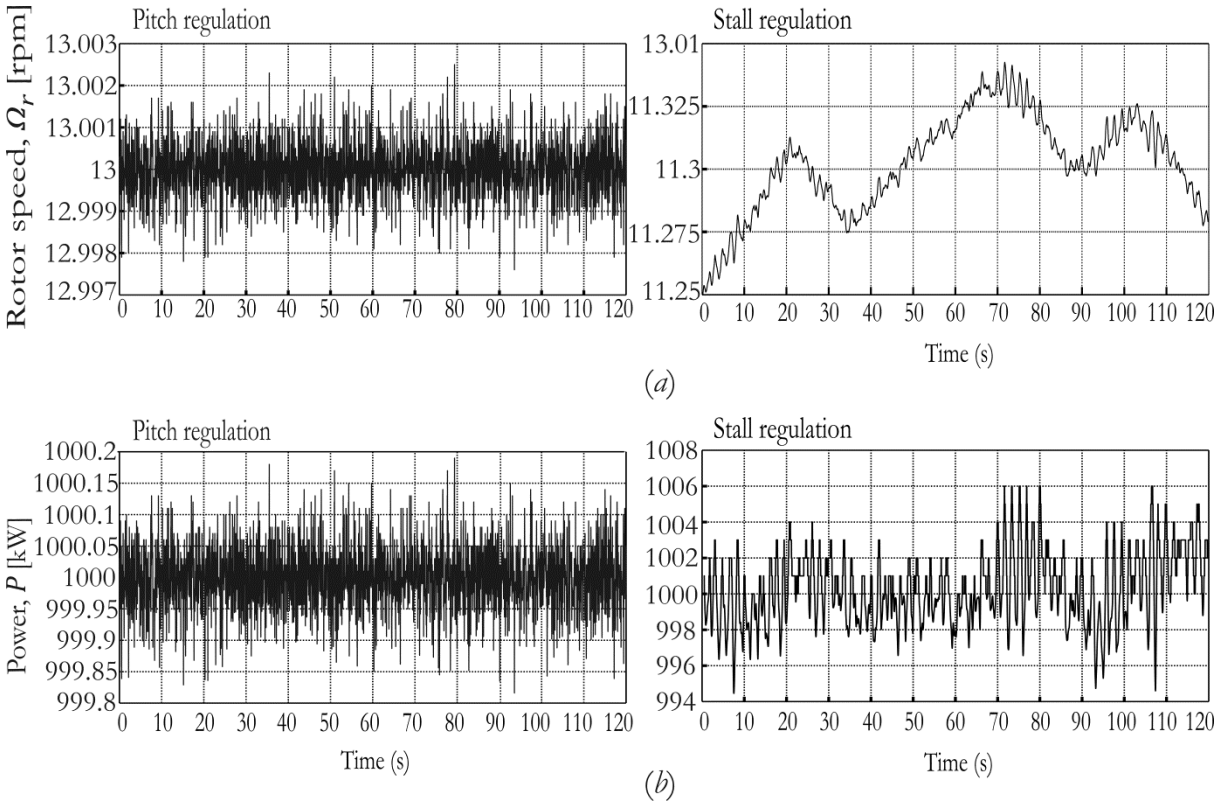

Figure 5.21: Performance of pitch and stall regulated TSTs simulation (1): (a) Rotor speeds (Ω_r), (b) Output Power (P).

The results of simulation 2, where the mean flow speed was increased from 2.6m/s to 3.8m/s are shown in Figure 5.22. Once again the rotor speed of the pitch regulated machine is regulated at rated speed (13RPM), as shown in Figure 5.22(a), and as a result the output power, shown in figure 5.22(b), is also regulated at the rated value of 1000kW. The stall regulated turbine tracks the speed reference (Ω_{Ref}), as shown in Figure 5.22(a) and the resulting output power is shown in Figure 5.22(b).

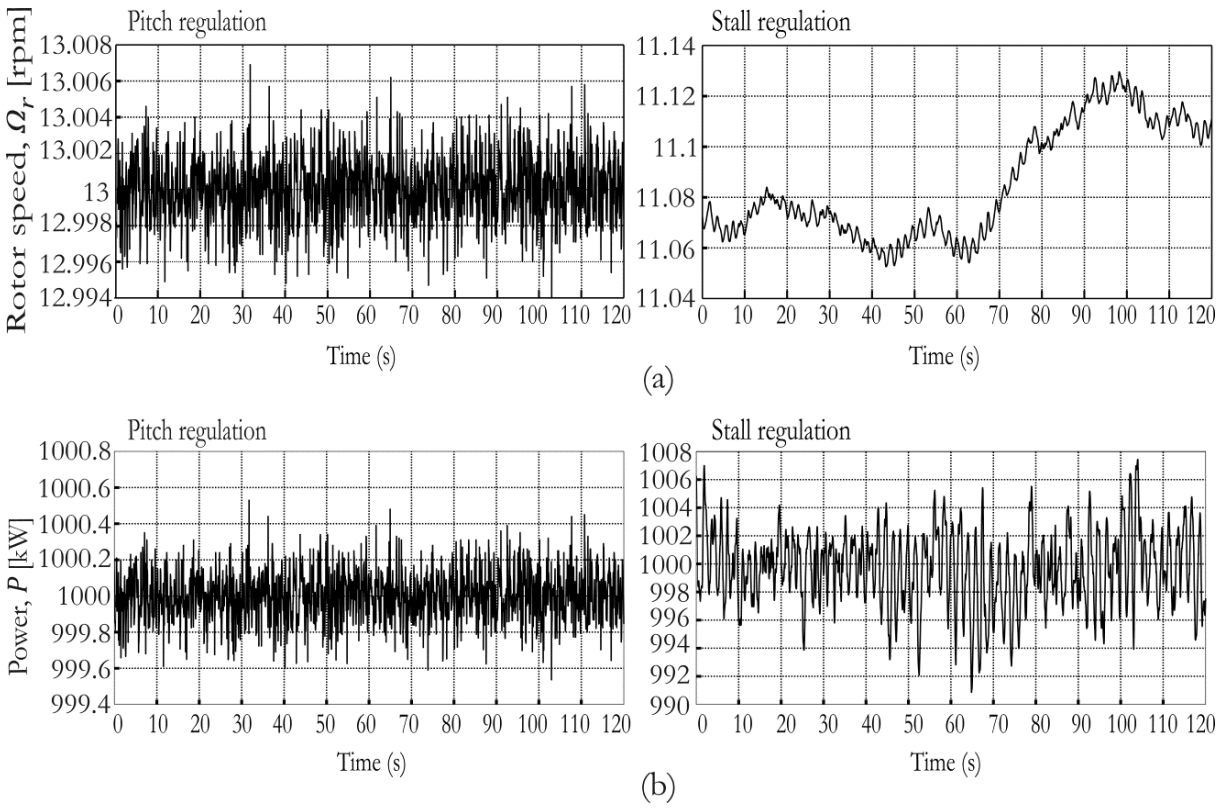

Figure 5.22: Performance of pitch and stall regulated TSTs simulation (2): (a) Rotor speeds (Ω_r), (b) Output Power (P).

In both simulation 1 and simulation 2 it is evident that the power regulation of the pitch regulated TST is superior to that of the stall regulated TST in both cases. It can also be seen that the power regulation of both the pitch and stall regulated TSTs does vary slightly between simulation 1 and simulation 2, which is due to the nonlinearities of the TST as it moves from one operating point to another.

The hydrodynamic thrust force (F_T), out-of-plane blade root bending moment (M_y) and in-plane blade root bending moment (M_x) are compared in Figure 5.23. These forces were obtained by running a simulation in GH Tidal Bladed® using the flow profile of Figure 5.20(a). Once again tower shadow effects and structural dynamics of the blades were included; those of the support structure were not.

It can be seen from Figure 5.23(a) that F_T is higher for the stall regulated turbine. This is due to the twist distribution of the stall regulated blade. M_y dominates in both cases, being higher for the stall regulated TST. In contrast, M_x is significantly lower for both turbines –although of a similar magnitude. These results confirm that the out-of-plane bending forces are dominant and higher for the assisted stall regulated TST.

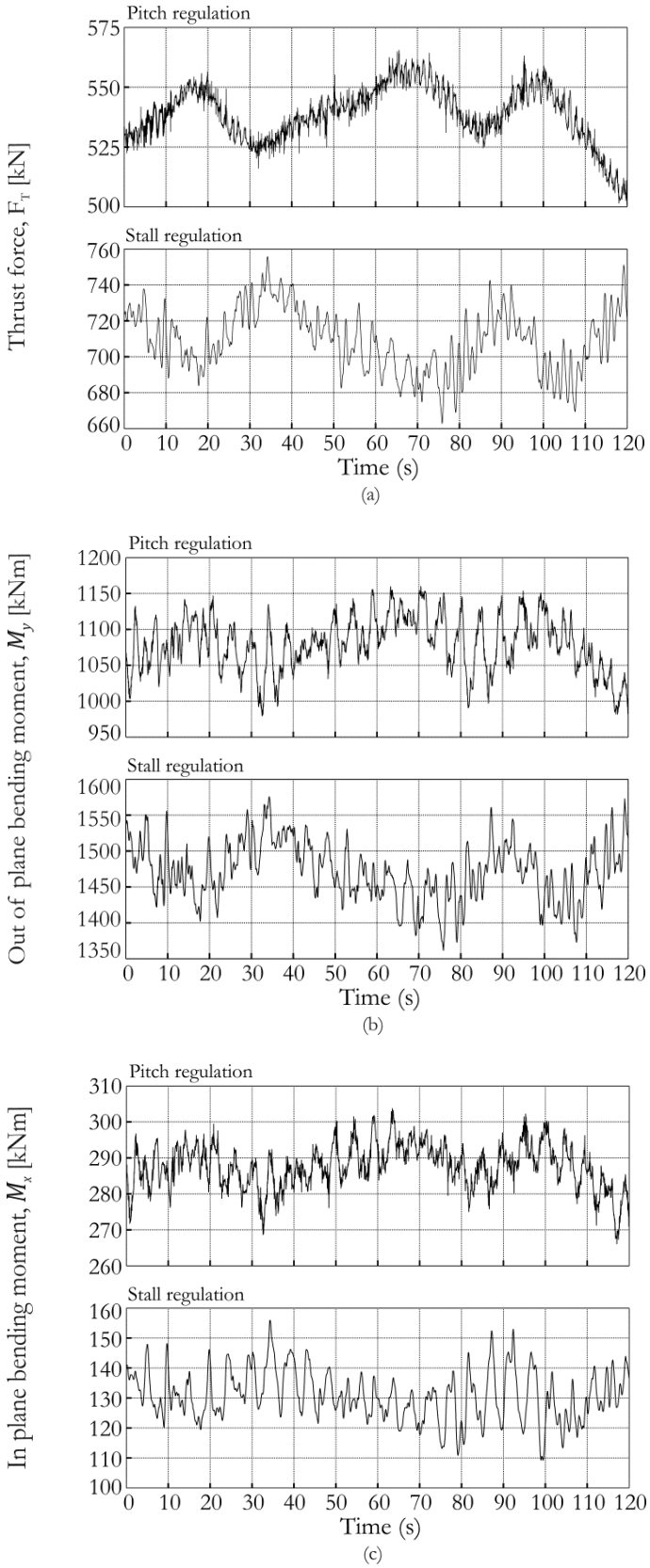

Figure 5.23: Thrust and bending moments for pitch and stall regulated TSTs: (a) Rotor thrust force (F_T), (b) Out-of-plane blade root bending moment (M_y), (c) In-plane blade root bending moment M_x.

5.1.6 Annual Energy Yield Analysis

The annual energy yield is calculated using the dynamic power curves shown in Figure 5.24. These power curves were produced by running dynamic simulations at a number of discrete flow speeds between the cut-in (V_{min}) and cut-out (V_{max}) flow speeds of each turbine. In between these discrete points a linear variation is assumed. The effects of the controller performance as well as the dynamics of the turbine are reflected in these power curves.

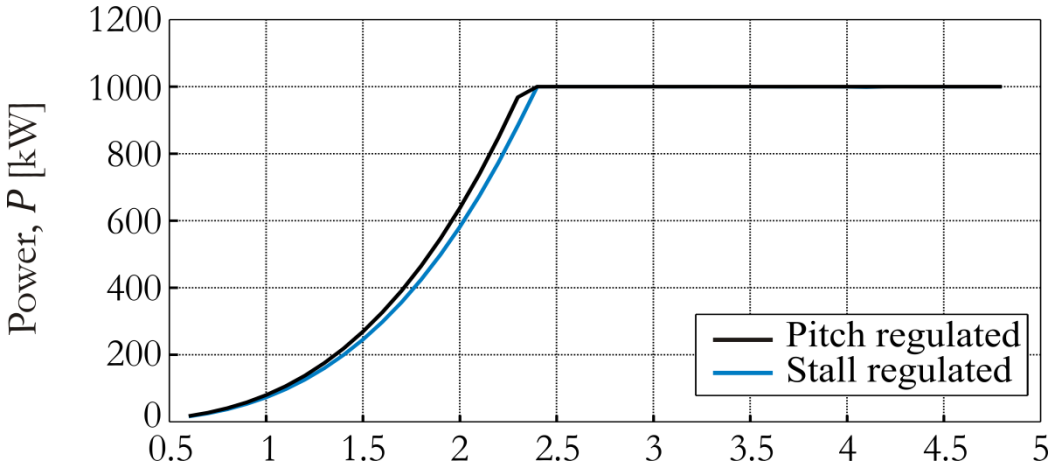

Figure 5.24: Dynamic power curves

The annual energy yield (E) is then calculated as follows (Bossanyi, 2009):

$$\mathrm{E} = Y \int_{V_{max}}^{V_{min}} P(V) f(V) dV \tag{5.13}$$

$P(V)$ is the dynamic power curve, Y is the length of a year (taken as 365 days) and $f(V)$ is the flow speed probability. In this case the distribution of flow speeds is defined by a Weibull curve (Bossanyi, 2009). A 100% availability of the TSTs was assumed when carrying out the calculations resulting in values of 5.299 GWh p.a. and 5.436 GWh p.a. for the variable-speed assisted stall regulated and pitch regulated TSTs respectively. The superior performance of the pitch regulated TST is mainly due to the better performance of the pitch controller and a more efficient blade design, which means that it operates at a higher C_P value below rated.

5.2 Conclusion

A performance comparison and control system design has been carried out for a stall and pitch regulated horizontal axial flow, variable-speed TST. By using the linearisation module in GH Tidal Bladed® analysis of the model dynamics was undertaken. Below rated flow speed the dynamics of both TST models were found to be stable. However, it has been shown that above rated the dynamics are significantly different: the pitch regulated TST is stable, whilst the stall regulated TST has unstable dynamics. Both turbines feature RHPZs. Controlling the stall regulated TST is more onerous as the controller has to stabilize the plant while restricting the bandwidth below the frequencies of the RHPZs.

Controllers have been designed and implemented for both TST models, providing a satisfactory performance when tested in GH Tidal Bladed®. Although the controller structure was kept as simple as possible to make implementation easier, the designs ensured good stability margins. The performance for the case of the stall regulated TST could be improved through a more complex controller. It is clear from the simulation results that the power regulation of the pitch regulated TST was superior.

Analyses of the loads show the out-of-plane bending moments dominate and are higher for the stall regulated TST over the entire operating range of the turbine. In fact, they are significantly higher when the turbine goes into deep stall. This is because the axial trust force is higher which results from the fact that the blades have been designed to operate at a higher angle of attack, near to the maximum lift coefficient. This ensures that the blade will stall at the desired above rated point.

The energy yield of the pitch regulated TST was higher than that of the stall regulated turbine. This is largely because the pitch regulated turbine, in this case, is more efficient below rated; however, the superior performance of the pitch controller also has an effect. It should be noted that 100% availability of the turbines was assumed when carrying out this calculation. In reality this will not be the case and one could argue that the increased complexity of the pitch machine (which requires pitch bearings, hydraulic actuators and position sensors) will mean more maintenance and increased downtime.

Chapter 6

6. Conclusions and Further Work

Summary:

This chapter summarises the conclusions resulting from the research that has been carried out and highlights the key contributions that have been made.

6.1 Conclusions

Tidal stream turbines have the ability to generate large amounts of electricity from a renewable resource that is indigenous, non-polluting and highly predictable. Despite the potential only a handful of prototype devices have been deployed and the industry is still in its infancy. A number of challenges will need to be overcome before the industry is able to move from single prototype installations to commercial scale multi-device arrays capable of generating meaningful amounts of electricity.

Two of the main challenges identified in the research are the need to reduce cost (to make tidal stream technologies competitive with other forms of renewable energy generation) and the need to establish an optimal design solution that will allow a certain amount of convergence to take place. To date a large number of developers, with vastly different designs, have entered the industry and the lack of convergence on a particular design philosophy is hampering progress. It was with these challenges in mind that the work in this thesis was carried out.

A low solidity horizontal axial flow rotor was proposed. This design offers an optimal solution that has been widely used in the wind industry and is the design that a large number tidal stream developers are adopting.

A comparison of different drive-train and power take-off options, suitable for use with an axial flow rotor of this sort, was undertaken. Operation and maintenance was highlighted by the Carbon Trust (Carbon Trust, 2011) as an area with high potential for cost reduction and this was taken into account when selecting a design. It was concluded that use of a multi-pole PMSG in a direct-drive configuration connected to the grid through a full-power converter, consisting of back-to-back VSCs, offered the most attractive solution. With the gearless construction, permanent magnet excitation and variable speed control the system represents an efficient and low maintenance solution. Such a design will reduce the operation and maintenance element of the lifetime cost and should therefore reduce the cost per kWh of the turbine.

The research was separated into two main areas: control of the turbine in below rated flow speeds where the objective was to maximise energy capture, and control of the turbine in high flow speeds where the aim was to regulate power, shed load and ensure the survivability of the turbine.

6.1.1 Control of Tidal Stream Turbines below Rated Flow Speed

A control scheme was developed to maximise the power output of a tidal stream turbine (TST) in below rated flow speeds by allowing the rotor speed to be varied. This was achieved by using the generator reaction torque. A lookup table was used to set the generator torque demand based on the rotational speed. This caused the rotor to track a torque vs. speed trajectory that maximised the output power.

The generator control was implemented in the d, q reference frame using a maximum torque per ampere strategy. The aim of this strategy is to keep the ratio between the stator current and the electromagnetic torque as small as possible. This leads to optimal utilisation of the generator and minimises losses, because the generator stator current is used solely for torque production.

A vector control scheme was applied to the grid-side converter that allows the flow of active and reactive power to be controlled.

The performance of the system was verified in simulation. When subjected to a step change in flow speed the generator-side controller controlled the generator torque for maximum power extraction while the grid-side converter regulated the DC link voltage, thereby controlling the flow of active power to the grid, as well as controlling the flow of reactive power.

The same control strategy was implemented on a hardware in the loop test rig. The rig consisted of two back-to-back VSCs connected to the grid through an auto-transformer. Two AC brushless servo machines joined by a flexible coupling were used to emulate the turbine rotor and generator. The control strategy was implemented in real-time on a dSPACE® unit containing a high speed digital signal processor. The experiment was carried out to assess how the controller would perform with the dynamics of a real back-to-back converter and generator in the loop. Experimental results showed that the system behaved appropriately and achieved the desired objective of maintaining the turbine at its maximum power coefficient.

This work provides evidence that operating the turbine in variable speed mode, using the control strategy detailed in this thesis, will increase the energy yield of the turbine by allowing it to operate at its maximum power coefficient over a wide range of flow speeds.

6.1.2 Control of Tidal Stream Turbines above Rated Flow Speed

A comparison was carried out between a variable speed pitch regulated turbine where the rotor blades are pitched to feather and a variable speed turbine using speed-assisted stall. Models of each TST were developed and simulated using the commercially available software GH Tidal Bladed®. The dynamic characteristics of each model under both types of regulation were examined and control system design was done in MATLAB.

The findings revealed by the studies are listed below.

- Below rated flow speed the dynamics of both TST models are stable. However, above rated flow speed the dynamics are significantly different: the pitch regulated TST is stable, whilst the stall regulated TST becomes unstable as the flow speed increases and the rotor begins to stall. This meant that design of the stall regulated controller was more onerous as the controller had to stabilise the plant.
- The out-of-plane bending moments were the dominant load for both turbines, and they were higher for the stall regulated TST over the entire operating range of the turbine. In fact, they were significantly higher when the turbine went into deep stall.
- The main driver for the out-of-plane bending moment is the axial thrust force, which is higher for the stall regulated TST over the entire operating range of the turbine and increases significantly when the turbine goes into deep stall.
- The energy yield for the pitch regulated turbine was higher. This was attributed to the superior performance of the pitch controller and to the fact that the pitch regulated turbine was more efficient below rated flow speed. The need to make the stall regulated turbine stall at a particular flow speed meant that the blade design was further from the optimal than that of the pitch regulated turbine; hence, it was less efficient.

It is concluded that designing a TST capable of operating at the maximum flow speed seen at a site will not be economic as it will operate at less than 100% capacity for much of the time and will be over-specified for average operating conditions. Specifying a rated flow speed, at which the turbine produces its peak power, and shedding power at flow speeds in excess of the rated value will increase the capacity factor of the turbine and reduce the cost per kWh of electricity generated.

Designers looking to choose between the pitch and stall regulation methods will need to be aware of the higher out-of-plane loads generated by the stall regulated TST, especially in high

flow speeds where the axial thrust force will increase unchecked as the flow speed increases. This, together with the increased complexity of the controller would suggest that the fixed pitch assisted stall regulated turbine will need to be much cheaper in order to compete with pitch regulated TSTs on a lifetime cost basis. However, this conclusion assumes that the availability of both TSTs is comparable, which is something that will require further investigation.

6.2 Summary of Contributions

The objectives listed below were set and achieved.

- A field oriented control method was developed to maximise energy extraction in below rated flow speeds (Chapter 2).
- A hardware in the loop turbine test rig was constructed (Chapter 3) – This allowed hardware-in the loop simulation and evaluation of the below rated controller to be carried out.
- Two hydroelastic turbine models were developed in GH Tidal Bladed® (Chapter 4). One of the turbines has variable pitch blades, which above rated speed are pitched to feather in order to regulate power. The other turbine has fixed pitch blades and uses assisted stall to regulate power.
- A comprehensive analysis of the dynamic characteristics of both the assisted stall and pitch regulated turbines was undertaken, with control system design being carried out in MATLAB (Chapter 5).
- A comparative analysis of the two turbine models in terms of performance under turbulent flows, loading and energy yield was carried out using GH Tidal Bladed® (Chapter 5).

6.3 Further Work

6.3.1 Variable Speed Control

The field oriented control strategy, applied to the generator-side converter to allow variable speed operation, requires measurements of the generator rotor position and speed, which were obtained using an encoder mounted on the rotor. The use of such a sensor will increase cost and may lead to reduced reliability, particularly in light of the harsh environment in which these devices will operate. Furthermore, in cases where the generator is flooded the use of an encoder may not be possible. Implementing a sensorless control technique, able to estimate the rotor position and speed used by the field oriented control strategy would be an improvement.

6.3.2 Stall Regulated Tidal Stream Turbine Control

The above rated control strategy for the stall regulated turbine, proposed in Chapter 5, assumed that a measurement of the turbines low speed shaft torque (τ_m) was available. Furthermore, the flow speed (V_{flow}) was used as a gain scheduling variable to tailor the controller to the changes in the dynamics of the turbine as the operating point changed. It is acknowledged that obtaining accurate measurements of τ_m and V_{flow} may be problematic. Implementation of an observer would allow the hydrodynamic torque and flow speed to be estimated from measureable variables of the turbine. Using observers for this purpose has been described in the literature.

6.3.3 Comparison of Pitch and Stall Regulated Tidal Stream Turbines

In Chapter 5 the performance of a pitch and a stall regulated TST were compared. When carrying out a comparison of the energy yields 100% availability of the TSTs was assumed. Making this assumption the energy yield from the pitch regulated turbine was higher than that of the stall leading to the conclusion that the stall regulated turbine will need to be much cheaper in order to compete with pitch regulated TSTs on a lifetime cost basis. However, in reality both turbines are likely to experience downtime. The increased complexity of the pitch regulated turbine suggests that downtime may be higher for this type of turbine. Further investigation into the amount of downtime that each TST is likely to experience, and the impact of downtime on the energy yields would be a very useful addition to this work.

7. References

Anaya Lara O., Jenkins N., Ekanayake J., Cartwright P. & Hughes M. 2009, '*Wind Energy Generation: Modelling and Control',* John Wiley and Sons Ltd., Chichester

Bahaj A.S. 2013, 'Marine current energy conversion: the dawn of a new era in electricity production', Phil Trans R Soc A 371: 20120500. http://dx.doi.org/10.1098/rsta.2012.0500

Bahaj A.S. 2011, 'Generating energy from the oceans', *Elsevier Renewable and Sustainable Energy Reviews,* vol.15, issue 7, p.p.3399-3416

Bang D., Polinder H., Shrestha G. & Fereira J.A. 2008, 'Review of generator systems for direct-drive wind turbines', Paper presented at the European Wind Energy Conference (EWEC), Brussels, Belgium, March-April 2008

Bard J., Schmid J., Caselitz P., Giebhardt J. 2005, 'Electrical Engineering Aspects of Ocean Energy Converters', Paper presented at the 6th European Wave and Tidal Energy Conference, Glasgow, Scotland, 30th August – 2nd September

Batten W.M.J., Bahaj A.S., Molland A.F. & Chaplin J.R. 2007, 'The prediction of the hydrodynamic performance of marine current turbines', *Elsevier Renewable Energy*, vol.33, p.p. 1085-1096

Bianchi F.D., De Battista H. & Mantz R.J. 2010, '*Wind Turbine Control Systems: Principles, Modelling and Gain Scheduling design',* Germany: Springer

Bir G. S., Lawson M. J. & Li Y. 2011, 'Structural Design of a Horizontal-Axis Tidal Current Turbine Composite Blade', presented ASME 30th International Conference on Ocean Offshore Arctic Engineering, The Netherlands, 19th – 24th June

Blaabjerg F., Teodorescu R., Liserre M. & Timbus A.V. 2006, 'Overview of Control and Grid Synchronization for Distributed Power Generation Systems', *IEEE Transactions on Power Electronics,* vol. 53, no.5, pp. 1398-1409

Black and Veatch Ltd, 2011, UK Tidal Current Resource and Economics, report prepared for the Carbon Trust, Carbon Trust, London

Boldea I. 2006, *'Synchronous Generators',* Taylor and Francis, Florida, United States

Bornens P., Daviau J., Gaillard L., Guerrier A. & Ruer J. 2010, 'The Sabella Tidal Turbine – Test Results and further development', paper presented at the international conference on ocean energy, Bilbao, Spain, 6-8 October

Boukhezzar B. & Siguerdidjane H. 2005, 'Nonlinear control of variable speed wind turbines for power regulation', *In Proceedings of 2005 IEEE Conf. Control Applications (CCA)* Toronto, Canada, pp. 114-119

Bourlis D. & Bleijs J.A.M. 2010, 'Control of stall regulated variable speed wind turbine based on wind speed estimation using an adaptive Kalman filter', in proceedings of the *European. Wind Energy Conference (EWEC)*, Warsaw, Poland, pp. 4699-4710

Bossanyi E.A. 2009, '*GH Tidal Bladed Theory Manual',* Garrad Hassan and Partners, Bristol

Bossanyi E.A. 2003, 'Wind Turbine Control for Load Reduction', *Wind Energy* vol.6, issue 3, pp. 229-244

Bryden G.I. 2004, 'Tidal Energy', In: Encyclopaedia of energy, Vol.6, pp. 132-150, Elsevier, New York

Brahmi J., Krichen L. & Ouali A. 2009, 'A comparative study between three sensorless control strategies for PMSG in wind energy conversion system', *Elsevier Applied Energy*, vol. 86, pp 1565-1573

Burton T., Sharpe D., Jenkins N. & Bossanyi E. 2001, '*Wind Energy Handbook',* Chichester: John Wiley and Sons

Carbon Trust, 2011, Accelerating Marine Energy, Carbon Trust, London

Chinchilla M., Arnaltes S. & Burgos J.C. 2006, 'Control of Permanent Magnet Generators Applied to Variable-Speed Wind-Energy Systems Connected to the Grid', *IEEE Transactions on Energy Conversion,* vol. 21, No.1, pp. 130-135

Clarke J.A., Connor G., Grant A.D., Jonstone C.M. 2006, 'Regulating the output characteristics of tidal current power stations to facilitate better base load matching over the lunar cycle', *Elsevier Renewable Energy,* vol. 31, pp. 173-180

Corten G.P., Veldkamp H.F. 2001, 'Insects can Halve Wind Power', Nature, Vol 412, pp.41-42

Department of Energy and Climate Change (DECC), 2011a, 'UK Renewable Energy Roadmap, Crown', London

Department of Energy and Climate Change (DECC), 2011b, 'Planning our electric future: a White Paper for secure, affordable and low-carbon electricity', The Stationary Office, London

Department of Energy and Climate Change (DECC), 2012, 'Government response to the consultation on proposals for the levels of banded support under the Renewables Obligation for the period 2013-17 and the Renewables Obligation Order 2012', Crown, London

Dorf R.C. & Bishop R.H. 2008, '*Modern Control Systems'*, New York: Pearson Education

Douglas C.A., Harrison G.P & Chick J.P. 2008, 'Life cycle assessment of the Seagen marine current turbine', *Proceedings of the Institution of Mechanical Engineers Part M Journal of Engineering for the Maritime Environment,* vol.222

Doyle F., Francis B. & Tannenbaum A. 1990, "*Feedback Control Theory*," New York: Macmillan publishing Co.

Drela M. 1989, 'XFoil: an analysis and design system for low Reynolds number airfoils', paper presented at the Conference on Low Reynolds Number Airfoil Aerodynamics, University of Notre Dame, Indiana

Ekelund T. 1997, '*Modeling and linear quadratic optimal control of wind turbines*.' Ph.D. thesis, Chalmers University of Technology, Gothemborg, Sweden

Ekelund T. 1994,"Speed control of wind turbines in the stall region," *In Proceedings of the 3rd IEEE Conference on Control Applications (CCA)*, Glasgow, U.K., pp. 227-232

Eldridge F.R. 1980, '*Wind Machines'* (2nd Edition), Van Nostrand Reinhold Company, New York

Florin I., Daniela Hansen A., Sorensen P. & Blaabjerg F. 2004, '*Wind Turbine Blockset in Matlab Simulink. General overview and description of the models'* [pdf]*,* Aalborg: Aalborg University. Available at: http://vbn.aau.dk/en/publications/wind-turbine-blockset-in-matlabsimulink-general-overview-and-description-of-the-model(7dae90f0-0035-11da-b4d5-000ea68e967b)/export.html

Fraenkel P.L. 2010a, 'Development and Testing of Marine Current Turbines's SeaGen 1.2MW tidal stream turbine', paper presented at the international conference on ocean energy, Bilbao, Spain, 6th-8th October

Fraenkel P.L. 2010b, 'Practical tidal turbine design considerations: a review of technical alternatives and key design decisions leading to the development of the SeaGen 1.2MW tidal turbine' paper presented at the Ocean Power Fluid Machinery Seminar, Institution of Mechanical Engineers London, 19th October 2010

Fraenkel P.L 2007, 'Marine current turbines: pioneering the development of marine kinetic energy converters', *Proceedings of the Institution of Mechanical Engineers Part A Journal of Power and Energy,* vol. 221

Fraenkel P. L. 2002, 'Power from marine currents', *Proc. Inst. Mech. Eng., Part A: Journal of Power and Energy,* vol. 216, pp. 1-14

Franc J.P & Michel J.M. 2005, *'Fundamentals of Cavitation'*, [e-book], Netherlands: Springer. Available through: http://www.springer.com/physics/classical+continuum+physics/book/978-1-4020-2232-6, [Accessed April 10th 2013]

Garrad Hassan & Partners Ltd, 2010, *'Training Course Manual: Introduction to Wave and Tidal Energy Conversion'*, Garrad Hassan and Partners, Bristol

Garrad Hassan & Partners Ltd, 2009, *'GH Tidal Bladed User Manual'*, Garrad Hassan & Partners Ltd., 2009

Gopal M. 2009, *'Digital Control and State Variable Methods'*, New Delhi: Tata McGraw-Hill publishing company

Gupta R., Biswas A. & Sharma K.K. 2008, 'Comparative study of a three-bucket Savonius rotor with a combined three-bucket Savonius-three-bladed Darrieus rotor' *Elsevier Renewable Energy,* vol.33, issue 9, p.p.1974-1981

GCK Technology 2013, viewed on 18th February 2013, http://www.gcktechnology.com/GCK/pg2.html

Hahn B., Durstewitz M. & Rohrig K. 2007, '*Reliability of Wind Turbines, Experience of 15 years with 1,500 WTs'*, in Wind Energy, Proceedings of the Euromech Colloquium, Springer, Berlin

Hardisty J. 2008, 'Power intermittency, redundancy and tidal phasing around the United Kingdom', *The Geographical Journal,* vol.174, no.1, pp.76-84

Hardisty J. 2009, '*The Analysis of Tidal Stream Power*' (1st Ed.), Chichester: John Wiley & Sons Ltd.

Hassan H. F., Karim O. A. & El-Shafie A. 2012, 'Tidal current turbines glance at the past and look into future prospects in Malaysia', *Elsevier Renewable and Sustainable Energy Reviews,* vol.15, p.p.5707-5717

Hau E. 2006, '*Wind Turbines, Fundamentals, Technologies, Application, Economics',* [2nd Ed.], Berlin: Springer

Heir S. 2006, '*Grid Integration of Wind Energy Conversion Systems'* (2nd Ed.), John Wiley and Sons Ltd., Chichester

Huang K., Huang S., She F., Luo B. & Cai L. 2008, 'A control strategy for direct-drive permanent-magnet wind-power generator using back-to-back PWM converter', *In the proceedings of the International Conference on Electrical Machines and Systems(ICEMS*), Wuhan, China 17th-20th October

Krishnan R. 2010, '*Permanent Magnet Synchronous and Brushless DC Motor Drives',* Taylor and Francis, Florida, United States

Kundur P. 1994, *'Power System Stability and Control'* United States: McGraw-Hill

Leithead W. E. & Connor B. 2000, 'Control of variable speed wind turbines: Dynamic models', *International Journal of Control,* vol. 73, pp. 1173-1188

Linke M., Kennel R. & Holtz J. 2002, 'Sensorless position control of permanent magnet synchronous machines without limitation at zero speed', *In the proceedings of the IEEE Industrial Electronics Society Conference (IECON),* Seville, Spain 5th-8th November.

Liserre M., Blaabjerg F. & Aquila A. D. 2007, 'Step-by-step design procedure for a grid-connected three-phase PWM voltage source converter', *International Journal of Electronics,* vol. 91, no. 8, pp.445-460

Manwell J.F., McGowan J.G. & Rogers A.L. 2002, '*Wind Energy Explained: Theory, Design and Application*' (1st Ed.). Chichester: John Wiley & Sons Ltd

Marsh G. 2004, 'Tidal Turbines Harness the Power of the Sea', *Reinforced Plastics,* vol.48, no.6, pp.44-47

McCann G., Thomson M. & Hitchcock S. 2008, 'Implications of Site-Specific Conditions on the Prediction of Loading and Power Performance of a Tidal Stream Device', paper presented at the international conference on ocean energy, Brest, 15th-17th October

Michalke G. & Hansen A.D. 2009, 'Multi-pole permanent magnet synchronous generator wind turbines' grid support capability in uninterrupted operation during grid faults', *IET Renewable Power Generation,* vol. 3, pp.333-348

Milne I.A., Sharma R.N., Flay R.G.J. & Bickerton S. 2010, 'The role of onset turbulence on tidal turbine blade loads', paper presented at the 17th Australasian Fluid Mechanics conference, Auckland, 5th -9th December.

Mohan N., Undeland T. M. & Robbins W.P. 2002, *'Power Electronics: Converters, Applications and Design'* (3rd Ed.), New Jersey: John Wiley & Sons

Muljadi E., Singh M. & Gevorgian V. 2012, 'Doubly Fed Induction Generator in an Offshore Wind Power Plant Operated at Rated V/Hz', paper presented at IEEE Energy Conversion Congress and Exhibition, Raleigh, United States, 15th – 20th September

Nise N.S. 2004, *'Control Systems Engineering'* (4th Ed.), New Jersey: John Wiley & Sons

OFGEM, 2013, 'Renewables Obligation: Guidance for licensed electricity suppliers', OFGEM, London.

OFGEM, 2011, '*Renewables Obligation* [online]*'*, viewed on 31st July 2013, http://www.ofgem.gov.uk/Sustainability/Environment/RenewablObl/Pages/RenewablObl.aspx

Ocean Renewable Power Company 2013, viewed on 28th February 2013, http://www.orpc.co/default.aspx

Ogata K. 1996, '*Modern Control Engineering'* (3rd Ed.)*,* London: Prentice Hall

O Rourke F., Boyle F. & Reynolds A. 2009, 'Tidal Energy Update 2009', *Elsevier Applied Energy,* vol. 87, pp. 398-409

Pena R., Clare J.C. & Asher G.M. 1996, 'Doubly fed induction generator using back-to-back PWM converters and its application to variable speed wind-energy generation' , *Electric Power Applications, IEE Proceedings-,* vol.143, No. 3, pp. 231-241

Pillay P. & Krishnan R. 1989, 'Modelling, Simulation, and Analysis of Permanent Magnet Motor Drives, Part 1: The Permanent Magnet Synchronous Motor Drive', *IEEE Transactions on Industry Applications,* vol. 25, no. 2, pp. 265-273

Polinder H., van der Pijl F.A., Jan de Vilder G., Tavner P.J. 2006, 'Comparison of Direct-Drive and Geared Generator Concepts for Wind Turbines', *IEEE Transactions on energy conversion*, Vol. 21, No. 3, pp. 725-733

Pulse Tidal, 2013, viewed on 17th February 2013, http://www.pulsegeneration.co.uk/

Royal Haskoning, 2011, '*Seagen Environmental Monitoring Programme Final Report'*, Edinburgh, Haskoning UK Ltd. Available at: http://seageneration.co.uk/files/SeaGen-Environmental-Monitoring-Programme-Final-Report.pdf

Saha, U.K. & Rajkumar, M.J. 2006, 'On the performance analysis of Savonius rotor with twisted blades', *Elsevier Renewable Energy,* vol.31, issue 11, p.p.1776-1788

Schubel P.J. & Crossley R.J., 2012, 'Wind Turbine Blade Design Review', *Wind Engineering* vol.636, No. 4, pp. 365-388

Soter S. & Wegener R. 2007, 'Development of induction machines in wind power technology', Paper presented at the electric machines and drives conference, Turkey, 3rd-5th May

Spooner E. & Williamson A.C. 1996, Direct coupled permanent magnet generators for wind turbine applications', *IEE Proceedings Electric Power Applications,* Vol. 143, No.1 pp.1-8

The MathWorks Inc., 2010, '*Simulink®7 Users Guide'* [pdf], The MathWorks Inc., Massachusetts

Tidal Sails AS 2013, viewed on 17th February 2013, http://www.tidalsails.com/

Twining E., Holmes D. G. 2003, 'Grid Current Regulation of a Three-Phase Voltage Source Inverter with an LCL Input Filter', *IEEE Trans on Power Electronics,* vol. 18, no.3, pp. 888-895

Yates N., Walkington I., Burrows R. & Wolf J. 2013, 'Appraising the extractable tidal energy resource of the UK's western coastal waters', Phil Trans R Soc A 371:20120181. http://dx.doi.org/10.1098/rsta.2012.0181

Welsh Assembly Government, 2010, 'A low carbon revolution: the Welsh assembly government energy policy statement', Crown, Cardiff

Winter A.I. 2011a, 'Differences in fundamental design drivers for wind and tidal turbines', paper presented at Oceans'11 conference, Santander, Spain, 6th- 9th June

Winter A.I. 2011b, 'Speed regulated operation for tidal turbines with fixed pitch rotors', *In Proceedings of the Oceans Conference,* Waikoloa, Hawaii, pp.1-8

Appendix A Parameters

Appendix A 1 Tidal Stream Turbine

Parameter	Turbine Parameters
Rated Power	1 MW
Rated Rotor Speed	13 rpm
Rated Hub Flow Speed	2.4 m/s
TSR Below Rated	5.6
Rotor Diameter	23 m
Blade Length	10.6 m
Blade Mass	640 kg
Hub Mass	3500 kg
Rotor Mass	5420 kg
Rotor Blade Inertia, (J_{blade})	11986 kgm^2
Rotor Inertia, (J_r)	110 688 kgm^2
Transmission	Direct Drive Permanent Magnet
Number of Rotor Blades	3
Rotor Position	Upstream

Appendix A 2 Drive-Train Parameters

Parameter	Value
Shaft stiffness (K_{dt})	2×10^6 Nm/rad
Shaft damping (D_{dt})	3.5×10^5 Nms/rad
Gearbox ratio (N)	1:1

Appendix A 3 1 MW Permanent Magnet Synchronous Generator Parameters

Parameter	Value
Rated Power	1000 kW
Rated Speed	13 rpm
Rated Torque	734753 Nm
Stator Resistance (R_s)	0.00461 Ω
Stator Inductance $(L_{sd} = L_{sq})$	886.48 µH
Pole pairs (n_{pp})	60
Generator Rotor Inertia, (J_g)	86 700 kgm^2
Torque Constant (K_t)	620 Nm/A
Voltage Constant (K_e)	98 V_peak L-L/krpm
Magnetic Flux (Ψ_{pm})	6.9 Vs

Appendix A 4 Voltage Source Converter and Grid Connection Parameters

Parameter	Value
DC Link Capacitor	90 000 µF
Switching Frequency	4 kHz
PWM Sampling Time (T_s)	250 µs
Modulation Index (M_a)	0.8
DC Link Voltage (V_{dc})	1400 V
Grid coupling inductance (L_{grid})	800 µH
Grid coupling resistance (R_{grid})	1.2 mΩ
Grid line to line rms voltage (V_{L-L})	690 V

Appendix B Derivations

Appendix B 1 Derivation of Permanent Magnet Synchronous Generator Model

For this description of the PMSG, a symmetrical 3-phase smooth-air-gap machine with sinusoidally-distributed windings is assumed. Furthermore the generator is assumed to have no saliency $(L_{sd}/L_{sq} = 1)$. The voltage equations of the stator in the instantaneous form can then be expressed as:

$$V_{sa} = R_s i_{sa} + \frac{d}{dt}\Psi_a \tag{7.1}$$

$$V_{sb} = R_s i_{sb} + \frac{d}{dt}\Psi_b \tag{7.2}$$

$$V_{sc} = R_s i_{sc} + \frac{d}{dt}\Psi_c \tag{7.3}$$

Where V_{sa}, V_{sb} and V_{sc} are the instantaneous values of stator voltages, i_{sa}, i_{sb} and i_{sc} are the instantaneous values of stator currents, and Ψ_a, Ψ_b, Ψ_c are instantaneous values of stator flux linkages, in phase sa, sb , and sc.

Due to the large number of equations in the instantaneous form, it is more practical to rewrite the instantaneous equations using two-axis theory. Conversion from a three-phase system to a two-phase system is achieved using the Clarke transformation given as follows (Boldea, 2006)

$$\begin{bmatrix} V_{s\alpha} \\ V_{s\beta} \end{bmatrix} = \frac{2}{3}\begin{bmatrix} 1 & -\cos\left(\frac{\pi}{3}\right) & -\cos\left(\frac{\pi}{3}\right) \\ 0 & \sin\left(\frac{\pi}{3}\right) & -\sin\left(\frac{\pi}{3}\right) \end{bmatrix}\begin{bmatrix} V_{sa} \\ V_{sb} \\ V_{sc} \end{bmatrix} \tag{7.4}$$

This frame is called the stationary reference frame. The scaling factor $2/3$ leads to a non power-invariant transformation. By applying the Clarke transformation the PMSG can be expressed as:

$$V_{s\alpha} = R_s\, i_{s\alpha} + \frac{d}{dt}\Psi_\alpha \tag{7.5}$$

$$V_{s\beta} = R_s\, i_{s\beta} + \frac{d}{dt}\Psi_\beta \tag{7.6}$$

$$\Psi_\alpha = L_{\alpha\alpha} i_{s\alpha} + L_{\alpha\beta} i_{s\beta} + \Psi_{pm} \cos(\theta_e) \tag{7.7}$$

$$\Psi_\beta = L_{\beta\beta} i_{s\beta} + L_{\beta\alpha} i_{s\alpha} + \Psi_{pm} \sin(\theta_e) \tag{7.8}$$

Equations (7.5) and (7.6) give expressions for the stator voltages in the stationary reference frame. $i_{s\alpha}$ and $i_{s\beta}$ are the equivalent stator currents in the stationary reference frame, R_s is the stator resistance and Ψ_α and Ψ_β are the flux linkages in the stationary reference frame. Equations (7.7) and (7.8) give expressions for the flux linkages, Ψ_α and Ψ_β. $L_{\alpha\alpha}$ and $L_{\beta\beta}$ are the self-inductances of the stator, $L_{\alpha\beta}$ and $L_{\beta\alpha}$ are the mutual inductances and θ_e is the electrical rotor position

The representation of the system in the stationary reference frame is given in Figure B.1.0

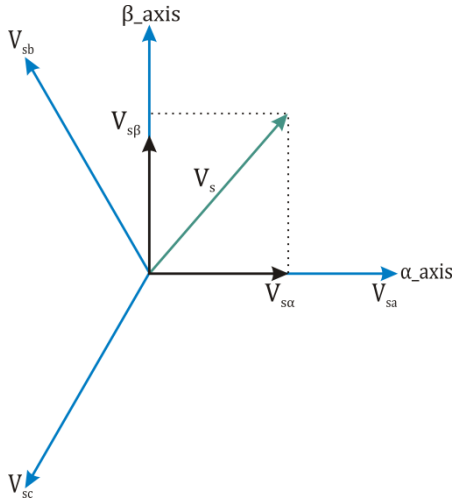

Figure B.1.0: Stator current space vector and it's components in the stationary ($\alpha\beta$) frame. α is aligned with the magnetic axis of phase a and β leads α by 90 degrees. V_{sa}, V_{sb} and V_{sc} are the instantaneous voltages in the stator phases. $V_{s\alpha}$ and $V_{s\beta}$ are the equivalent stator voltages in the stationary reference frame. V_s is the resulting stator voltage vector.

It can be seen from equations (7.7) and (7.8) that the flux linkages are rotor position dependent. By moving from the stationary reference frame to a rotating reference frame the flux linkages are no longer dependant on the rotor position. A Park transformation is used to transform the static reference frame to a dynamic reference frame. It is given as follows (Krishnan, 2010):

$$\begin{bmatrix} V_{sd} \\ V_{sq} \end{bmatrix} = \frac{2}{3} \begin{bmatrix} \cos\theta_e & \sin\theta_e \\ -\sin\theta_e & \cos\theta_e \end{bmatrix} \begin{bmatrix} V_\alpha \\ V_\beta \end{bmatrix} \tag{7.9}$$

It can be seen from (7.9) that V_{sd} and V_{sq} are now dependent on the voltage vector (V_α, V_β) components and on the rotor flux (Ψ_{pm}) position (θ_e). Therefore, if the rotor flux position is known then, by this projection, the dq component becomes a constant.

Applying the transformation of (7.9) to equations (7.5)-(7.8) the machine model is as follows:

$$V_{sd} = i_{sd}R_S + \frac{di_{sd}}{dt}L_d - \Omega_e L_q i_{sq} \tag{7.10}$$

$$V_{sq} = i_{sq}R_S + \frac{di_{sq}}{dt}L_q + \Omega_e L_d i_{sd} + \Omega_e \Psi_{pm} \tag{7.11}$$

$$\Psi_{sq} = L_q i_{sq} \tag{7.12}$$

$$\Psi_{sd} = L_d i_{sd} + \Psi_{pm} \tag{7.13}$$

where R_S is the stator resistance, Ω_e is the electrical rotor speed, L_d and L_q are the equivalent self inductances of the stator and Ψ_{pm} is the flux produced by the permanent magnets.

The representation of the system in the rotating dq reference frame is given in Figure B.1.1

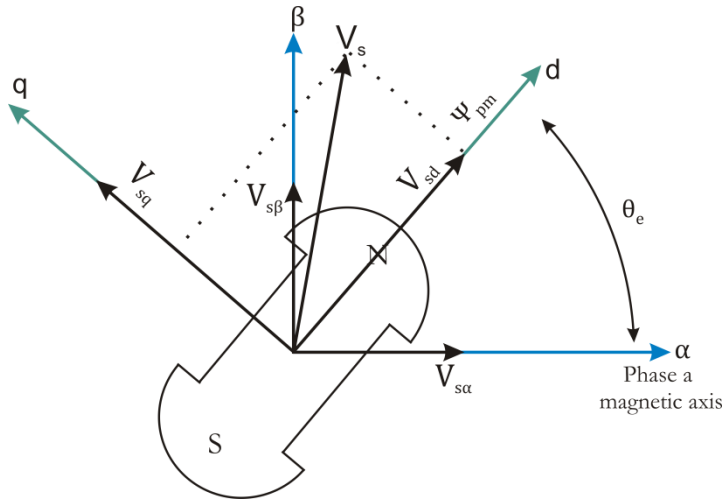

Figure B.1.1: Stator current space vector and its component in $(\alpha\beta)$ and in the (dq) rotating reference frame.

Appendix C Hardware in the Loop Test Rig

Appendix C 1 Power Component Parameters

Parameters of the permanently excited synchronous machines used on the test rig are as follows:

Parameter	Value
Rated Power	1.2 kW
Rated Voltage	400 V
Rated Torque	3.9 Nm
Rated Speed	1800 rpm
Stator Resistance (R_s)	6.8 Ω
Stator Inductance $(L_{sd} = L_{sq})$	24.3 mH
K_t [Nm/A]	1.6 Nm/A
K_e [V/krpm]	98 V/krpm
Encoder	Incremental with 4096 ppr

The VSC parameters are as follows:

Parameter	Value
Rated Power	10 kVA
Rated Voltage	400 V
DC Link Voltage (max)	800 V
AC Current (max)	15 A
Switching frequency	4 kHz
Modulation Index (M_a)	0.8
PWM sampling time (T_s)	250 µs
Capacitor bank	1020 µF

The grid connection parameters are as follows:

Parameter	Value
Grid coupling inductance (L_{grid})	3.5 mH
Grid coupling resistance (R_{grid})	16 mΩ

The auto-transformer parameters are as follows

Parameter	Value
Rated Power	5 kW
Rated Voltage Input	400 V
Output Voltage	0 – 400 V

Appendix D GH Tidal Bladed® Modelling

Appendix D 1 Parameters of Variable Speed Pitch and Stall Regulated TST Models.

All of the characteristics given in Table D.1.0 are common to both the Variable Speed Pitch and Variable Speed Stall Regulated TSTs.

Parameter	Turbine Parameters
Rated Power	1 MW
Rated Rotor Speed	13 rpm
Rated Hub Flow Speed (V_{flow})	2.4 m/s
TSR Below Rated	5.6
Rotor Diameter	23 m
Blade Length	10.6 m
Blade Mass	640 kg
Hub Mass	3500 kg
Rotor Mass	5420 kg
Rotor Blade Inertia, (J_{blade})	11986 kgm^2
Rotor Inertia, (J_r)	110 688 kgm^2
Transmission	Direct Drive Permanent Magnet
Number of Rotor Blades	3
Water Depth	50 m
Hub-Height above sea-bed	29 m
Rotor Position	Upstream

Table D.1.0: Parameters of Variable Speed Pitch and Variable Speed Stall Regulated Turbine Models implemented in GH Tidal Bladed®.

Appendix D 2 Blade Modes for Variable Speed Pitch and Stall Regulated Rotor Blades.

Within GH Tidal Bladed® the blades and the support structure are modelled as single linear flexible components using a modal approach. Each mode is defined in terms of the following parameters (Bossanyi, 2009):

- Modal frequency, ω_i
- Modal damping coefficient, ξ_i
- Mode shape represented as a vector of the displacement at each blade section.

For full details on how the modal frequencies and mode shapes are calculated the reader is referred to the GH Tidal Bladed® theory manual (Bossanyi, 2009). Details of the modal frequencies and modal damping coefficients for the rotor blades of the variable speed pitch and variable speed stall regulated TSTs introduced in this thesis are provided in the Tables below.

Modal Frequency (Hz)	Damping Ratio	Mode Type
6841	0.05	Rotor Blade: Flapwise
9415	0.05	Rotor Blade: Edgewise
22219	0.05	Rotor Blade: Flapwise
44892	0.05	Rotor Blade: Edgewise

Table D.2.0:Modal Frequencies and modal damping coefficients for variable speed pitch regulated rotor blades.

Modal Frequency (Hz)	Damping Ratio	Mode Type
7281	0.05	Rotor Blade: Flapwise
12393	0.05	Rotor Blade: Edgewise
17777	0.05	Rotor Blade: Flapwise
33392	0.05	Rotor Blade: Edgewise

Table D.2.1: Modal Frequencies and modal damping coefficients for variable speed stall regulated rotor blades.

Appendix D 3 Variation of Structural Properties along the Blade Length for Pitch Regulated Rotor Blades.

The stiffness distribution is defined in both the edgewise (X_{Edge}) and flapwise directions(X_{Flap}). For more information on how the blade parameters are defined the reader is referred to the GH Tidal Bladed® user manual (Garrad Hassan & Partners Ltd, 2009).

Fraction of Rotor Radius(r/R)	Chord	Twist Angle	Mass/Unit Length	Bending Stiffness (X_{Flap})	Bending Stiffness (X_{Edge})
[m]	[m]	[deg]	kg/m	Nm²	Nm²
0	1	21.30	204.67	2.5E+14	2.52E+14
0.375	1	21.30	225.16	2.5E+14	3.59E+14
0.75	1.49	21.30	132.24	1.12E+14	1.07E+14
1.125	1.67	21.30	103.84	5.62E+13	1.01E+14
1.5	1.67	21.30	108.87	4.3E+13	1.16E+14
1.875	1.59	19.70	108.63	3.57E+13	1.11E+14
2.25	1.48	18.41	103.75	2.91E+13	9.84E+13
2.4	1.44	17.22	102.80	2.72E+13	9.54E+13
3.15	1.23	12.54	86.87	2E+13	6.87E+13
3.9	1.06	9.29	74.56	1.43E+13	5.09E+13
4.65	0.92	6.93	59.92	9.42E+12	3.33E+13
5.4	0.81	5.16	44.95	5.51E+12	1.97E+13
6.15	0.72	3.79	34.20	3.11E+12	1.21E+13
6.9	0.65	2.69	23.68	1.37E+12	6.45E+12
7.65	0.59	1.8	16.00	4.76E+11	3.11E+12
8.4	0.54	1.06	11.33	1.59E+11	1.49E+12
9.15	0.5	0.43	10.57	1.56E+11	1.19E+12
9.75	0.47	0	10.57	1.56E+11	1.19E+12

Table D.3.0: Structural properties of pitch regulated rotor blade.

Appendix D 4 Variation of Structural Properties along the Blade Length for Stall Regulated Rotor Blades.

The stiffness distribution is defined in both the edgewise (X_{Edge}) and flapwise directions(X_{Flap}). For more information on how the blade parameters are defined the reader is referred to the GH Tidal Bladed® user manual (Garrad Hassan & Partners Ltd, 2009).

Fraction of Rotor Radius(r/R)	Chord	Twist Angle	Mass/Unit Length	Bending Stiffness (X_{Flap})	Bending Stiffness (X_{Edge})
[m]	[m]	[deg]	kg/m	Nm²	Nm²
0	1	14.75	204.67	2.43E+14	2.52E+14
0.375	1	14.75	225.16	2.5E+14	3.59E+14
0.75	1.49	14.75	132.24	2.49E+14	4.03E+14
1.125	1.67	14.75	103.84	1.7E+14	1.12E+14
1.5	1.67	14.75	108.87	1.3E+14	1.1E+14
1.875	1.59	13.16	108.63	8.82E+13	9.56E+13
2.25	1.48	11.86	103.75	6.45E+13	9.15E+13
2.4	1.44	10.68	102.80	4.94E+13	1.08E+14
3.15	1.23	6	86.87	4.09E+13	1.13E+14
3.9	1.06	2.75	74.56	3.57E+13	1.11E+14
4.65	0.92	0.39	59.92	3.11E+13	1.03E+14
5.4	0.81	-1.38	44.95	2.72E+13	9.54E+13
6.15	0.72	-2.75	34.20	2E+13	6.87E+13
6.9	0.65	-3.85	23.68	1.43E+07	5.09E+13
7.65	0.59	-4.74	16.00	9.42E+12	3.33E+13
8.4	0.54	-5.48	11.33	5.51E+12	1.97E+13
9.15	0.5	-6.11	10.57	3.11E+12	1.21E+13
9.75	0.47	-6.54	10.57	1.37E+12	6.45E+12

Table D.4.0: Structural properties of pitch regulated rotor blade.

Appendix D 5 Turbine States Included in the Linearised Models of the Variable Speed Pitch and Variable Speed Stall Regulated Turbine Models.

State	Description
Gearbox LSS angular displacement	$\Delta x1$
Gearbox LSS angular velocity	$\Delta x2$
Blade 1 mode 1 displacement	$\Delta x3$
Blade 1 mode 1 velocity	$\Delta x4$
Blade 1 mode 2 displacement	$\Delta x5$
Blade 1 mode 2 velocity	$\Delta x6$
Blade 1 mode 3 displacement	$\Delta x7$
Blade 1 mode 3 velocity	$\Delta x8$
Blade 1 mode 4 displacement	$\Delta x9$
Blade 1 mode 4 velocity	$\Delta x10$
Blade 2 mode 1 displacement	$\Delta x11$
Blade 2 mode 1 velocity	$\Delta x12$
Blade 2 mode 2 displacement	$\Delta x13$
Blade 2 mode 2 velocity	$\Delta x14$
Blade 2 mode 3 displacement	$\Delta x15$
Blade 2 mode 3 velocity	$\Delta x16$
Blade 2 mode 4 displacement	$\Delta x17$
Blade 2 mode 4 velocity	$\Delta x18$
Blade 3 mode 1 displacement	$\Delta x19$
Blade 3 mode 1 velocity	$\Delta x20$
Blade 3 mode 2 displacement	$\Delta x21$
Blade 3 mode 2 velocity	$\Delta x22$
Blade 3 mode 3 displacement	$\Delta x23$
Blade 3 mode 3 velocity	$\Delta x24$

Blade 3 mode 4 displacement	$\Delta x25$
Blade 3 mode 4 velocity	$\Delta x26$
Blade 1 actuator position state 1	$\Delta x27$
Blade 2 actuator position state 1	$\Delta x28$
Blade 3 actuator position state 1	$\Delta x29$
Generator electrical torque	$\Delta x30$

Table D.5.0: Turbine States.

Appendix D 6 Pitch System Parameters

Actuator Time Constant (T_{act}) = 0.2 s

Angle Limits: Min = 0°, Max = 90°

Pitch rate limit = ±8°

Appendix D 7 Pitch and stall controller gains above rated flow speed

Flow speeds from 2.5–5 m/s. Gains (k_{gs}) given for steps of 0.1m/s for pitch and stall controllers.

Pitch: $=K_{\mathrm{c\_pi}}(s)$ = [65, 54, 50, 46, 43, 43, 43, 42, 41, 40, 39, 38, 37, 36, 35, 34, 33, 32, 31, 30, 29, 28, 27, 26, 25, 24].

Pitch: $K_{\mathrm{c\_pi\_lead}}(s)$ = [162.5, 135, 125, 115, 107.5, 107.5, 107.5, 105, 102.5, 100, 97.5, 95, 92.5, 90, 87.5, 85, 82.5, 80, 77.5, 75, 72.5, 70, 67.5, 65, 62.5, 60].

Stall (from 2.5–3 m/s): k_{s1} = $10^{6}\cdot$ [26.68, 26.68, 29, 26.68, 34.8, 30.16].

Stall (from 3.1–5 m/s): k_{s2} = $10^{6}\cdot$ [139.2, 145, 174, 145, 156.6, 150.8, 168.2, 168.2, 165.88, 174, 162.4, 171.68, 162.4, 174, 179.8, 179.8, 179.8, 179.8, 179.8, 179.8].